Biofilm Growth Dynamics Characterized by Electrochemical Impedance Spectroscopy

Thesis

Presented in Partial Fulfillment of the Requirements for the Degree Master of Science in the Graduate School of The Ohio State University

By

Kaitlyn LeeAnn Kearns

Graduate Program in Mechanical Engineering

The Ohio State University

2022

Thesis Committee

Dr. Shaurya Prakash, Advisor

Dr. Paul Stoodley

Abstract

The treatment of biofilm-related infections and implant failure is an area of major concern that costs the healthcare industry billions of dollars each year. While a great deal of research has been conducted to eliminate biofilms after an infection has set in, less is known about the underlying causes behind these infections and the way biofilms form. Biofilm growth and communication are only a few of their many characteristics that exhibit electrochemical properties. These characteristics can be measured through electrochemical impedance spectroscopy (EIS).

In this thesis, we design and iterate on the fabrication procedure for two versions of an EIS system with flat-patterned silver electrodes capable of collecting electrochemical data from *Staphylococcus epidermidis* biofilms directly above the electrodes. We verify the functionality of the device by using both a two-electrode system and a four-electrode system to measure the impedance of tryptic soy agar (TSA). The behavior of TSA measured by the two-electrode system included a region with a constant phase angle of -42.0 ± 4.6˚, and a region with a phase of 0˚. The 42.0˚ region corresponds to a constant phase element (CPE), or equivalent circuit component where the ratio of real to imaginary impedance stays constant such that the phase is not purely 0˚ or -90˚. The 0˚ region corresponds to a purely resistive circuit component. The CPE is also similar to a Warburg element, which specifically has a constant phase of exactly 45˚. The response of the TSA

measured by the four-electrode device was almost purely resistive with an average phase of -0.7 ± 1.7˚.

After verifying that the device could produce repeatable data, the two-electrode system was selected to measure the electrochemical response of *S. epidermidis* grown on a thin layer of TSA for 0 hours, 8 hours, 16 hours, and 24 hours. All four growth durations showed an increase in the absolute value of the phase angle and the impedance of the system as opposed to TSA-only data. The 0-hour measurements were closest to the TSA-only measurements in phase angle and impedance. The 8-hour measurements had the greatest increase in absolute value of phase angle and impedance, both of which decreased with 16-hour and 24-hour measurements. The results from the biofilm studies were also found to be repeatable.

Acknowledgments

I would like to thank my advisor, Dr. Shaurya Prakash, for his guidance, expertise, and patience at each stage of this project. I would also like to thank Dr. Paul Stoodley for serving on my master's committee, permitting me to use his lab space, his contributions to this project, and his guidance for any microbiology-related questions. I thank Keith Ramsey and Paul Steffen at Nanotech West for their help in training me and developing my photolithography processes. Additionally, I thank my peers in the Microsystems and Nanosystems Lab for their support and comradery during my time at the Ohio State University. I would like to thank my family and especially my fiancé, Luke, for providing their continued encouragement through the last two years. Finally, I thank the Ohio State University for funding my master's education through my University Fellowship and GTA position.

Vita

2016……	West Jessamine High School, Nicholasville, KY
2020……	Bachelor of Science, Mechanical Engineering
	Minors in Mathematics and Music Performance
	University of Kentucky, Lexington, KY
2020……	University Fellow
	The Ohio State University, Columbus, OH
2021 to present……..	Graduate Teaching Assistant, Department of Mechanical
	and Aerospace Engineering
	The Ohio State University, Columbus, OH

Publications

Kearns, K. L., Boyd, J. D., & Grady, M. E. (2020). Biofilm rupture by laser-induced stress waves increases with loading amplitude, independent of location. *ACS Applied Bio Materials*, *3*(3), 1426-1433.

Fields of Study

Major Field: Mechanical Engineering

Table of Contents

List of Tables

List of Figures

Chapter 1. Introduction

1.1 Motivation

Biofilm infections pervade several facets of the healthcare industry. Biofilms are found in over 75% of chronic wounds[1-4], the treatment of which costs billions of dollars each year[5, 6]. These infections also result in the failure of implantable medical devices such as dental implants[7-9] and prosthetic joints[10, 11] through associated infections. Our group has previously reported on a printed electroceutical dressing for eliminating bacterial infections from chronic wounds[12, 13], which is a valuable device for these severe situations. However, expanding the knowledge of biofilm growth and communication is of equal importance to designing remedies to their consequences.

Previous research has shown that as biofilm colonies grow, the bacteria communicate through multiple electrical and chemical signaling methods[14-17]. These communication methods change the electrical properties of the biofilm depending on what is occurring in the colony and can be measured through electrochemical techniques such as potentiometry, voltammetry, and electrochemical impedance spectroscopy[18]. Electrochemical impedance spectroscopy (EIS) is a technique that is already widely used on biofilms to study several subjects such as colony growth and surface adhesion[19-25]. This technique has been chosen by many researchers because it does not cause the biofilm to be damaged or killed during experiments[26].

Thus far, the area of biofilm communication measured *via* EIS has not been thoroughly researched. Due to its ability to measure electrochemical responses in real time without damaging the biofilm, this technique is excellent for monitoring biofilm communication because the biofilm must be alive to communicate. In the past, EIS has been used to study biofilm maturation and adhesion based on the change in impedance by comparing findings to other established methods of biofilm monitoring[19-21, 23-25]. Prior research also supports that certain methods of bacterial communication, such as quorum sensing[27] and ion-channel signaling[28], have an impact on the electrochemical activity within the biofilm. Using EIS, the changes in the electrochemical activity of a biofilm can be monitored and related to either growth dynamics or possible bacterial communication occurring within the colony. In this thesis, we design and test two variations of a device for measuring the impedance of a biofilm at multiple stages of growth using electrochemical impedance spectroscopy (EIS), with particular interest in how the electrochemical response changes as it transforms from a planktonic colony to a biofilm-lawn grown over 24-hour period. Previously, our group[12, 29, 30] has used lawn biofilms grown on TSA-agar as a model for soft tissue infection studies. These lawn biofilms have been used to evaluate a pioneering electroceutical technology from our team[13]. Therefore, the goal of this thesis is to electrochemically evaluate the formation of these 24-hour lawn biofilms.

1.2 Specific aims of this research

The specific aims of this Master's Thesis project are:

1. Designing and developing the fabrication procedure for single-use devices used for performing EIS on biofilms.

2. Verifying the functionality of the devices by performing EIS on tryptic soy agar alone and comparing results to previous work.
3. Establishing the properties of the device as compared to previous work by observing differences in electrochemical responses between stages of biofilm growth (0 hours, 8 hours, 16 hours, and 24 hours).

1.3 Biofilm characteristics

A biofilm is a colony of bacteria that is characterized by the addition of extracellular polymeric substance, or EPS[31, 32]. The EPS is a substance excreted from a bacterium that alters the mechanical and chemical properties of the bacteria colony[16, 33-36]. Initially, a biofilm begins as free-flowing individual cells (referred to as planktonic) suspended in a fluid such as growth media[37, 38] which come into contact with a surface. With the addition of EPS, the planktonic bacteria multiply and transform into a biofilm phenotype. This change results in an increased adhesion strength[39-42]. Due to this high adhesion strength, the fortified biofilm becomes much more difficult to remove by mechanical processes. Further, biofilms also distinguish themselves from ordinary planktonic bacteria by their increased antibacterial resistance, meaning that chemical treatments of biofilms are also often unsuccessful. Due to these qualities, biofilms can be found on almost any surface if nutrients and moisture are provided.

The growth of a biofilm from planktonic bacteria has been defined by most researchers as having four stages moving in a cyclical pattern[43, 44]. The first stage is reversible attachment, where individual bacteria attach themselves to a surface but have not yet begun producing EPS. The second stage is irreversible attachment, after the bacteria

have begun excreting EPS and forming bonds between one another. The third stage is called the maturation or growth stage, during which more EPS is produced, and more bacteria are added to the biofilm. The final stage is dispersion, where bacteria are released from the mature biofilm and attached somewhere else on the surface, thus repeating the process. An article by Kim et. al[19] used EIS methods to determine the beginning of the maturation stage. In Figure 1, an illustrated model of this growth cycle is provided, shown on the device designed for this thesis. Details on the fabrication of the device is detailed in sections 2.1 and 2.2.

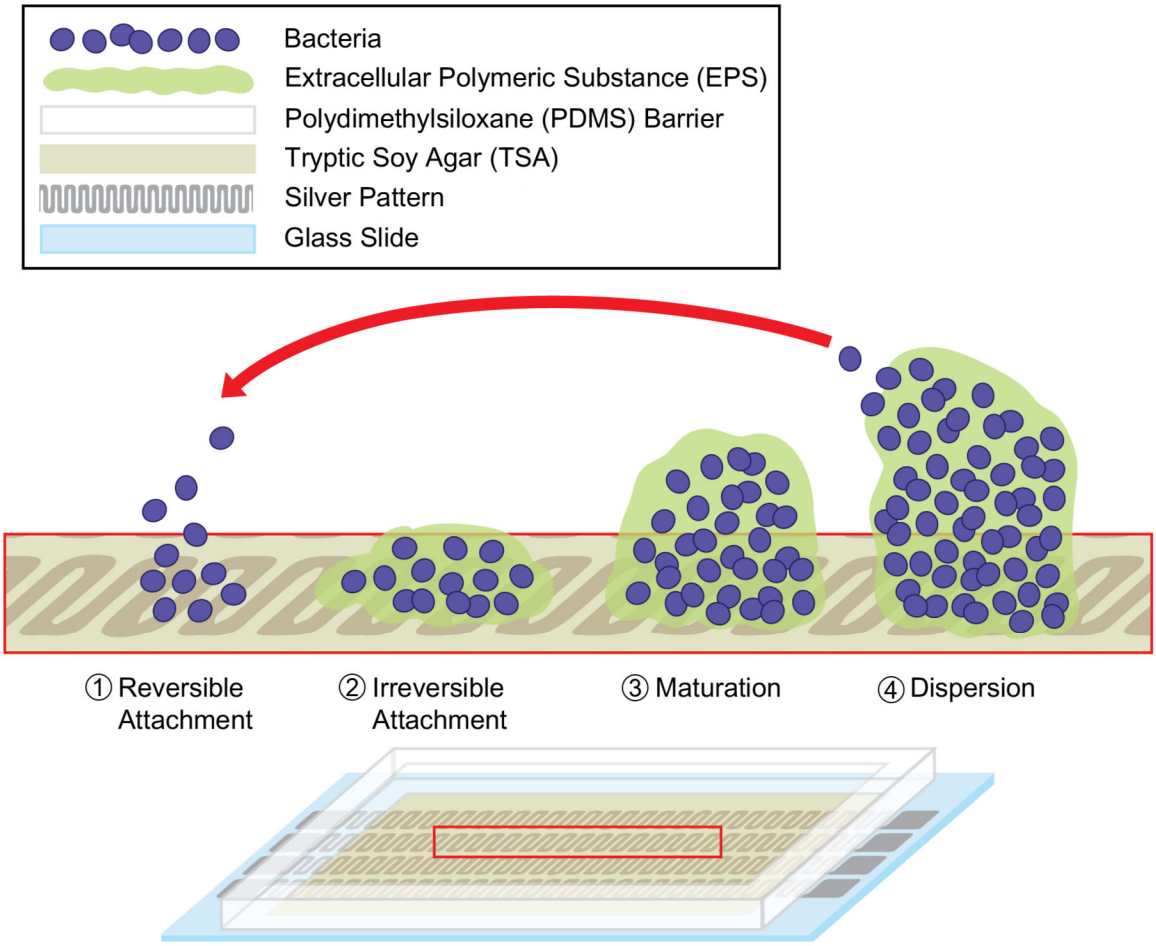

Figure 1. A visual model of the biofilm growth cycle

1.3.1 Industries impacted by biofilms

The resilience of biofilms makes them both a prevalent challenge and a source of innovation, depending on the industry and application. For example, biofilms such as growth-promoting rhizobacteria have been studied for agricultural applications such as increasing crop yields[45], improving sustainability[46], and treating wastewater[47]. Alternately, biofilms formed by harmful bacteria such as *Escherichia coli* and *Salmonella* cause challenges in the meat processing industry because their adhesion strength makes them

extremely difficult to irradicate and can result in mass spoilage of products if left unchecked[48, 49]. Biofilm adhesion strength also pervades the marine industry, and a considerable amount of research has been performed to design biofilm-resistant coatings for boats[50] or other methods to prevent biofouling[51, 52].

The impact of biofilms on the medical industry has been one of the most researched in this field. Virtually all medical devices can be affected detrimentally by biofilms. For example, biofilm impact on permanent implants such as dental implants[7-9], joint implants[10, 11], fluid shunts[53], and artificial pacemakers[54] have all been studied. In addition to permanent implants, other devices such as ventilators[55], catheters[56], surgical tools[57, 58], and contact lenses[59, 60] pose threats to those who need them if biofilm attachment occurs.

For each of these industries, the behavior of biofilms as opposed to the behavior of planktonic bacteria greatly affect the response required. For some, the adhesion strength of biofilms is desired, while others work to prevent adhesion. One of the biggest questions is at what stage and under which conditions this transition occurs. Therefore, understanding the methods of communication between individual bacterium as the colony transforms from a collection of planktonic bacteria to a biofilm is an essential next step in this area of research.

1.4 Bacterial communication

Bacteria, whether in a planktonic form or part of a biofilm, communicate through multiple electrochemical means including quorum sensing[27, 61], electron transfer[62], and ion-channel mediated signaling[28]. These communication methods provide gene regulation instructions and density-dependent information for other bacteria in the colony. Despite

technically being independent, single-celled organisms, bacteria can collaborate like a multicellular organism[14]. Each bacteria species has unique forms of communication[63]. The following sections explore some previous findings in specific forms of bacterial communication.

1.4.1 Quorum sensing

Prior research has defined quorum sensing (QS) as a common mode of communication utilized by bacterial colonies[27, 61]. Through QS, bacteria produce chemical signaling molecules called autoinducers that are sent out to the rest of the colony[64-67]. There are multiple ways in which bacteria can perform QS, and the precise reason these distinctions exist is still being explored. One primary distinction is the between Gram-positive and Gram-negative QS[63].

In Gram-positive QS, bacteria such as *Staphylococci* use peptides as autoinducers[68, 69]. Peptides are short chains of amino acids which are produced by bacterial ribosomes then secreted from a bacterium to bind with receptors on the membranes of other bacteria[70]. These receptors activate response regulators within the bacteria which induce target gene expression.

Gram-negative QS, such as that of *Pseudomonas* bacteria, uses acylhomoserine lactone (AHL) as an autoinducer. AHL is a signaling molecules produced by a gene called *lasI*. When AHL is released from one bacterium and enters another, it activates a protein called *lasR*. Once activated, *lasR* can bind to the DNA molecule and express the target gene[71, 72]. In Figure 2, the basics of QS for both Gram-positive and Gram-negative bacteria are illustrated.

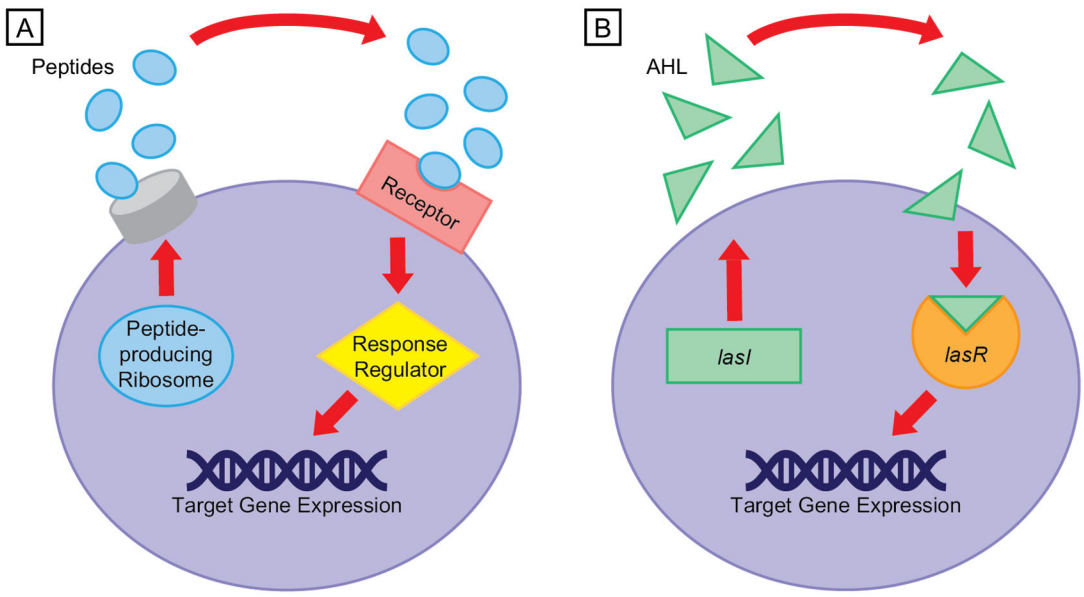

Figure 2. Quorum sensing as performed by (A) Gram-positive bacteria and (B) Gram-negative bacteria

1.4.2 Bacterial communication through electrochemical methods

In recent years, researchers have discovered multiple short-range and long-range electrochemical methods that bacteria use to communicate[14]. Most bacteria cell walls have a net negative charge due to the presence of carboxyl groups and ionized phosphoryl, thus attracting positive ions through membrane potential[15]. Major electrical signaling is performed through ion channels and is analogous to neurons in multicellular organisms.

During biofilm formation, depletion of nutrients causes stress on the bacteria within the biofilm[34]. In a study performed on the bacteria *Bacillus subtilis*, the growth rate of the biofilm was found to increase and decrease depending on the amount of nutrients available in the environment[73]. Glutamine, which is synthesized from glutamate and ammonium, is essential for the biofilm to grow. Since glutamate was available in the growth media, external cells were able to obtain the nutrients more easily than internal cells. Cells were

also able to produce ammonium from glutamate, but the group found that the ammonium concentration in the external cells diminished periodically even though the external cells were the most capable of receiving glutamate. The group proposed that some mechanism was allowing the interior and exterior cells to absorb glutamate in an alternating pattern, resulting in the variation in growth rate. Overall, the intended goal of this communication seemed to be protecting the interior bacteria by managing their resources, but the specific pathway that communicates this information is still being explored.

Ion channels are proteins situated in bacteria membranes that allow ions to travel through the membrane in a way that is analogous to action potential in neurons[17]. Multiple channel types have been documented including potassium (K+) channels[74, 75], sodium (Na+) channels[76], and chloride (Cl-) channels[77]. The full extent of the tasks carried out through ion channel communication are still being explored, but some of its purposes have been observed. Prindle et. al further studied the communication of *B. subtilis* through ion channels[28]. They found that the bacteria were able to relay their metabolic state to the rest of the colony using K+ ion channels. Metabolic oscillations occurred as the metabolic stress level passed from the interior bacteria to the exterior bacteria. At the same time, the movement of positively charged ions to the exterior bacteria would prevent them from taking up ammonium, a positively charged nutrient. Conversely, the concentration of K+ ions in the exterior bacteria allowed them to take up glutamate more easily, which is negatively charged.

From these studies, the electrochemical properties of biofilms, including membrane potential and ion-channel-mediated signals, change as their environment changes, even

within the same colony[14, 17, 28, 73, 75]. By linking the electrochemical responses of a biofilm to the stages of biofilm growth, a new quantitative approach to preventing biofilm infection could be formed. In the following section, we describe a method for monitoring the electrochemical properties of a biofilm.

1.5 Electrochemical impedance spectroscopy

Electrochemical impedance spectroscopy, or EIS, is a process that obtains the impedance spectrogram of complex electrochemical materials. This process has been used to characterize electrochemical devices such as batteries[78-80], capacitors[81-83], and fuel cells[84-86]. As research in this area has developed, other materials have been studied, including biological materials[23, 25, 87-89].

To perform an EIS measurement, an instrument called a potentiostat applies either sinusoidal voltage or current signal to an electrochemical material. In return, the electrochemical material responds with a corresponding alternate signal. If a voltage is applied and a current is measured, the EIS method is called potentiostatic EIS. If a current is applied and a voltage is measured, the EIS method is called galvanostatic EIS. Modifying the frequency and amplitude of these inputs will create different responses in the measured material. The output signal has an equal frequency to the input signal but has a different amplitude and may have a phase offset as well. The ratio of the voltage, $\hat{E}$ to the current, $\hat{I}$, gives us the impedance, $\hat{Z}$, as shown in equation 1.

$$\frac{\hat{E}}{\hat{I}} = \hat{Z} \qquad [1]$$

This equation is another form of Ohm's law, shown in equation 2, where V is voltage and R is resistance[90].

$$\frac{V}{I} = R \quad [2]$$

Like resistance, impedance is the opposition to current flow, specifically in an alternating current system.

1.5.1 Setup of electrodes for EIS experiments

The specific device used to perform EIS in this thesis is a Gamry Interface 1000 Potentiostat. The four leads of this device are defined in Table 1.

Table 1. Leads of a Gamry potentiostat

Lead Name	**Description**
Working	Carries voltage
Working Sense	Measures current
Reference	Measures current
Counter	Carries voltage

Deciding how to connect these leads to the electrochemical medium being studied depends on factors such as the desired complexity of the experiment setup, the desired complexity of analysis, the type of information that is needed, and the previous research performed on similar media[91]. These leads can be connected to the electrochemical medium in two-electrode, three-electrode, or four-electrode methods.

Experiments which use two electrodes are the simplest to set up but obtain the most difficult data to analyze, because it obtains information about the entire system rather than measured media. For these experiments, the working and working sense leads are connected to one electrode, and the reference and counter leads are connected to the second electrode. Since the two electrodes that carry the voltage are the same that measure the current, this method measures the impedance of the entire system.

The three-electrode experiments pair the working and working sense leads again but separate the reference and counter leads. This method only measures the side of the cell that has the working and working sense electrode and will provide a higher degree of accuracy to the measurements at a specific region of interest.

For four-electrode experiments, each lead is connected to an electrode. This method yields data that is easier to analyze. Only the impedance of the solution itself, independent of the current-carrying electrodes, is measured because the electrodes carrying the voltage are distinct from those measuring the current.

Two-electrode and three-electrode measurements are most commonly used for biofilm research. These types of measurements find information related to the entire system and the interactions that occur across barriers in the system. A four-electrode device would only be able to provide the total impedance of the growth media and biofilm. Both two-electrode and three-electrode devices can be used to uncover the interactions between a surface and a biofilm, such as how biofilm adhesion strength changes over time.

1.5.2 Presenting EIS data

Two of the methods to visualize EIS data are Bode plots and Nyquist plots. A Bode plot is comprised of two components. The first is created by plotting the magnitude of impedance in Ohms against the frequency in Hertz, both plotted on a logarithmic scale. The second is created by plotting the phase of the impedance in degrees against the frequency in Hertz, where only the frequency is still plotted on a logarithmic scale. Another version of a Bode plot uses a polar coordinate system to plot the magnitude of impedance at its respective phase angle.

A Nyquist plot is produced by transforming the polar coordinate system to a cartesian coordinate system, so the two other sides formed by this triangle can be measured. Along the x-axis, the real, or resistive, component of the impedance is given. Along the y-axis, the imaginary, or reactive, component of the impedance is given.

As one might expect, an electrochemical system that is fully resistive is simply a resistor. As more elements are added to a circuit, the Bode and Nyquist plots change. All systems measured through EIS can be modeled by an equivalent circuit. In Figure 3, the Bode and Nyquist plots are depicted for a combination of two circuit elements, a resistor and capacitor, in series and in parallel. In Figure 4, an inductor is added to the series and parallel circuits. Realistic resistance, capacitance, and inductance values were used to help portray the changes that occur when these circuit elements are included. In these figures, resistance is R = 10 Ω, capacitance is C = 1 nF, and inductance is L = 100 pH. The MATLAB code used to calculate and plot the figures is provided in Appendix B.1.

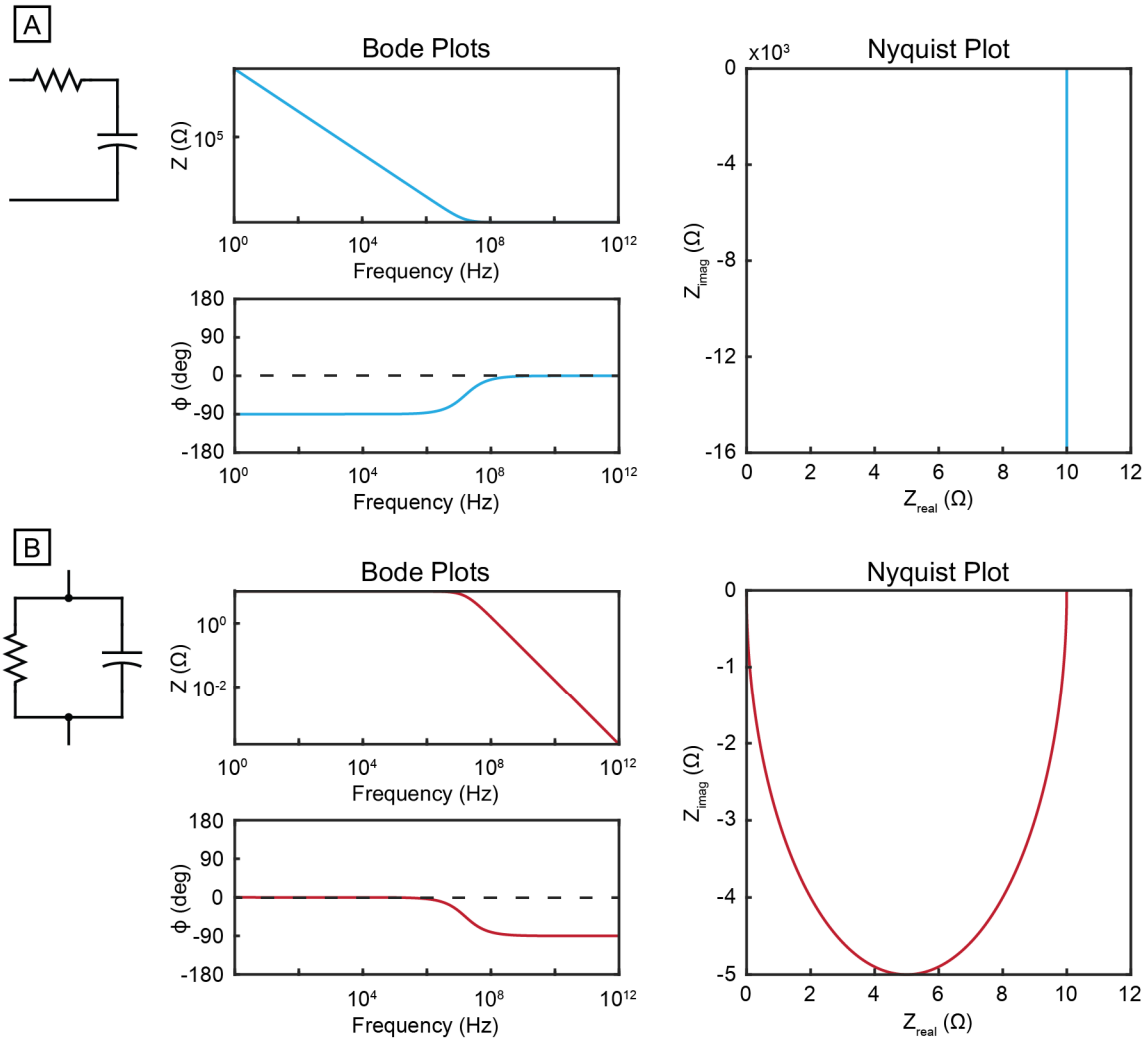

Figure 3. The Bode and Nyquist plots for a resistor (R = 10 Ω) and capacitor (C = 1 nF) (A) in series and (B) in parallel

Some interesting details about the impacts of each circuit element can be found by studying the plots in Figure 3. In the magnitude Bode plot of Figure 3A, the magnitude of the impedance starts at a high value because the capacitor has a very high imaginary impedance at low frequencies. However, the initial magnitude of the impedance in Figure 3B is only 10 Ω. This occurs because in a series circuit, the signal must pass through both the capacitor and the resistor, and the capacitor dominates the impedance value. In a

parallel circuit, the signal will take the path of least resistance, which is the side with the 10 Ω resistor. The frequency at which the dominating circuit element changes, such as changing from the capacitor to the resistor in the series circuit, is called the corner frequency.

The Nyquist plot of Figure 3A shows that for all frequency values, the resistor contributes to the real value of the impedance while the imaginary component only comes from the capacitor. When the signal can go through either the resistor or capacitor, such as in Figure 3B, the resistor is the pathway used at lower frequencies while the capacitor is used at higher frequencies.

The phase Bode plots indicate which circuit element dominates the phase. When the capacitor is dominating the phase, the phase angle is -90˚, and when the resistor is dominating the phase, the phase angle is 0˚. In Figure 3A, the capacitor is dominating at low frequencies because it has the higher impedance, but the resistor dominates the phase later as the imaginary impedance decreases. The opposite is shown in Figure 3B, where the resistor dominates the phase at lower frequencies because it offers the least resistance initially, but the capacitor dominates at higher frequencies as the imaginary impedance continues to decrease.

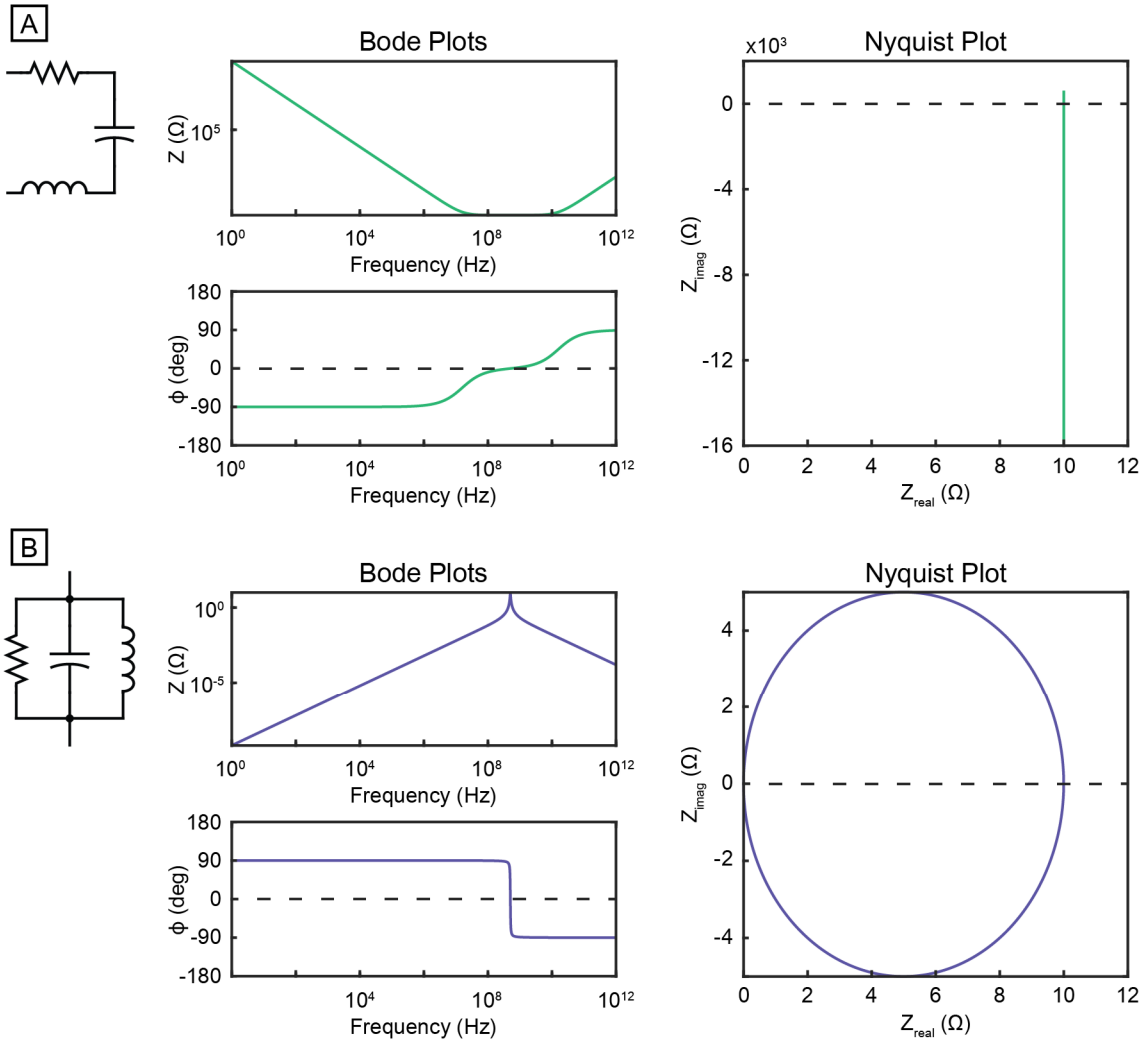

Figure 4. The Bode and Nyquist plots for a resistor (R = 10 Ω), capacitor (C = 1 nF), and inductor (L = 100 pH) (A) in series and (B) in parallel

Once an inductor is added to the circuit, the plots become more complex. While a capacitor has a very high negative imaginary impedance at low frequencies, an inductor has very small positive imaginary impedance at low frequencies. For the magnitude Bode plot in Figure 4A, the positive slope at the higher frequencies is due to the inductor, which

has the highest impedance out of the three circuit elements when at higher frequencies. The inductor also dominates the phase at higher frequencies with a phase of 90˚.

The peak that occurs on the magnitude Bode plot of Figure 4B is a result of the positive and negative imaginary impedance values of the inductor and capacitor cancelling each other out. This point is called the resonant frequency. On the phase Bode plot, the inductor dominates at lower frequencies and the capacitor dominates at higher frequencies.

The positive impedance of the inductor also contributes to the Nyquist plots. In Figure 3A, the Nyquist plot stopped at 0 because the capacitor only has negative imaginary impedance values, but in Figure 4A there are positive imaginary impedance values. The Nyquist plot in Figure 4B is the same as that of Figure 3B, but with positive imaginary impedance values as well.

1.6 EIS on biofilms

EIS is a useful tool for studying biofilms because it provides a quantitative measurement of the electrochemical activity occurring in the colony[88]. A wide variety of experimental methods and bacteria species have been studied by researchers in the past few decades. One of the earliest uses of this technique was by Franklin et. al in 1991 to study microbiologically influenced corrosion (MIC). The technique was found to be a viable method for studying biofilms without disturbing the growth of the colony[26, 92] and continues to be a widely utilized experimental method in MIC research[62, 87, 89, 93-97]. EIS is also commonly used to help determine properties of biofilms as components in microbial fuel cells (MFCs)[98-104]. Due to its harmless effect on the biofilm, EIS has been used to study biofilm growth and adhesion while the colony is active. A selection of seven publications

which use EIS to study biofilm activity and the experimental conditions of those studies are summarized in Table 2 and each reference is thoroughly explored in the following section.

In 2011, Kim et. al[19] utilized EIS to identify the beginning of the maturation stage of *Pseudomonas aeruginosa* biofilm. The group's EIS experiment used a 3-electrode technique. Bacteria was grown for 0, 6, 24, 48, and 72 hours on a platinum disk working electrode, then submerged in an electrochemical cell along with a platinum wire counter electrode, and an Ag/AgCl reference electrode. After analyzing the resultant data, the group was able to produce an equivalent circuit for the system, consisting of a solution resistance in series, then a double-layer capacitance and charge transfer resistance in parallel. The double-layer capacitance, or capacitance between the electrodes and the electrolytic solution, was identified as a constant phase element (CPE) that allowed them to identify the initiation point of biofilm maturation. A CPE is a circuit element commonly used in electrochemistry research that represents a double-layer interaction, or imperfect capacitance, between a solution and substrate[105]. The constant phase refers to the constant ratio of real to imaginary impedance that results in a phase that is neither 0˚, which would make the element a resistor, nor -90˚, which would make the element a capacitor. According to the Bode plots provided, the group did not find much variation in their data across the 72 hours of measurements. However, they did not report the individual Nyquist plots for each time point and only provided an average Nyquist plot for all time points. The equivalent circuit, shown in Figure 5A for this study, is one potential model that can be

used for this thesis, where the double-layer capacitance at the interface between the electrodes and growth media was represented as a CPE.

Also in 2011, Ben-Yoav et. al[20] studied the adhesion of *Escherichia coli* by flowing a suspension of the bacteria in growth media through their system and monitoring bacterial deposition through image analysis. Simultaneously, EIS measurements were collected at 30, 60, 90, and 120 minutes at 50 mV excitation. Their EIS system consisted of two indium-tin-oxide working and counter electrodes, which were positioned at the bottom and top of the flow chamber, respectively, and an Ag/AgCl reference electrode positioned at the inlet. Following the initial flow and attachment of bacteria, the bacterial suspension was replaced with sterile growth media to represent the growth of the attached cells in nature. An additional grid of EIS measurements was obtained at 12, 22, 35, 48, 67, and 91 hours of growth using three different DC excitations: 600 mV, 50 mV, and -500 mV. Data from these measurements indicated an anomalous diffusion where diffusion was not perfectly linear due to diffusion slowing over time. This anomalous diffusion, specifically sub-diffusion, occurred when some particles in an electrolytic solution adhere to the surroundings rather than moving with the solution. The Nyquist plot for the 600-mV excitation showed an increase in the impedance of the biofilm as compared to the 50-mV excitation, which Ben-Yoav et. al described as biofilm expansion. The -500-mV excitation showed a slight decrease of the biofilm impedance with respect to the 50-mV excitation, which they called biofilm contraction. The equivalent circuit they designed for their model was more complex than Kim et. al. and is provided in Figure 5B.

Fraiwan et. al[21] published on their device for performing EIS on biofilms in 2015. This device was unique because it was designed to be transparent and allow microscope imaging to occur concurrently with electrochemical experiments. Fraiwan et. al used a three-electrode setup including a gold working/working sense electrode which was transparent enough to image through it. They also used an Ag/AgCl reference electrode and a carbon counter electrode, both of which were screen-printed. Due to the nature of their device, the three-electrode measurement was selected to ensure the response of the biofilm was measured correctly. The biofilm was grown between the reference electrode and the working/working sense electrode, meaning that the measurements were restricted to a smaller region. A syringe pump was used to supply a flow of bacteria to the system and EIS measurements were taken before and after biofilm formation had occurred, similarly to Ben-Yoav et. al. The group primarily reported cyclic voltammetry data but did include Nyquist plots for both biofilms that were studied. Both plots indicated that the imaginary, or reactive, component of impedance decreased after the biofilm was formed. The group did not report an equivalent circuit to model their plots.

Out of all publications described in this section, Ward et. al[25] reported on a device and experiments that most closely aligned with the goals of this thesis. The goal of the paper was to establish an EIS method capable of determining unique electrochemical responses across different bacteria species, with the outlook of using the technique in rapid diagnostic methods. Their device consisted of a two-electrode system composed of two screen-printed carbon electrodes. Similar to the experiments in this thesis, Ward et. al also use a flat-pattern two-electrode device. In addition to the device itself, Ward et. al used

Staphylococcus aureus as their measured biofilm, which is of the same bacterial family as *S. epidermidis*, studied in this thesis. The Bode plots reported in this study indicated that the phase was most impacted at 1 kHz measurements and the magnitude of impedance was most affected at lower frequencies. For both cases, this impact was greatest after 2 hours of growth and had decreased by the time 24-hour measurements were collected. The group reported a similar equivalent circuit to what was previously reported by Kim et. al, but did not represent their double-layer capacitance as a CPE. The equivalent circuit is replicated in Figure 5C.

Huiszoon et. al[106] published on a flexible EIS system for measuring impedance of biofilms on three-dimensional surfaces such as medical devices. They chose *E. coli* as their bacteria species and recorded measurements at 0, 6, 12, and 24 hours of growth. Their system was a two-electrode system consisting of two gold interdigitated electrodes, similar to our two-electrode design. While they did not report an equivalent circuit, their magnitude Bode plots matched the patterns found when performing EIS on a resistor and capacitor in series. There was minimal difference in impedance across all four time points.

In a 2019 article by Bharatula et. al[23], the need for a mechanism to rapidly study biofilm adherence and electrochemical activity on larger areas than can be observed through traditional microscopy methods was explored. The group selected *P. aeruginosa* for their measurements and used a three-electrode system for EIS which consisted of an indium-tin-oxide working electrode, a titanium counter electrode, and an Ag/AgCl reference electrode. They reported both Bode and Nyquist plots for measurements recorded across several time points from 0-96 hours of growth. The Nyquist plots indicated a

consistent decrease in imaginary impedance as the age of the biofilm increased. At low frequencies, the Bode plot indicated that the phase increased as growth duration increased. The phase was consistent across all time points at medium and high frequencies. The equivalent circuit reported by this group is similar to Kim et. al and Ward et. al, and consists of two sets of resistors and CPEs in parallel as well as a solution resistance. Each set of resistor and CPE corresponds to a biofilm-electrode interfacial element and a charge accumulation element. This equivalent circuit is replicated in Figure 5D.

In 2020, Romero et. al published their study of biofilm attachment using EIS methods. The measurement system consisted of two graphite working and counter electrodes and an Ag/AgCl reference electrode. Since their specific bacterium, and therefore whether it was Gram-positive or Gram-negative, was not reported, we cannot fully determine how the results from this study align with previous publications. However, the Nyquist plots indicated that the imaginary component of impedance of the biofilm decreased as growth duration increased, corresponding to the results found by Fraiwan et. al and Bharatula et. al. Romero et. al reported an equivalent circuit that includes solution resistance and biofilm capacitance and resistance in parallel. The equivalent circuit is provided in Figure 5E.

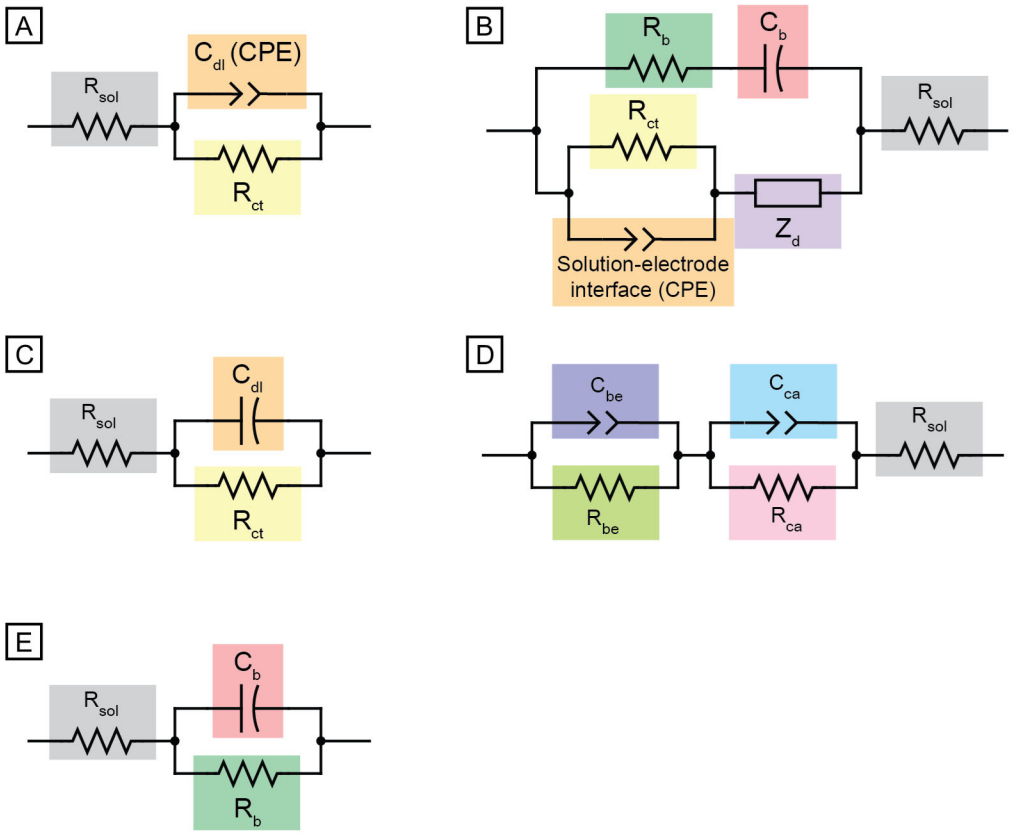

Figure 5. Equivalent circuits of EIS on biofilms reported in five publications. Corresponding circuit elements are highlighted in the same color to identify similarities between models. R_{sol} is solution resistance, C_{dl} is double-layer capacitance, R_{ct} is charge-transfer resistance, R_b is biofilm resistance, C_b is biofilm capacitance, Z_d is a diffusion impedance element, C_{be} is biofilm-electrode interface capacitance, R_{be} is biofilm-electrode interface resistance, C_{ca} is charge accumulation capacitance, and R_{ca} is charge accumulation resistance. Circuits are replicated from figures by (A) Kim et. al[19] (B) Ben-Yoav et. al[20] (C) Ward et. al[25] (D) Bharatula et. al[23] and (E) Romero et. al[24].

Table 2. Previous experimental conditions for EIS on biofilms

Authors	Year	Bacteria Species	Number and Material of Electrodes	Voltage	Current Range
Kim et. al[19]	2011	*P. aeruginosa*	2 platinum working and counter, 1 Ag/AgCl reference	10 mV AC	100kHz – 1 Hz
Ben-Yoav et. al[20]	2011	*E. coli*	2 indium-tin-oxide working and counter, 1 Ag/AgCl reference	600, 50, -500 mV DC	400 kHz – 100 mHz
Fraiwan et. al[21]	2015	*S. oneidensis* and *P. aeruginosa*	1 gold working/working sense, 1 carbon counter, 1 Ag/AgCl reference	10 mV AC	100 kHz – 100 mHz
Huiszoon et. al[106]	2018	*E. coli*	2 gold working/working sense and counter/reference	50 mV AC	100 kHz – 10 Hz
Ward et. al[25]	2018	*S. aureus*	2 Carbon ink working/working sense and counter/reference	200 mV AC	1 MHz – 1 Hz
Bharatula et. al[23]	2019	*P. aeruginosa*	1 indium-tin-oxide working, 1 titanium counter, 1 Ag/AgCl reference	10 mV AC	100 kHz – 30 mHz
Romero et. al[24]	2020	Combination of ureolytic bacteria	2 graphite working and counter, 1 Ag/AgCl reference	10 mV AC	10 kHz – 1 mHz

Chapter 2. Methods Section

2.1 Electrode patterning through photolithography

Our devices for this study consisted of a 38 mm x 76 mm x 1 mm glass slide, a 100 nm thick silver pattern, and a PDMS barrier. We used two different silver patterns: a two-electrode interdigitated pattern and a 4-electrode pattern.

Fabrication of the silver patterns on glass slides was performed via solvent lift-off in a cleanroom. Solvent lift-off is a common procedure used in photolithography, where the substrate is first coated in a negative photoresist (PR), exposed using a photomask, and developed to leave the bare substrate material in the regions where the final pattern will exist. Then, the substrate is coated with the desired material. Finally, a solvent is used to remove all remaining PR that had been developed before the coating process. The coated material that was adhered to the developed PR is lifted off (hence the process name) and the coated material that was adhered directly to the substrate is left behind.

Following a precleaning procedure, the glass slides were coated with a 1.8 μm coating of AZ nLOF 2020 negative PR using an Apogee Spin Coater. The PR was soft baked then exposed using a chrome photomask in hard contact for 7 seconds. A post-exposure bake smoothed the PR. The PR was developed in a dish of MF-CD-26 developer for 60 seconds, removing the unexposed regions of PR. Each slide was rinsed in deionized water, dried, and inspected under a microscope. A 100 nm coating of silver was evaporated

onto the same side as the PR coating using a CHA Solution System E-Gun Evaporator. To complete the process, the slides were submerged in 80˚C N-Methyl-2-pyrrolidone (NMP), which dissolved the developed PR and lifted off the excess silver coating in those regions. The slides were rinsed thoroughly with methanol and isopropyl alcohol and the features were inspected under a microscope before the slides were used in the next steps. A more detailed description of the silver patterning procedure is provided in Appendix A.1.

2.2 Fabrication of PDMS barriers

In order to grow biofilms directly above the silver patterns, wells were fabricated using a 2-part silicone mixture Polydimethylsiloxane (PDMS) to keep bacteria and growth media from flowing off the glass slides. A 10-part to 1-part mixture by mass was mixed thoroughly to ensure an even solution. To remove air bubbles from mixing, the PDMS was placed in a vacuum chamber for 1 hour to degas. After degassing, approximately 15.75 g of mixture was poured into an acrylic mold. The mold and PDMS were placed on a hot plate set to 70˚C and cured for 4 hours. The cured PDMS was carefully cut out of the acrylic mold and flash was trimmed using a pen knife. Using a Harrick Plasma cleaner, the PDMS was plasma bonded to the glass slides on the same side as the silver patterns. A more detailed description of this process is provided in Appendix A.2. The silver contact pads on the glass were left outside of the well and a two-part silver epoxy was used to attach wires to the contact pads. The final growth area within the well was 1290 mm^2. Figure 6 provides a visual representation of each key step in the fabrication process.

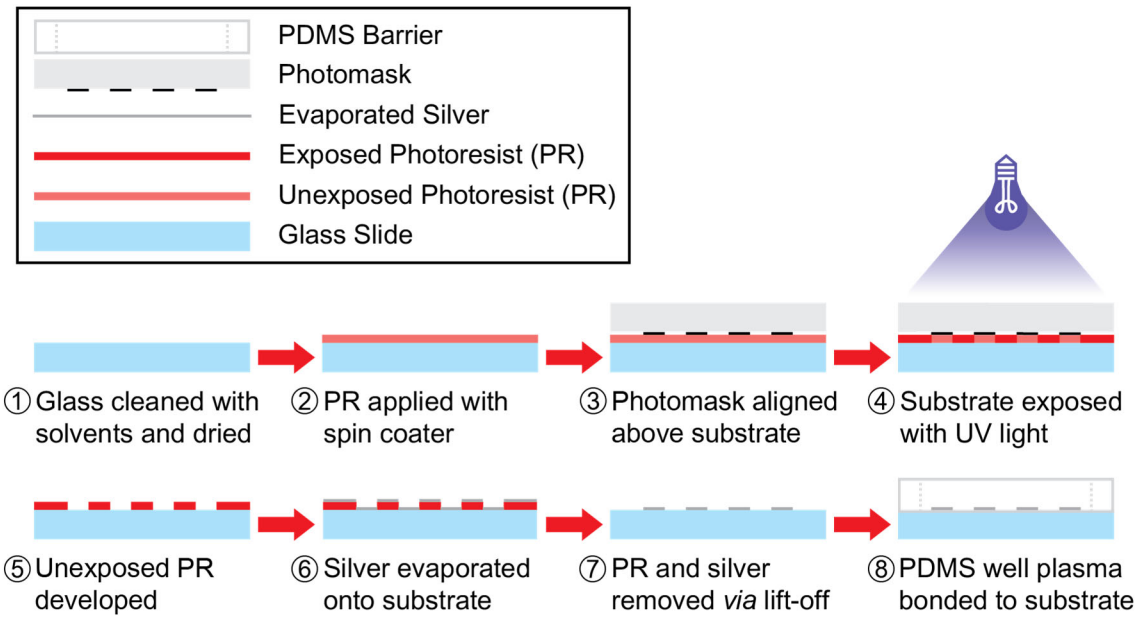

Figure 6. Pictorial representation of the device fabrication process

The final step of the fabrication process is to extend the contact pads by attaching lengths of wire to the contact pads with a 2-part silver epoxy. Figure 7 shows an illustration of the final device setup before media is added.

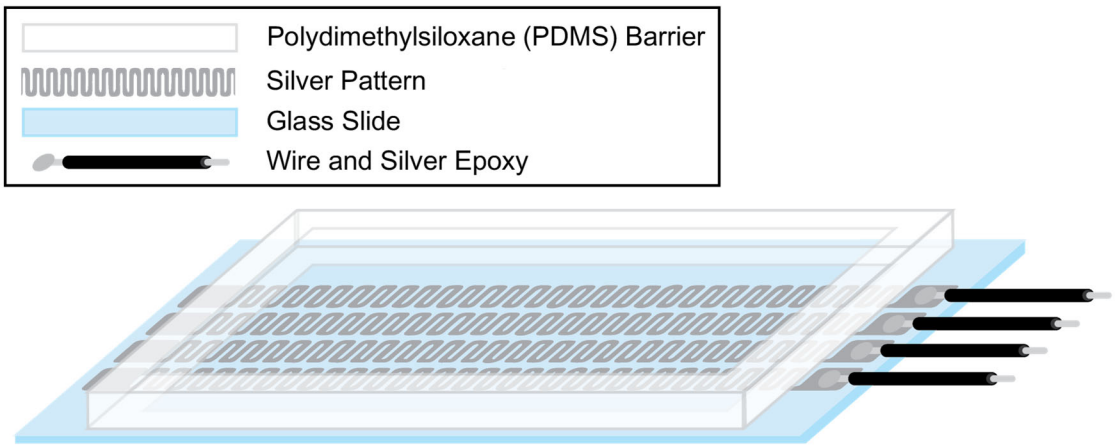

Figure 7. Illustration of the final glass slide with silver electrodes and PDMS well

2.3 Bacteria growth procedure

Staphylococcus epidermidis was chosen for this study because it is a wound-relevant bacteria and has been previously studied by our group[107, 108]. One colony of *S. epidermidis* was removed from a culture plate using an inoculation loop, then added to 25 mL of Tryptic Soy broth (TSB). The solution was then incubated in a shaker incubator at 37˚C for 18 hours. After incubation, the solution was diluted with additional TSB at a 1:100 ratio and was used immediately or refrigerated for up to 48 hours before use.

Petri dishes containing a 1.4 mm thick tryptic soy agar (TSA) layer were prepared and refrigerated upside-down until they were needed. For 9 cm plates, 8.9 mL of TSA was used. Two 1" x 2" rectangles were traced onto the outside of the petri dishes, which matches the size of the opening in the PDMS well. Then 165 μL of diluted *S. epidermidis* solution was spread onto the surface of the TSA using a cell spreader. The bacteria solution was dried for 30 minutes then placed upside-down in an incubator at 37˚C for either 8, 16, or 24 hours. Experiments were also performed immediately after the 30-minute drying period and were referred to as 0 hours of growth.

2.4 Electrochemical impedance spectroscopy measurements

After devices were completed, plain TSA or TSA and biofilm were added to the devices for EIS measurements. This was performed by cutting out the media along the rectangles drawn on the petri dishes, then lifting out the media with biofilm on top and placing it into the well made by the PDMS. The TSA would directly cover the electrodes and the biofilm, if used in the sample, would be on top of the TSA. Photos of a petri dish with biofilm grown and the media moved into a device are provided in Figure 8.

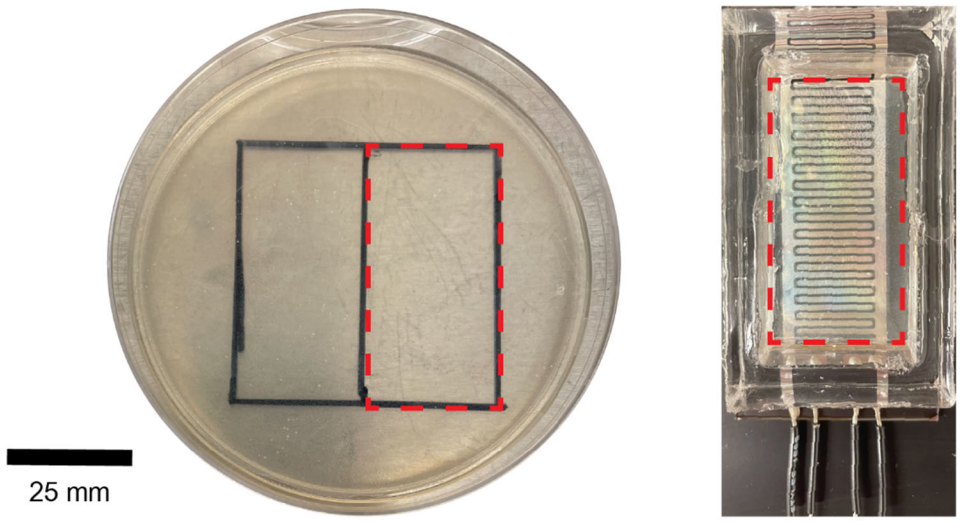

Figure 8. Photos showing an example of a dish with biofilm, the region removed from the dish, and the region placed into a device.

Within an hour of media being added to the devices, completed devices were connected to an Interface 1000 Potentiostat (Gamry Instruments) to perform potentiostatic EIS experiments. Figure 9 depicts the electrode connections for both a 2-electrode device and a 4-electrode device. Each device was used for three repeated potentiostatic EIS experiments to account for slight error between measurements. Devices were discarded after use. We selected our EIS parameters based on the prior articles discussed in section 1.6. Our AC excitation voltage was selected at the lower end, 10 mV, as in Kim et. al[19], Fraiwan et. al[21], Bharatula et. al[23], and Romero et. al[24]. Our frequency range was selected to encompass the range of frequencies used in these studies, from 1 Hz to 350 kHz. Initially 500 kHz was used, but the final frequencies were eliminated from measurements after early testing showed that the system did not change past 300 kHz. Frequency values below 1 Hz were not tested because there were no major changes observed in the system observed at lower frequencies. In addition to experimental

conditions, the equivalent circuits described by these articles are used as the baseline for analysis in our experiments. Table 3 summarizes the input parameters for the potentiostat.

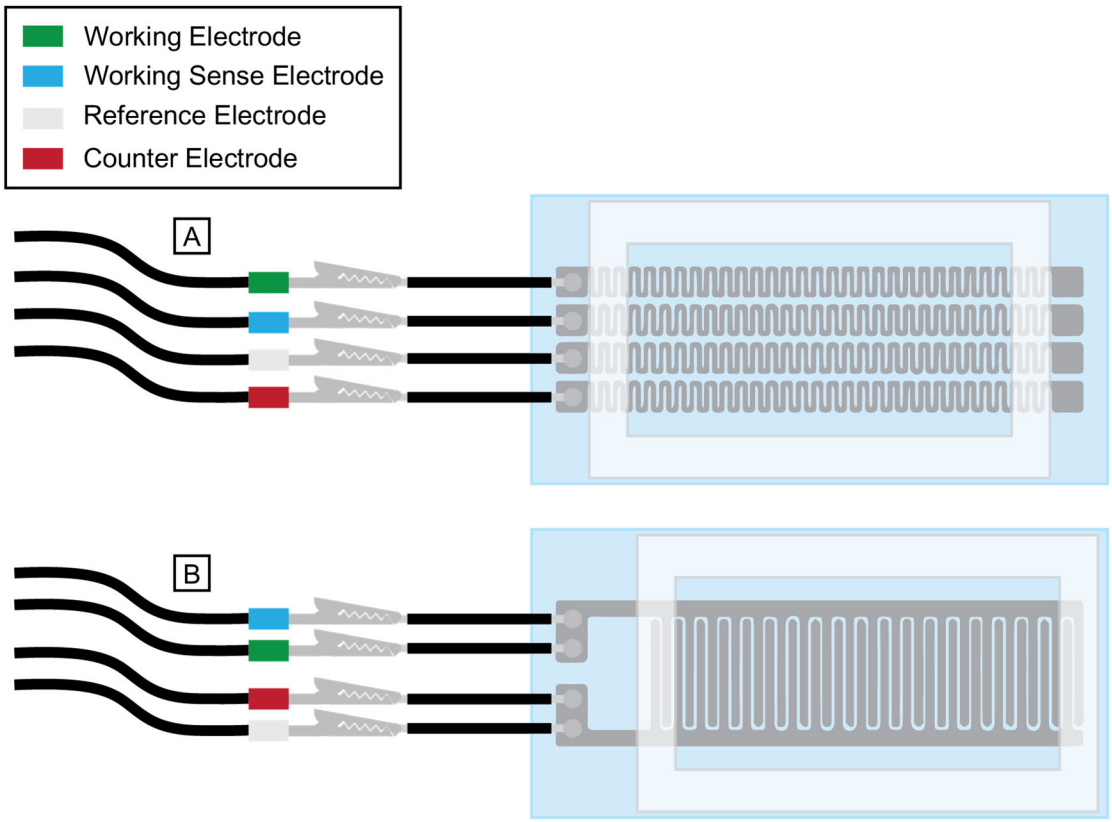

Figure 9. Diagrams of the potentiostatic EIS connections for the (A) 4-electrode device design and the (B) interdigitated 2-electrode device design

Table 3. Parameters used for potentiostatic EIS experiments

Parameter Name	**Value**
Initial Frequency	1 Hz
Final Frequency	350 kHz
Points per Decade	10
AC Excitation Voltage	10 V

Chapter 3. Results and Discussion

3.1 Iterations of device design

The device presented in this thesis underwent multiple iterations before being finalized for data collection. This section will present some of the key steps in the design process and will serve as a guide for future lab members as they continue to improve the device.

3.1.1 Substrate materials

Our group has previously reported on additional devices which use silver as the electrode material because of its compatibility with biological interfaces and its conductivity[12, 13, 30, 109]. We decided to continue using silver because it will allow the group to easily relate the knowledge gained from this project to that of previous projects.

For the base of the device, 38 mm x 76 mm x 1 mm glass slides were chosen to allow for ample surface area above the electrodes for biofilm growth. The electrodes were positioned at the center of the glass slides with room on each side, and most of the area covered by the PDMS wells were plasma bonded to the clear space on the glass slides. Only the shorter sides of the PDMS wells overlapped onto the electrodes.

3.1.2 Electrode photolithography

There are multiple photolithography processes that would provide similar final products. The first photolithography process we used was to evaporate silver first, then

apply a positive photoresist and use a metal etchant to remove silver that was not protected by the photoresist. After etching, the remaining photoresist was removed. This process allowed the edges of the glass slide to be cleaner, but there was more variability in the electrode dimensions due to the inconsistent etching time. If the etching process went too long, the etchant could flow underneath the photoresist and etch further than desired. The etchant solution itself also posed other challenges because it was difficult to mix consistently when diluted. This resulted in some slides being etched faster than others, making it difficult to decide a consistent etching time.

The next fabrication process we tested was a solvent lift-off process. This process started by applying a negative photoresist to a clean glass slide, so that after developing, photoresist was only applied to the areas that would not have silver. In the first trials of this method, a photomask was printed using a 1200 x 1200 dpi office printer (HP Color LaserJet Enterprise m553). This mask was replaced with a chrome photomask because the printed photomask was not close enough to the nominal dimensions of the pattern. The chrome mask was fabricated as described in Appendix A.4. Figure 10 shows microscope images of the two different photomasks and the resultant substrates from using each photomask.

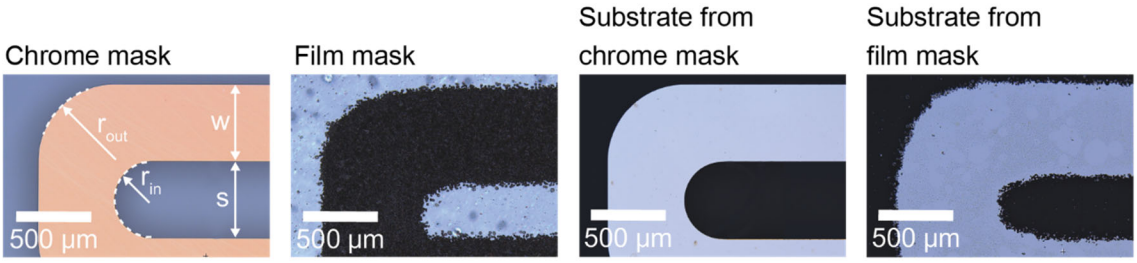

Figure 10. Microscope images of each photomask used and the resultant substrate appearance. Each region – inner radius (r_{in}), outer radius (r_{out}), width (w), and spacing (s) – were measured at multiple locations on each sample.

Table 4 provides measurements as supplement for Figure 10. For the masks, the measurements of each region were taken at four locations on the mask and the average is provided. A total of 20 measurements of each region across five samples are averaged for the film mask substrate. A total of 32 measurements of each region across eight samples are averaged for the chrome mask substrate.

Table 4. Measurements of substrates fabricated with printed mask and chrome mask compared to nominal dimensions. Values are rounded to the nearest tenth of a micron.

	Width (µm)	**Spacing (µm)**	**Inner Radius (µm)**	**Outer Radius (µm)**
Nominal Design	500	500	250	500
Film Mask	606.3 ± 6.5	390.5 ± 15.9	187.7 ± 10.0	560.9 ± 25.7
Chrome Mask	496.8 ± 2.0	503.7 ± 2.2	251.4 ± 0.8	500.9 ± 0.9
Film Mask Substrate	584.1 ± 11.9	405.0 ± 20.4	183.2 ± 9.5	547.0 ± 28.6
Chrome Mask Substrate	496.7 ± 1.6	503.0 ± 1.6	252.2 ± 0.8	500.5 ± 1.7

3.1.3 Number of electrodes

As described in section 1.5.1, there are several things to consider when choosing the number of electrodes for an EIS experiment. The type of media being measured, the way in which it is prepared, and the type of data desired are all details that contribute to the final decision. In this thesis, we have designed two different electrode setups so that multiple types of data can be obtained. Two-electrode measurements are common in EIS studies of biofilms, as seen in Table 2 in section 1.5.3. While 4-electrode experiments are rarely used to study biofilms, it will allow us to collect different types of information.

3.2 EIS measurements on TSA only

3.2.1 Two-electrode experiments

To verify the functionality of the devices, we first performed potentiostatic EIS experiments with only TSA in the devices. For the two-electrode devices, three samples were used, and each sample had EIS measurements performed three times in a row to account for any small errors during the experiment itself. Only samples that successfully completed three runs of EIS experiments were used in the final data analysis. Then, this data was averaged into each individual sample. In Figures 11 through 14, the overall average across all samples is shown as each data point, and the error bars show the standard deviation across all experiment runs. Figures 11 and 12 show the overall average magnitude and phase of impedance measured from TSA as Bode plots. Figures 13 and 14 show the overall average real and imaginary impedance values measured from TSA as Nyquist plots. Two plots are used to avoid clutter with overlapping error bars. The averaged plots from each sample are provided in Appendix C.1. The MATLAB code used for creating the following plots is provided in Appendices B.2 and B.3.

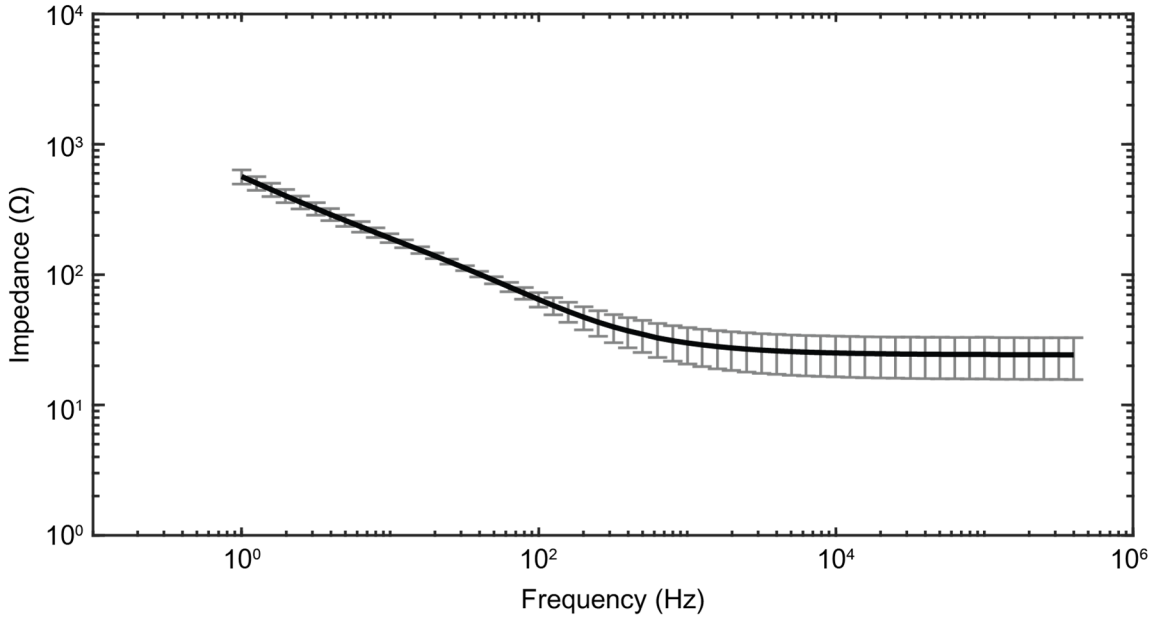

Figure 11. Bode plot depicting the impedance magnitude of TSA across a range of frequencies using the two-electrode EIS setup. Mean ± 1 standard deviation, n = 3 plates measured each 3 times for a total of 9 measurements. The data is reported as the average of these 9 measurements with the associated standard deviation.

The magnitude Bode plot for TSA measured on the two-electrode device in Figure 11 shows that TSA behaves similar to a resistor and capacitor in series. The corner frequency, or highest frequency at which the imaginary and real components of the impedance were equal in magnitude[110], was calculated to be approximately 760.9 ± 144.3 Hz. These calculations are provided in a MATLAB script in appendix B.2. This was calculated by fitting two lines to the average magnitude Bode plot data of each set from 1 – 100 Hz and from 10 – 350 kHz, then finding the intersect of those lines. The TSA actually behaves as a constant-phase element (CPE), which was also described in some of the prior research discussed in section 1.6. A CPE is a frequency-dependent passive circuit element with real and imaginary impedance components of constant proportion. Due to the constant proportionality between the real and imaginary impedance components, the phase when

converted to polar units remains constant. The total magnitude of a CPE will vary with frequency. The impedance of a constant phase element is represented in equation 3, where C_{eff} is the effective capacitance and α is the fit parameter[105].

$$Z_{CPE} = \frac{1}{(j\omega C_{eff})^{\alpha}} \quad [3]$$

The imaginary component dominates the frequency response until it reaches the final real value and the imaginary component continues to decrease while the real component stays constant. The smaller standard deviation at earlier frequencies indicates that the CPE behavior is consistent across samples. The larger standard deviation after the corner frequency indicates that the final resistive component was more variable across samples. The final average impedance was 24.2 ± 8.6 Ω.

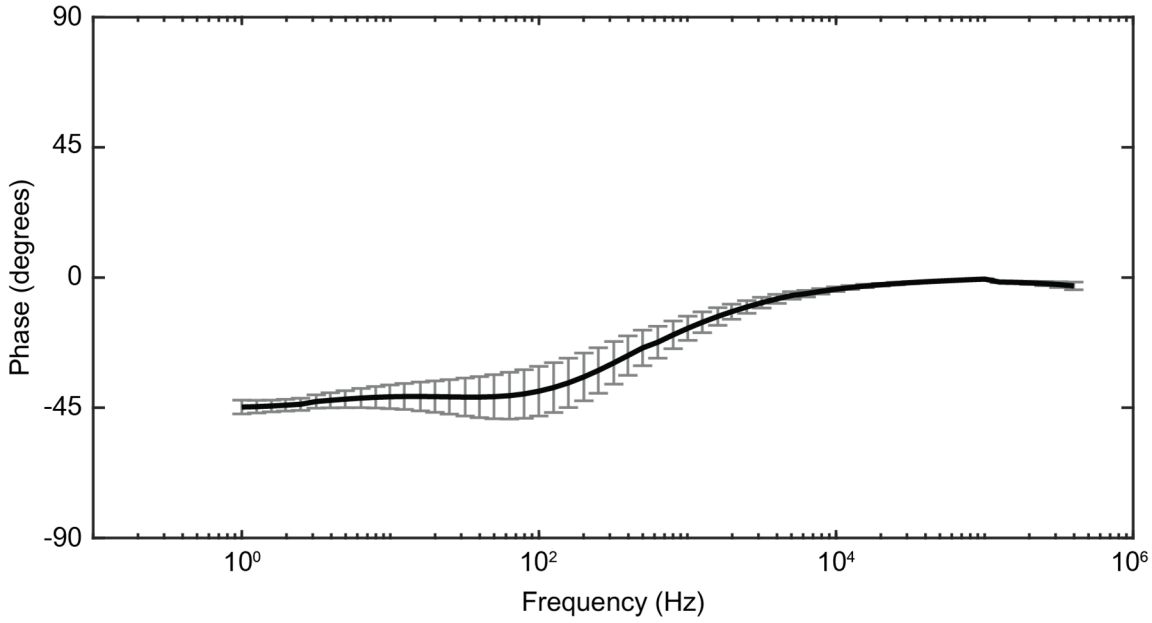

Figure 12. Bode plot depicting the impedance phase of TSA across a range of frequencies using the two-electrode EIS setup. Mean ± 1 standard deviation, n = 3 plates measured each 3 times for a total of 9 measurements. The data is reported as the average of these 9 measurements with the associated standard deviation.

The phase Bode plot of TSA measured on the two-electrode device in Figure 12 also supports the analysis that TSA is a CPE. At lower frequencies, the average phase is approximately -45˚, which is halfway between the phase of a capacitor, -90˚, and the phase of a resistor, 0˚. Specifically, a CPE at -45˚ is referred to as a Warburg element, which models semi-infinite linear diffusion[111]. In reference to equation 3, a Warburg element has a fit of $\alpha = 0.5$, because $\alpha = 1$ corresponds to a perfect capacitor, and $\alpha = 0$ corresponds to a perfect resistor[105]. The frequency-dependent resistive value holds the phase at -45˚. By finding the average phase from 1 Hz to 100 Hz, the actual phase for the CPE is -42.0 ± 4.6˚. After the corner frequency calculated with data from the magnitude Bode plot (760.9 ± 144.3 Hz), the resistive component takes over and the phase settles at approximately 0˚. The larger bands of standard deviation close to the corner frequency can be attributed to the similarity of the imaginary and real component magnitudes. As the values fluctuate, whichever magnitude is greatest at each frequency temporarily dominates the phase.

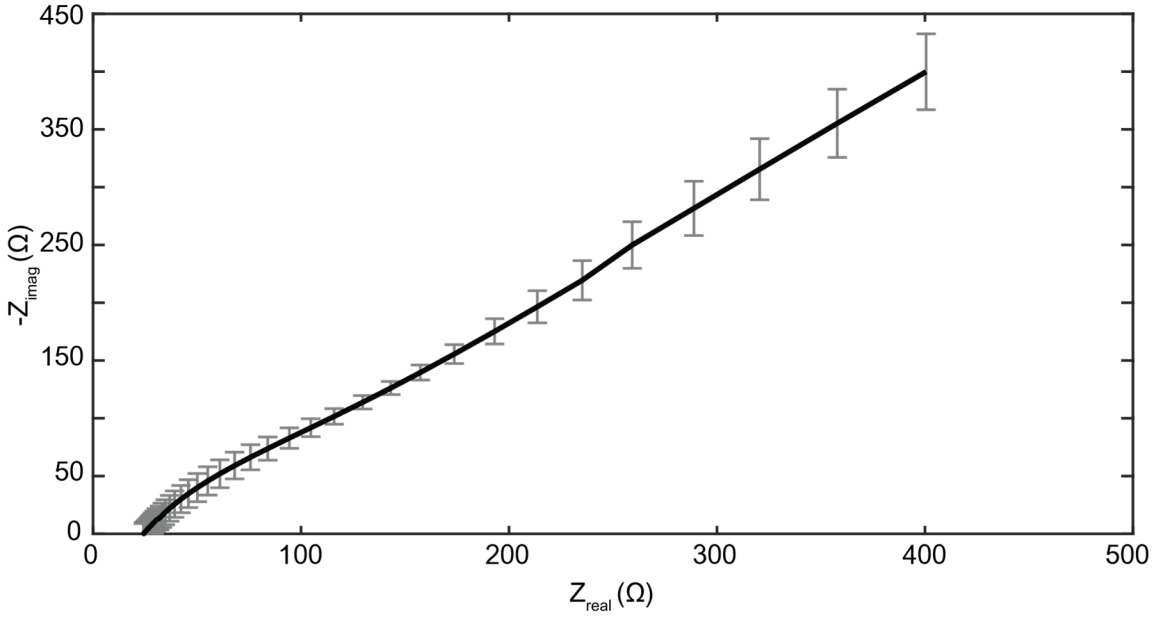

Figure 13. Nyquist plot depicting the real and imaginary impedance of TSA across a range of frequencies using the two-electrode EIS setup. Mean ± 1 standard deviation, n = 3 plates measured each 3 times for a total of 9 measurements. The data is reported as the average of these 9 measurements with the associated standard deviation.

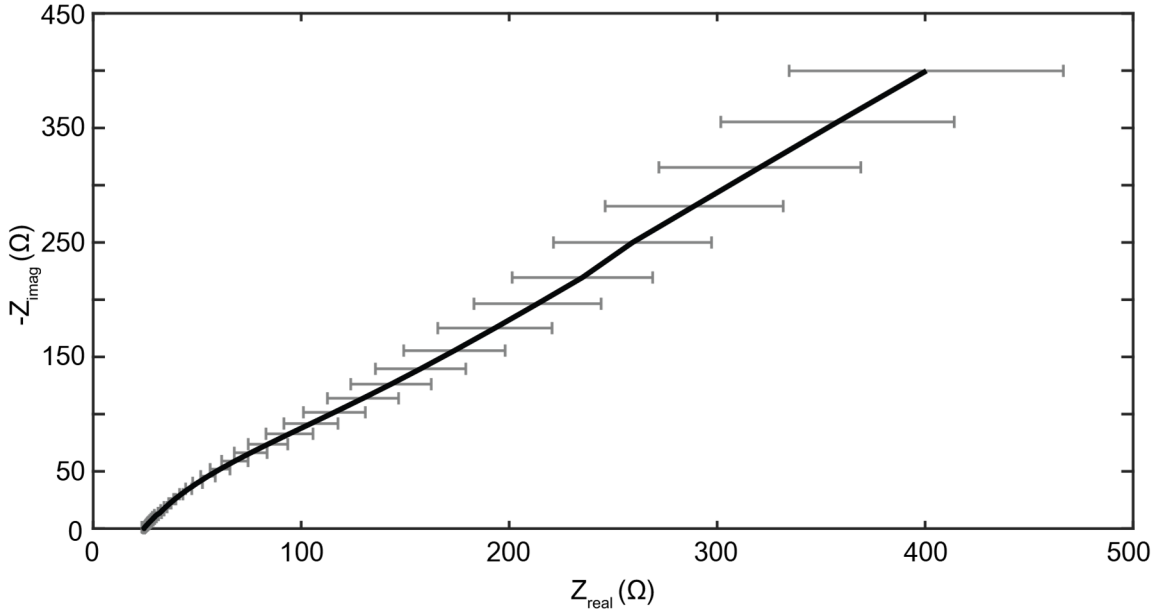

Figure 14. Nyquist plot depicting the real and imaginary impedance of TSA across a range of frequencies using the two-electrode EIS setup. Mean ± 1 standard deviation, n = 3 plates measured each 3 times for a total of 9 measurements. The data is reported as the average of these 9 measurements with the associated standard deviation.

The Nyquist plots of TSA measured on the two-electrode devices in Figures 13 and 14 are also clear indicators of a Warburg element in the system. At the left side of the plot, the point intersecting with the Z_{real} axis is equal to the final real value calculated from Figure 11. As the frequency decreases (moving right on the graph), the magnitude of the real and imaginary components increase and are approximately equal. The equal magnitude indicates that this is a diffusion-limited reaction, or reaction limited by the rate at which reactants are transported through the media[112, 113]. In both plots, the standard deviation increases as the frequency decreases. The largest standard deviation of the imaginary values was smaller than that of the real values, which corresponds to the larger standard deviation that occurred at the right side of the magnitude Bode plot in Figure 11. These results align with Nyquist plots of other gels such as sol-gel[114, 115], other agar mixtures[116], and other hydrogels[117], which show a small kinetic region (curve or semicircle) followed by a diffusional region (straight line).

3.2.2 Four-electrode experiments

For the four-electrode measurements, four samples were used, and EIS was again performed three times for each sample. Only the samples that successfully completed three EIS experiment runs were used in the data analysis. Figures 15 and 16 show the overall Bode plots and Figures 17 and 18 show the overall Nyquist plots. These plots also use the same error convention as Figures 11 through 14. The averaged plots from each sample are provided in Appendix C.2.

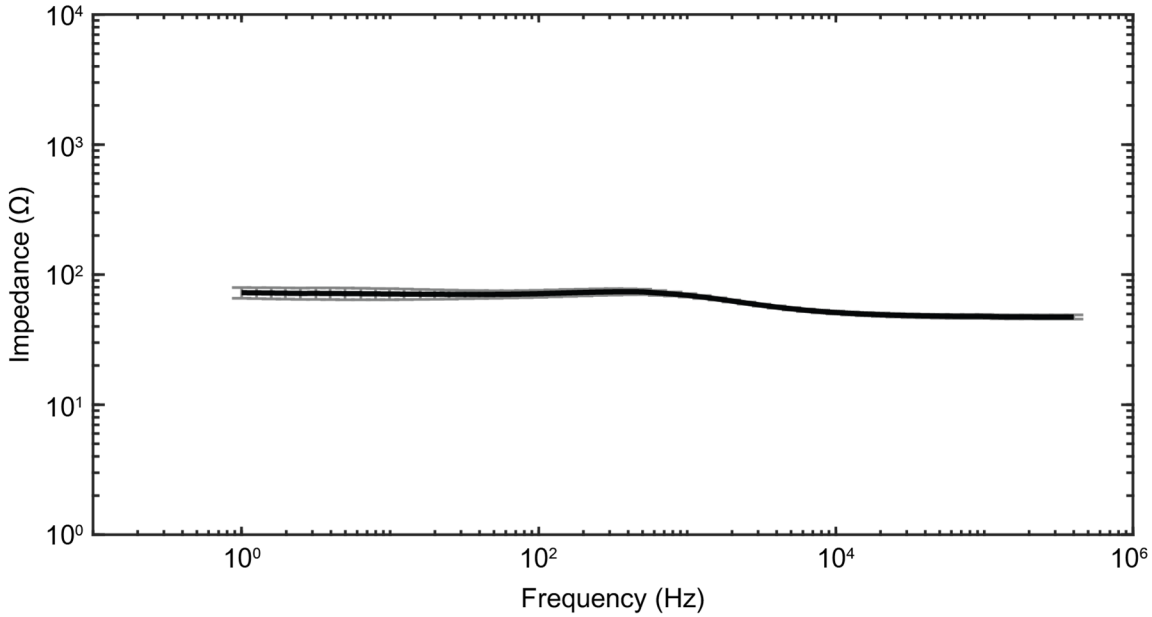

Figure 15. Bode plot depicting the impedance magnitude of TSA across a range of frequencies using the four-electrode EIS setup. Mean ± 1 standard deviation, n = 4 plates measured each 3 times for a total of 12 measurements. The data is reported as the average of these 12 measurements with the associated standard deviation.

The magnitude Bode plot of TSA measured on the four-electrode device in Figure 15 had a much smaller change than that of the two-electrode measurements. The plot consists of a flat region, then a short, sloped region, and finally another flat region. Each flat region corresponds to a constant resistive element that dominates the system at those frequencies, and in the sloped region, a capacitive element dominates the system. The magnitudes measured at 1 Hz and 350 kHz were 72.6 ± 6.9 **Ω** and 47.3 ± 1.7 **Ω**, respectively.

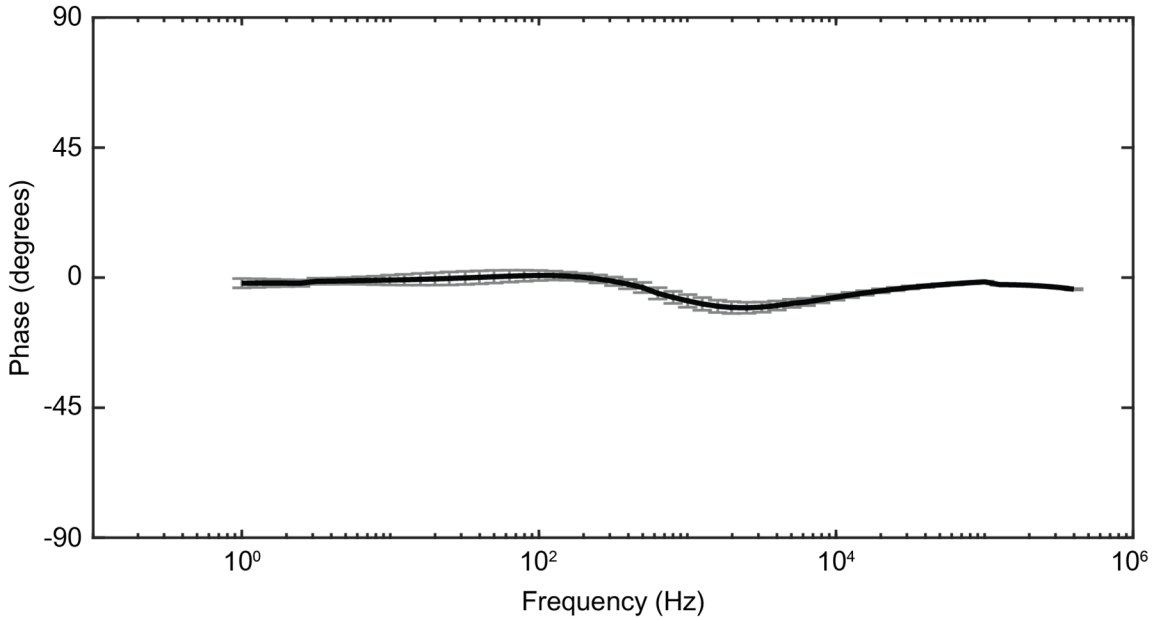

Figure 16. Bode plot depicting the impedance phase of TSA across a range of frequencies using the four-electrode EIS setup. Mean ± 1 standard deviation, n = 4 plates measured each 3 times for a total of 12 measurements. The data is reported as the average of these 12 measurements with the associated standard deviation.

The phase Bode plot of TSA measured on the four-electrode device in Figure 16 shows that the system is even more complex and includes inductive elements as well. At the smallest and largest frequencies measured, the phase rests close to 0˚, which corresponds to the resistive elements apparent in the magnitude Bode plot. Towards the middle frequencies, an amount of variance occurs. Since the phase changes from positive to negative values, both a capacitive and inductive component are present in the system.

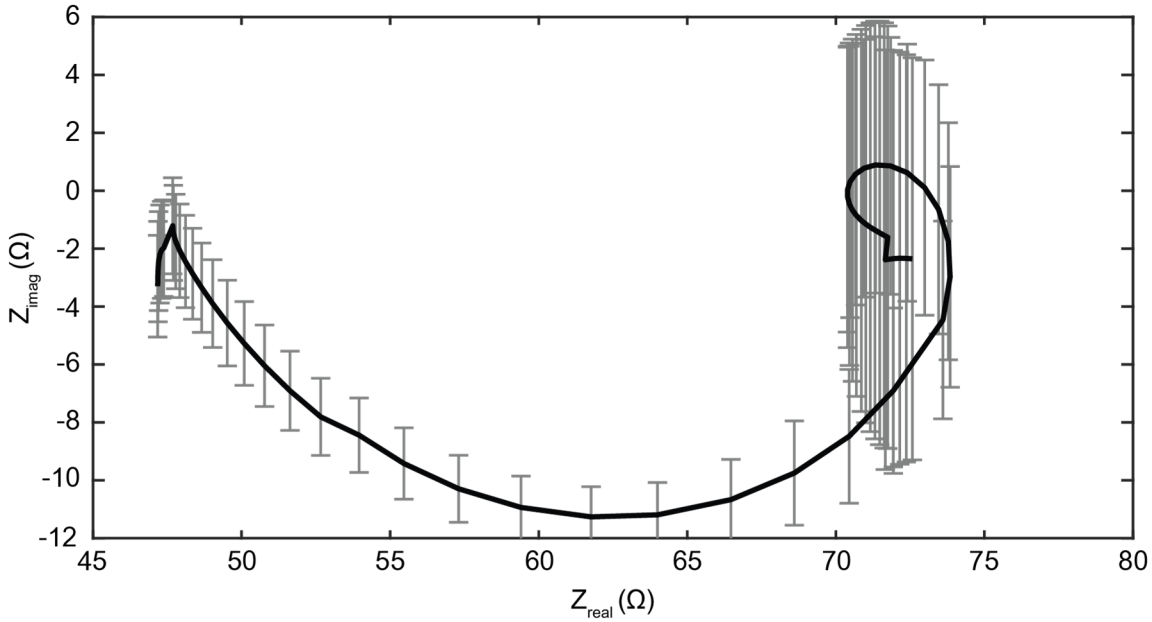

Figure 17. Nyquist plot depicting the real and imaginary impedance of TSA across a range of frequencies using the four-electrode EIS setup. Mean ± 1 standard deviation, n = 4 plates measured each 3 times for a total of 12 measurements. The data is reported as the average of these 12 measurements with the associated standard deviation.

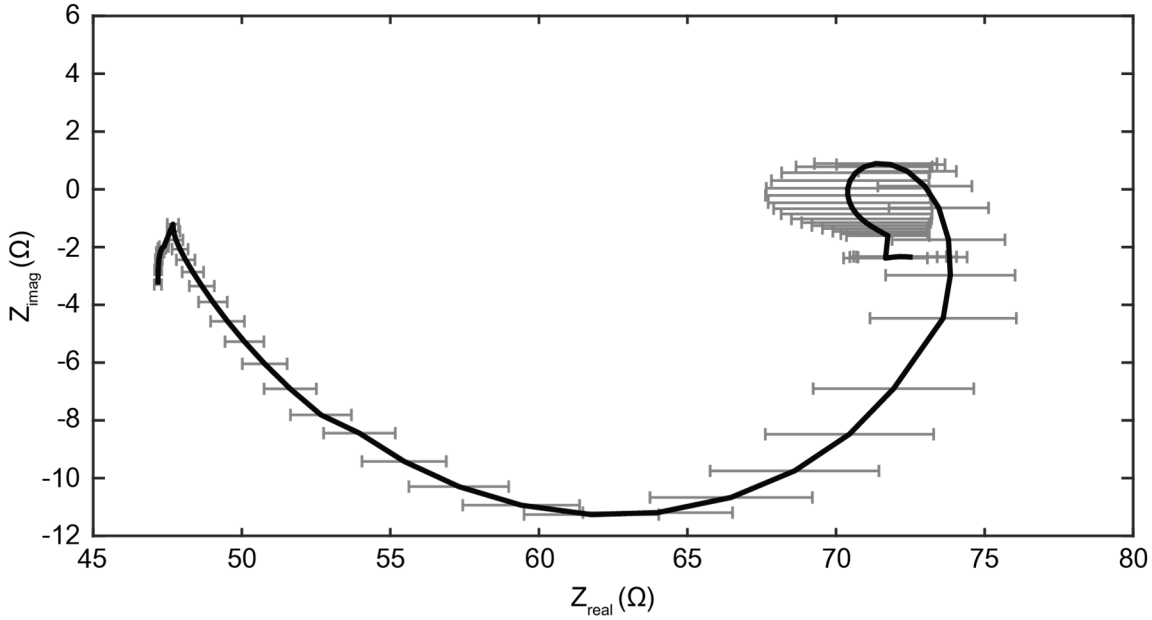

Figure 18. Nyquist plot depicting the real and imaginary impedance of TSA across a range of frequencies using the four-electrode EIS setup. Mean ± 1 standard deviation, n = 4 plates measured each 3 times for a total of 12 measurements. The data is reported as the average of these 12 measurements with the associated standard deviation.

The Nyquist plots of TSA measured on the four-electrode device in Figures 17 and 18 introduced a great deal of variance in the measurements, as shown by the standard deviation error bars. Each sample had the semicircular pattern in the negative Z_{imag} and positive Z_{real} quadrant that corresponds to a resistor and capacitor in series at the higher frequencies. At lower frequencies, the Nyquist plots had a semicircular pattern in the positive Z_{imag} and positive Z_{real} quadrant that corresponds to a resistor and inductor in parallel. The wide range of standard deviation across samples at lower frequencies shows that the inductive component was varied across all samples.

Due to the complexity of a potential equivalent circuit, inconsistency between samples, and lack of publications with similar EIS setups, the two-electrode device was selected as the device used for all biofilm EIS measurements.

3.3 EIS measurements on *S. epidermidis* biofilm

Following the verification of the device, the next step was to analyze the electrochemical response of the system after 0, 8, 16, and 24 hours of biofilm growth. For each growth period, 3 or 4 samples were used in the final data analysis depending on if the sample successfully completed three experiment cycles. Each of the 0-hour, 16-hour, and 24-hour data sets were calculated using three distinct samples each. Four samples were used for the 8-hour biofilm results because additional data was collected to verify trends. The error bars shown on all graphs are the standard deviation across the average values of each sample.

There were several difficulties early in the biofilm data collection. Initially, we attempted to grow biofilm directly in the devices rather than growing the biofilm on plates

and moving it into the devices. However, this was often unsuccessful because placing the devices upside-down in the incubator prevented them from receiving adequate oxygen movement. Even when tape was used to hold the devices up and leave space for air movement, the device shape made it difficult to adequately spread the appropriate volume of *S. epidermidis* solution evenly on the TSA surface. Using a cell spreader on a very small volume resulted in too much of the solution staying on the cell spreader after it was used. To counteract this, we tried slowly rotating the device to spread the solution, but that resulted in an uneven biofilm layer, as shown in Figure 19.

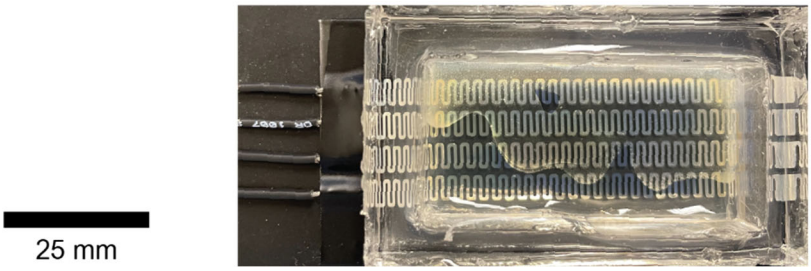

Figure 19. Photo showing the appearance of a biofilm grown inside the device where the *S. epidermidis* solution was spread by rotating the device.

3.3.1 0 hours of biofilm growth

Figures 20-23 provide the Bode and Nyquist plots for the average of all 0-hour biofilm samples. The averaged plots from each sample are provided in Appendix C.3.

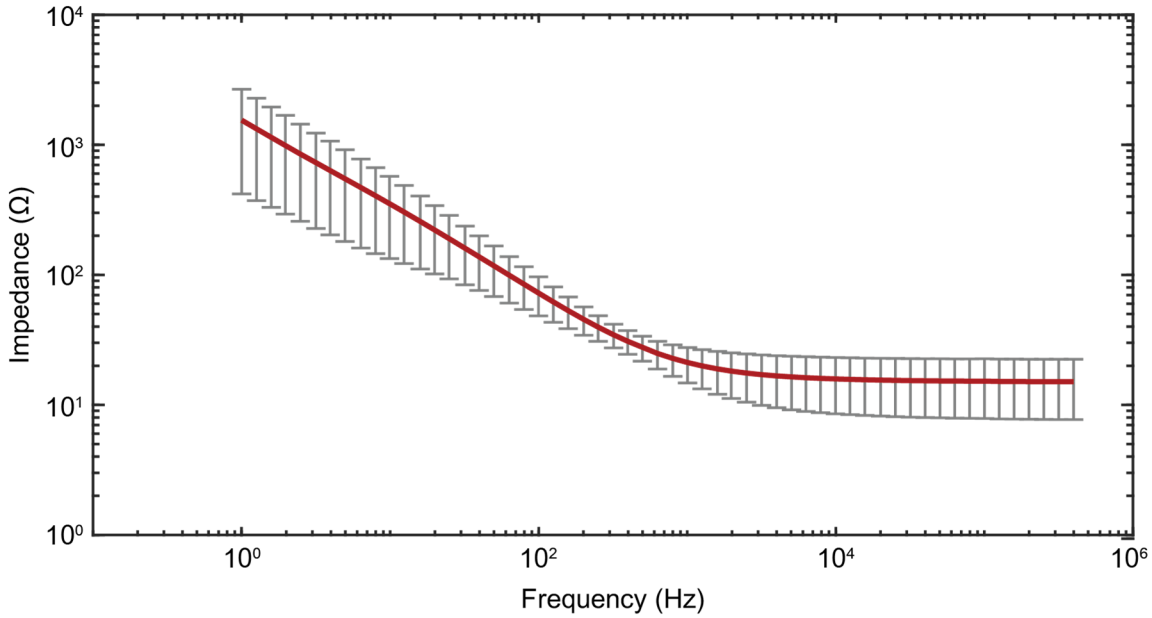

Figure 20. Bode plot depicting the impedance magnitude of *S. epidermidis* biofilm incubated for 0 hours across a range of frequencies using the two-electrode EIS setup. Mean ± 1 standard deviation, n = 3 plates measured each 3 times for a total of 9 measurements. The data is reported as the average of these 9 measurements with the associated standard deviation.

The magnitude Bode plot in Figure 20 was similar in shape to the TSA-only Bode plot in Figure 11. The sloped region indicates a CPE in the system and the flat region corresponds to a resistive component. The final impedance magnitude was 15.1 ± 7.4 **Ω**, and the corner frequency was located at 1018.4 ± 803.5 Hz.

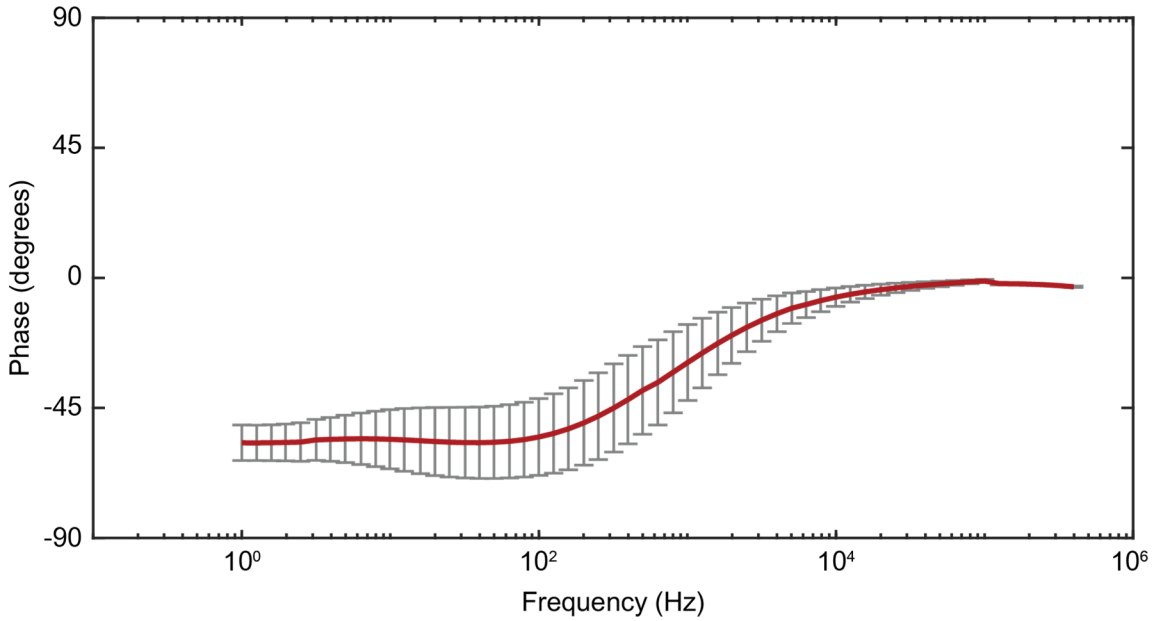

Figure 21. Bode plot depicting the impedance phase of *S. epidermidis* biofilm incubated for 0 hours across a range of frequencies using the two-electrode EIS setup. Mean ± 1 standard deviation, n = 3 plates measured each 3 times for a total of 9 measurements. The data is reported as the average of these 9 measurements with the associated standard deviation.

In Figure 21, the phase Bode plot of the 0-hour measurements is also similar to the phase Bode plot in Figure 12. The CPE is not a Warburg element in this system because the phase is below -45˚, meaning that the imaginary component in the CPE is larger. Using the same range of 1 Hz to 100 Hz, the average phase of the CPE is -56.4 ± 9.8˚. Even though the standard deviation is larger than that of the TSA-only samples, the trends are still consistent. First, the CPE is dominant, and the phase is consistently below -45˚, then the phase increases with frequency until the resistive element is dominant and the phase settles close to 0˚.

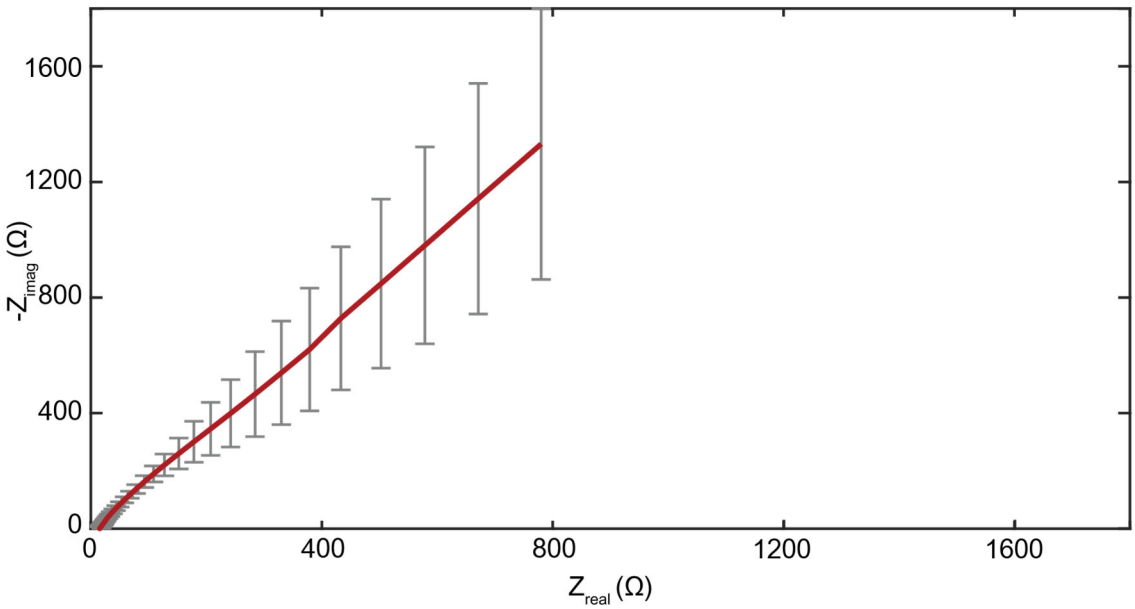

Figure 22. Nyquist plot depicting the real and imaginary impedance of *S. epidermidis* biofilm incubated for 0 hours across a range of frequencies using the two-electrode EIS setup. Mean ± 1 standard deviation, n = 3 plates measured each 3 times for a total of 9 measurements. The data is reported as the average of these 9 measurements with the associated standard deviation.

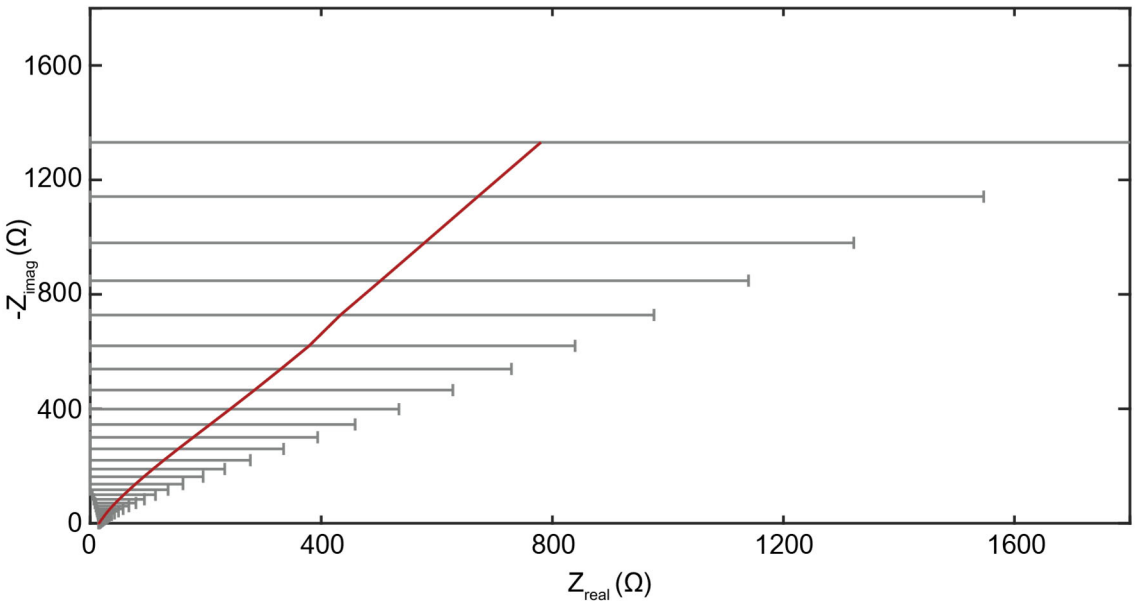

Figure 23. Nyquist plot depicting the real and imaginary impedance of *S. epidermidis* biofilm incubated for 0 hours across a range of frequencies using the two-electrode EIS setup. Mean ± 1 standard deviation, n = 3 plates measured each 3 times for a total of 9 measurements. The data is reported as the average of these 9 measurements with the associated standard deviation.

In Figures 22 and 23, the variation between samples is very apparent. Most notably, the standard deviation of the real impedance is very large because of the high amount of variability between 0-hour biofilms despite using the same overnight culture for all three samples. The average Nyquist plot corresponds to the Bode plots and shows that the system is also a diffusion-limited reaction with an angle greater in magnitude than -45˚. The average impedance was also closest to the TSA-only samples. The point where the Nyquist plot meets the Z_{real} axis also corresponds to the final impedance magnitude value of 15.1 ± 7.4 **Ω**.

3.3.2 8 hours of biofilm growth

Figures 24-27 provide the Bode and Nyquist plots for the average of all 8-hour biofilm samples. The averaged plots from each sample are provided in Appendix C.4.

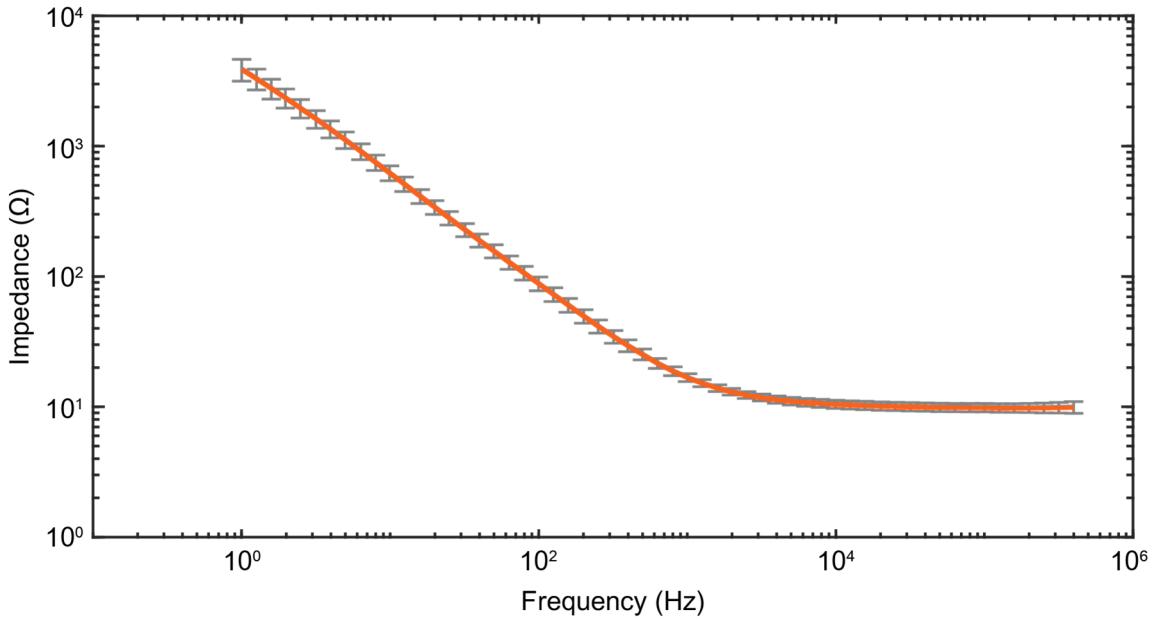

Figure 24. Bode plot depicting the impedance magnitude of *S. epidermidis* biofilm incubated for 8 hours across a range of frequencies using the two-electrode EIS setup. Mean ± 1 standard deviation, n = 4 plates measured each 3 times for a total of 12 measurements. The data is reported as the average of these 12 measurements with the associated standard deviation.

After 8 hours of biofilm growth, the EIS measurements became much more consistent across samples, as shown by the small standard deviation. In Figure 24, the magnitude Bode plot again shows a CPE at lower frequencies and a resistive element becoming dominant at higher frequencies. The corner frequency was calculated to be 1285.6 ± 247.3 Hz and the final average impedance magnitude value was 9.9 ± 1.0 Ω.

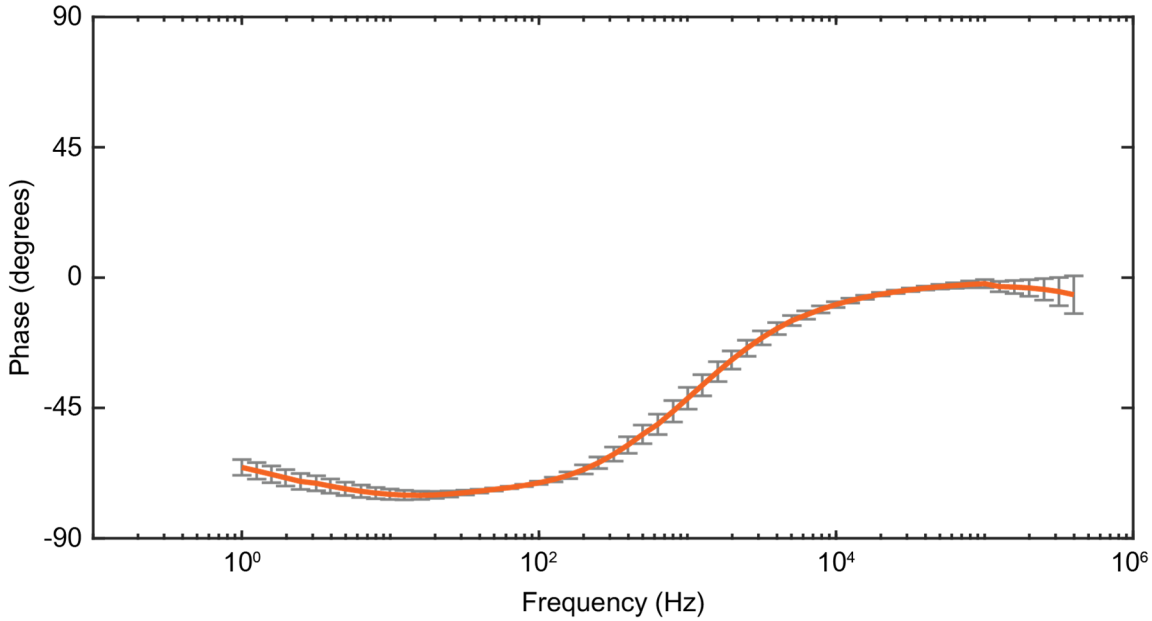

Figure 25. Bode plot depicting the impedance phase of *S. epidermidis* biofilm incubated for 8 hours across a range of frequencies using the two-electrode EIS setup. Mean ± 1 standard deviation, n = 4 plates measured each 3 times for a total of 12 measurements. The data is reported as the average of these 12 measurements with the associated standard deviation.

The phase Bode plot shows that the CPE in the 8-hour biofilm samples was less consistent than that of the TSA-only and 0-hour biofilm samples. The curve at earlier frequencies indicates that the imaginary component was always the dominating component of the phase, but the magnitude of the imaginary component was larger when the phase moves closer to -90˚. The phase measured less than -45˚ until the corner frequency, at

which the phase increases past -45˚ and the resistive component of impedance dominates the phase. The average phase from 1 Hz to 100 Hz was -72.1 ± 1.7˚.

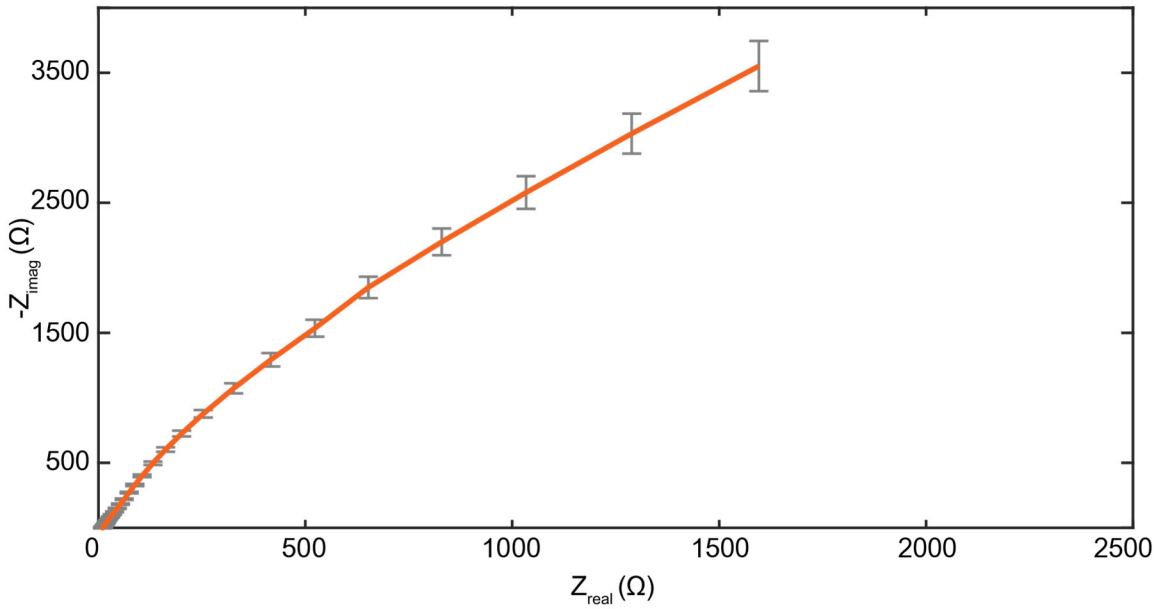

Figure 26. Nyquist plot depicting the real and imaginary impedance of *S. epidermidis* biofilm incubated for 8 hours across a range of frequencies using the two-electrode EIS setup. Mean ± 1 standard deviation, n = 4 plates measured each 3 times for a total of 12 measurements. The data is reported as the average of these 12 measurements with the associated standard deviation.

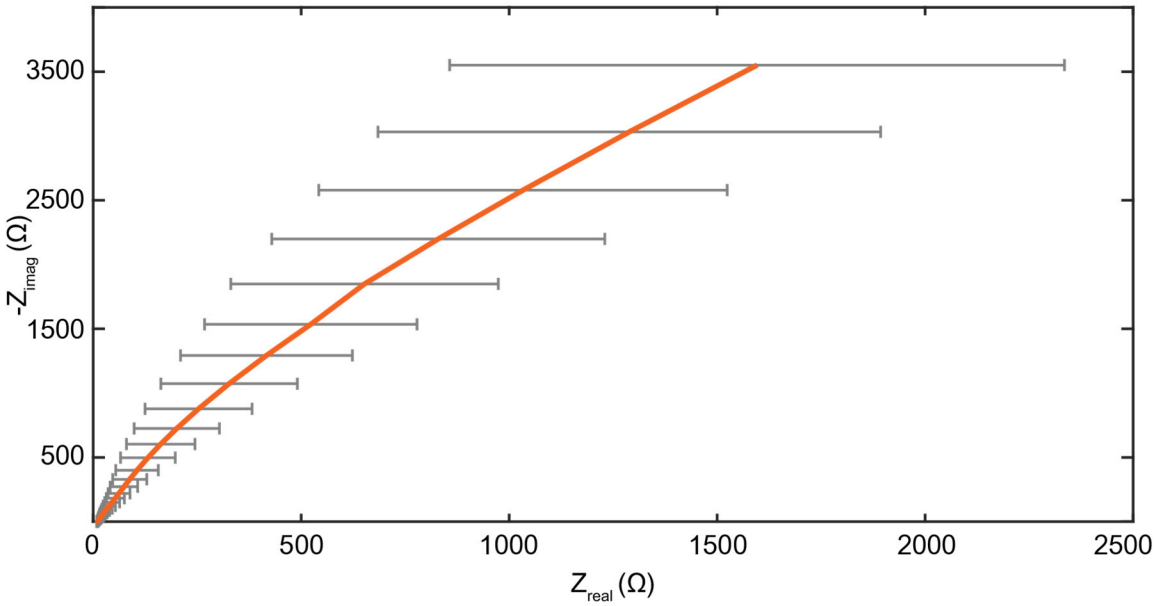

Figure 27. Nyquist plot depicting the real and imaginary impedance of *S. epidermidis* biofilm incubated for 8 hours across a range of frequencies using the two-electrode EIS setup. Mean ± 1 standard deviation, n = 4 plates measured each 3 times for a total of 12 measurements. The data is reported as the average of these 12 measurements with the associated standard deviation.

The Nyquist plots in Figures 26 and 27 further support the evidence for a CPE in the 8-hour biofilm system. The largest standard deviation comes from the resistive component at low frequencies, as was the case with the TSA-only and 0-hour biofilm samples. The point at which the plot intersects the Z_{real} axis is 9.9 ± 1.0 Ω, matching the frequency-invariant impedance magnitude calculated from the Figure 24 Bode plot.

3.3.3 16 hours of biofilm growth

Figures 28-31 provide the Bode and Nyquist plots for the average of all 16-hour biofilm samples. The averaged plots from each sample are provided in Appendix C.5.

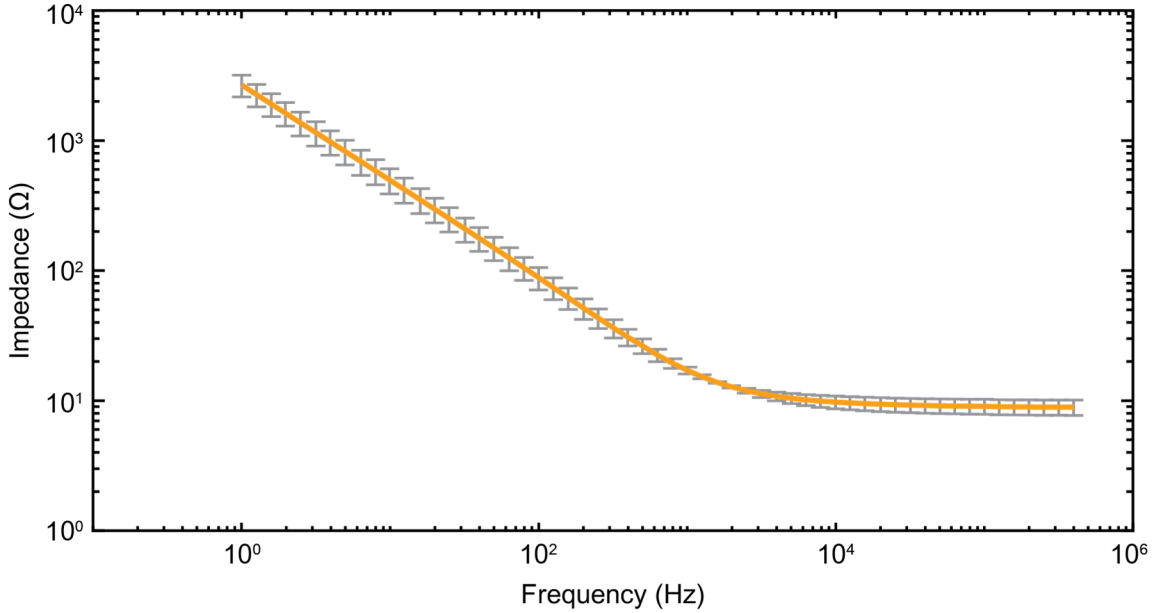

Figure 28. Bode plot depicting the impedance magnitude of *S. epidermidis* biofilm incubated for 16 hours across a range of frequencies using the two-electrode EIS setup. Mean ± 1 standard deviation, n = 3 plates measured each 3 times for a total of 9 measurements. The data is reported as the average of these 9 measurements with the associated standard deviation.

In Figure 28, the magnitude Bode plot of the 16-hour biofilms has a similar shape to that of the TSA-only two-electrode measurements. This growth duration also had small standard deviation across all measured frequencies, similar to the measurements of the 8-hour biofilms. The corner frequency was calculated at 1959.3 ± 1198.2 Hz and the final impedance magnitude was 8.9 ± 1.2 Ω.

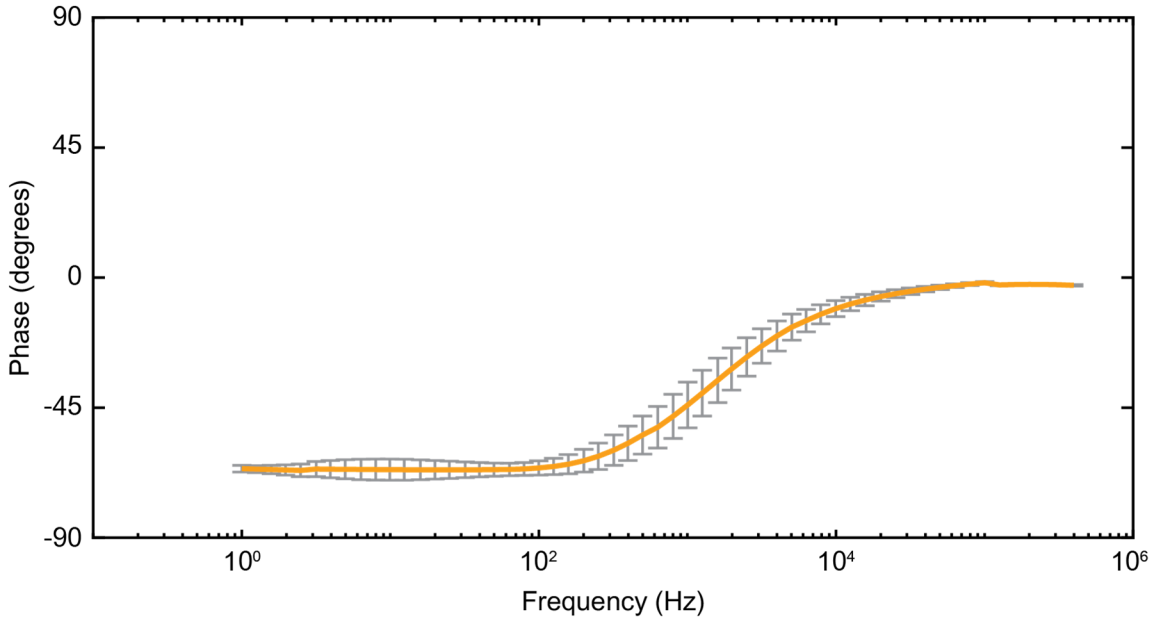

Figure 29. Bode plot depicting the impedance phase of *S. epidermidis* biofilm incubated for 16 hours across a range of frequencies using the two-electrode EIS setup. Mean ± 1 standard deviation, n = 3 plates measured each 3 times for a total of 9 measurements. The data is reported as the average of these 9 measurements with the associated standard deviation.

The magnitude Bode plot for the 16-hour samples in Figure 29 is also similar in shape to the TSA-only plot. The average phase from 1 Hz to 100 Hz was -66.4 ± 2.6˚. After the corner frequency, the phase increases until eventually settling at 0˚, confirming a purely resistive element at higher frequencies.

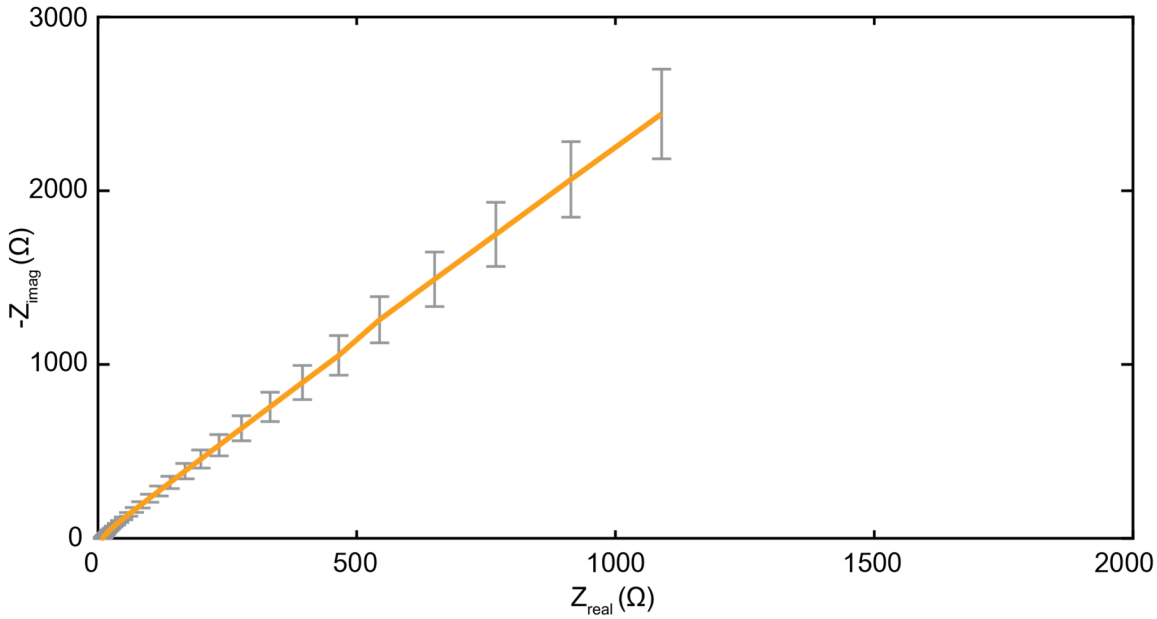

Figure 30. Nyquist plot depicting the real and imaginary impedance of *S. epidermidis* biofilm incubated for 16 hours across a range of frequencies using the two-electrode EIS setup. Mean ± 1 standard deviation, n = 3 plates measured each 3 times for a total of 9 measurements. The data is reported as the average of these 9 measurements with the associated standard deviation.

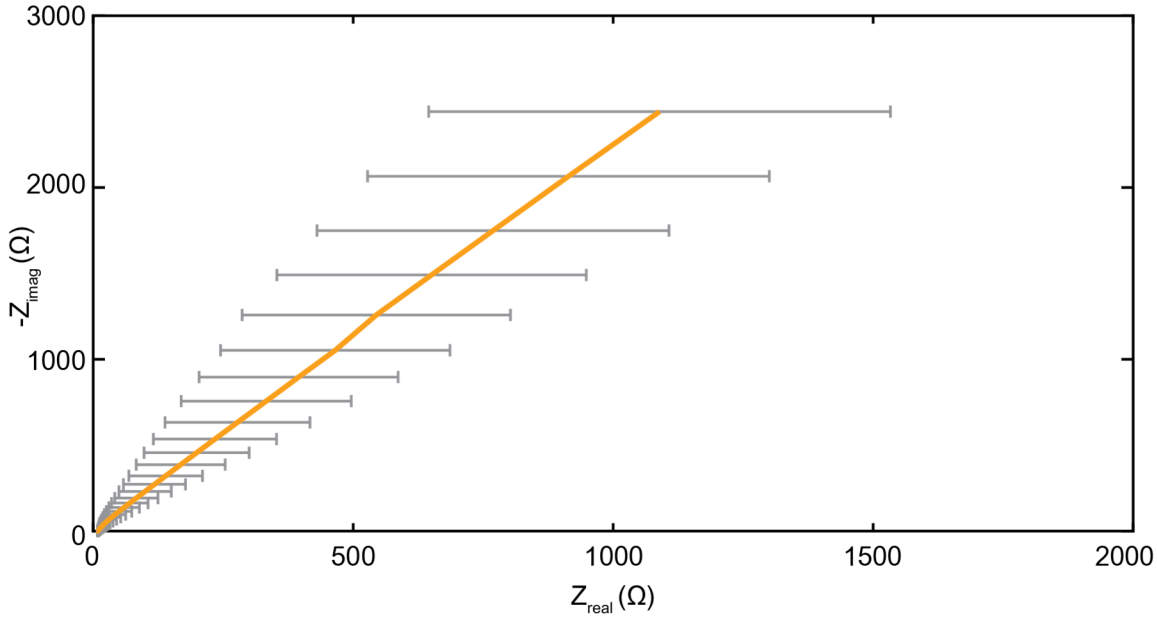

Figure 31. Nyquist plot depicting the real and imaginary impedance of *S. epidermidis* biofilm incubated for 16 hours across a range of frequencies using the two-electrode EIS setup. Mean ± 1 standard deviation, n = 3 plates measured each 3 times for a total of 9 measurements. The data is reported as the average of these 9 measurements with the associated standard deviation.

The Nyquist plots for the 16-hour biofilms in Figures 30 and 31 show the smallest standard deviation out of all previous samples in both the Z_{imag} and Z_{real} directions. The final impedance magnitude is located on the Z_{real} axis at 8.9 ± 1.2 **Ω**, corresponding to what was calculated from the magnitude Bode plot.

3.3.4 24 hours of biofilm growth

Figures 32-35 provide the Bode and Nyquist plots for the average of all 24-hour biofilm samples. The averaged plots from each sample are provided in Appendix C.6.

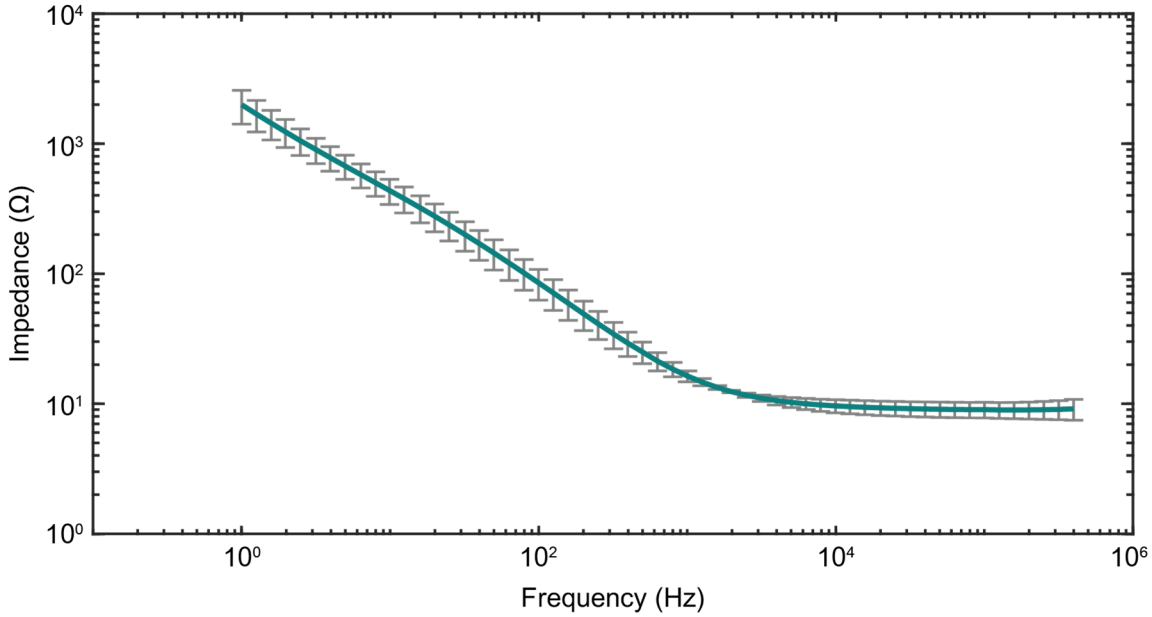

Figure 32. Bode plot depicting the impedance magnitude of *S. epidermidis* biofilm incubated for 24 hours across a range of frequencies using the two-electrode EIS setup. Mean ± 1 standard deviation, n = 3 plates measured each 3 times for a total of 9 measurements. The data is reported as the average of these 9 measurements with the associated standard deviation.

The magnitude Bode plot for the 24-hour biofilm samples has a similar shape to the other samples measured on the two-electrode device. The corner frequency for these samples was calculated to be 2849.6 ± 1497.7 Hz. The frequency-invariant impedance magnitude was measured as 9.1 ± 1.7 **Ω**.

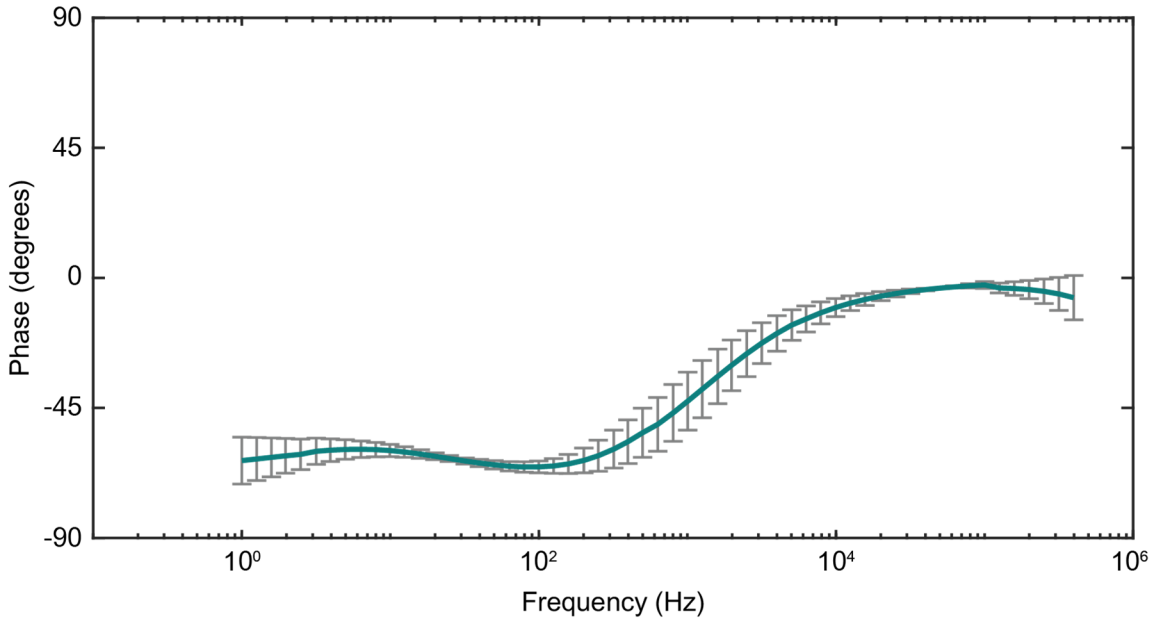

Figure 33. Bode plot depicting the impedance phase of *S. epidermidis* biofilm incubated for 24 hours across a range of frequencies using the two-electrode EIS setup. Mean ± 1 standard deviation, n = 3 plates measured each 3 times for a total of 9 measurements. The data is reported as the average of these 9 measurements with the associated standard deviation.

The impedance Bode plot for 24-hour biofilms in Figure 33 has some similar traits to that of the 8-hour biofilm. One notable similarity is that they are both not perfect CPEs. While they are both on the capacitive side of the -45-degree phase, the 8-hour biofilm fluctuates with a concave-up shape while the 24-hour biofilm fluctuates with a concave-down shape. The average value of the phase from 1 Hz to 100 Hz was -62.0 ± 3.2˚.

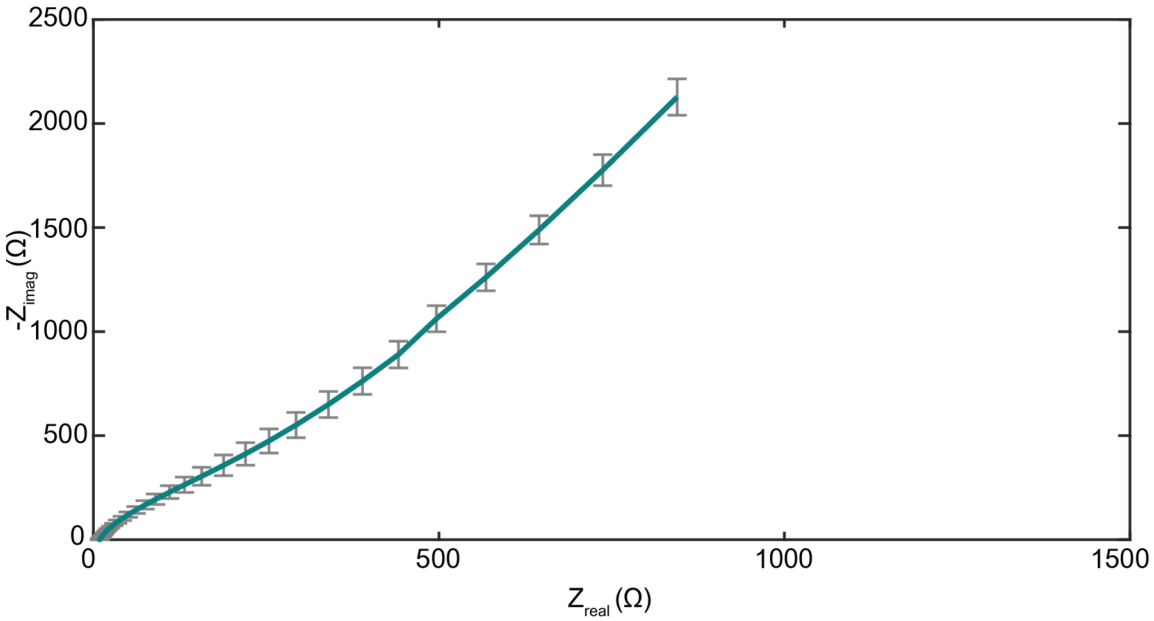

Figure 34. Nyquist plot depicting the real and imaginary impedance of *S. epidermidis* biofilm incubated for 24 hours across a range of frequencies using the two-electrode EIS setup. Mean ± 1 standard deviation, n = 3 plates measured each 3 times for a total of 9 measurements. The data is reported as the average of these 9 measurements with the associated standard deviation.

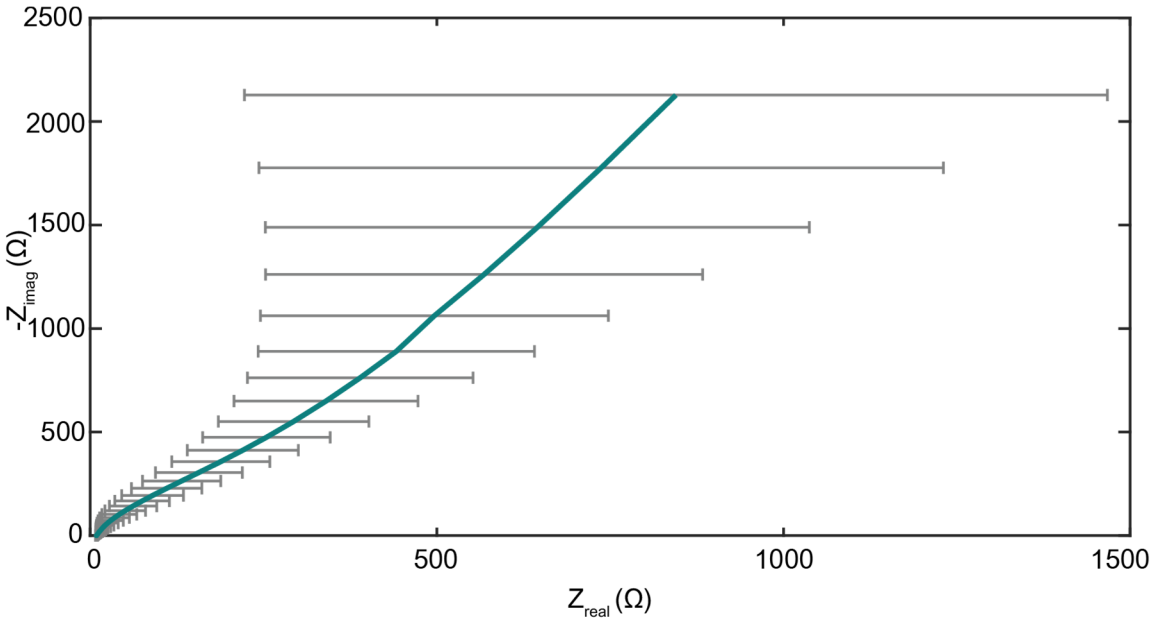

Figure 35. Nyquist plot depicting the real and imaginary impedance of *S. epidermidis* biofilm incubated for 24 hours across a range of frequencies using the two-electrode EIS setup. Mean ± 1 standard deviation, n = 3 plates measured each 3 times for a total of 9 measurements. The data is reported as the average of these 9 measurements with the associated standard deviation.

The Nyquist plots for the 24-hour biofilms in Figures 34 and 35 show a small standard deviation for the Z_{imag} axis but one of the largest standard deviations for the Z_{real} axis. The frequency-invariant impedance magnitude can be found at the intersection with the Z_{real} axis. The large standard deviation for the Z_{real} values as opposed to the Z_{imag} values indicates that the imaginary, or reactive, impedance component was very consistent across samples while the resistive component was more variable. However, all three samples still followed the same trend and showed a CPE with a more capacitive than resistive electrochemical response.

3.4 Comparison of all two-electrode experiments

The previous subsections described each plot individually with discussion of the standard deviation and important values found from each data set, which are tabulated in Table 5. To further illustrate the frequency-invariant magnitude across the two-electrode experiments, Figure 36 is provided with results from t-tests across all 10 combinations of data sets. The following section combines the magnitude Bode plots, the phase Bode plots, and the Nyquist plots into three overall plots. The standard deviation error bars are excluded for clarity. In addition to the biofilm data sets, the TSA-only data set that was measured using the two-electrode device is also included in each combined graph. Figure 37 shows the magnitude Bode plots, Figure 38 shows the phase Bode plots, and Figure 39 shows the Nyquist plots.

Table 5. Corner frequency, impedance, and average phase values calculated from data depicted in Figures 11, 20, 24, 28, and 32. Mean ± 1 Standard Deviation, n=3 for TSA Only, 0 hours, 16 hours, and 24 hours; n=4 for 8 hours. Final impedance magnitude refers to the frequency-independent impedance measured at 350 kHz.

Data Set	TSA Only	0 Hours	8 Hours	16 Hours	24 Hours
Corner Frequency	760.9 ± 144.3 Hz	1018.4 ± 803.5 Hz	1285.6 ± 247.3 Hz	1959.3 ± 1198.2 Hz	2849.6 ± 1497.7 Hz
Final Impedance Magnitude	24.2 ± 8.6 Ω	15.1 ± 7.4 Ω	9.9 ± 1.0 Ω	8.9 ± 1.2 Ω	9.1 ± 1.7 Ω
Average Phase from 1 - 100 Hz	-42.0 ± 4.6˚	-56.4 ± 9.8˚	-72.1 ± 1.7˚	-66.4 ± 2.6˚	-62.0 ± 3.2˚

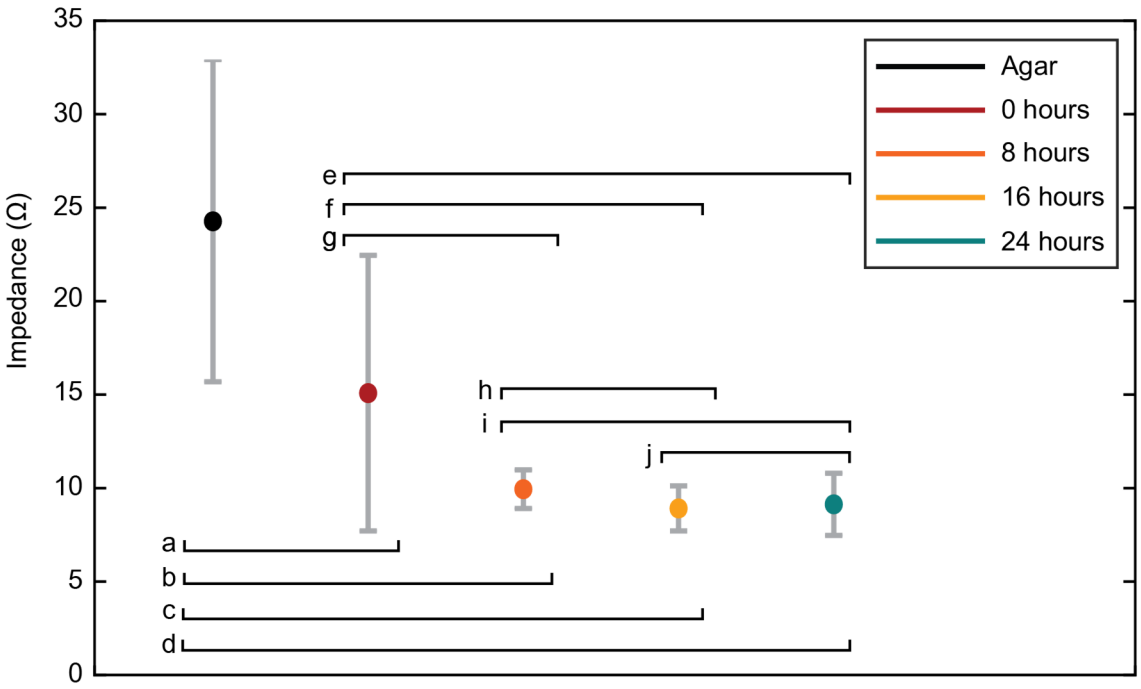

Figure 36. Average frequency-invariant impedance values measured at 350 kHz from each data set, plotted as mean ± 1 standard deviation, n=9 for all data sets to allow for statistical calculations (the 4th 8-hour measurement is excluded for this reason). A students-t test was

performed to calculate p-values for each comparison to determine the similarity between data sets. (a) TSA vs 0-hour, p = 0.29, (b) TSA vs 8-hour, p = 0.09, (c) TSA vs 16-hour, p = 0.11, (d) TSA vs 24-hour, p = 0.07, (e) 0-hour vs 8-hour, p = 0.40, (f) 0-hour vs 16-hour, p = 0.30, (g) 0-hour vs 24-hour, p = 0.35, (h) 8-hour vs 16-hour, p = 0.46, (i) 8-hour vs 24-hour, p = 0.18, (j) 16-hr vs 24-hr, p = 0.90.

The statistical analysis described in Figure 36 illustrates that the frequency-invariant impedance at 8-hours, 16-hours, and 24-hours have a notable amount of overlap, but also have a much smaller standard deviation as compared to the TSA-only and 0-hour data sets.

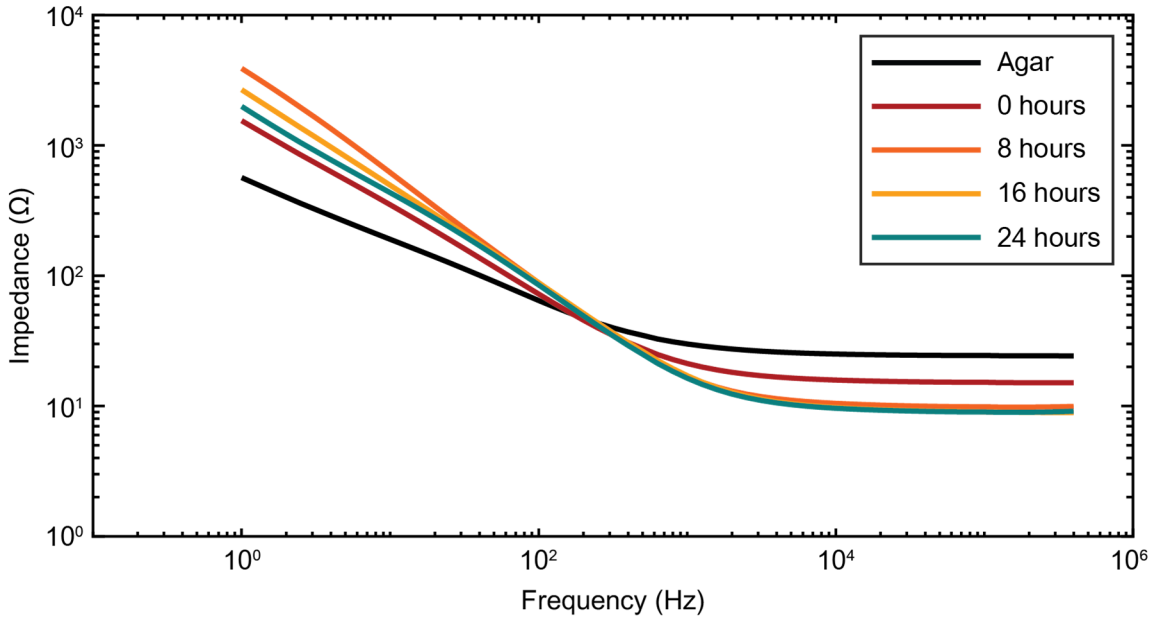

Figure 37. Bode plot depicting the impedance magnitudes of TSA and *S. epidermidis* biofilms incubated for 0, 8, 16, and 24 hours across a range of frequencies using the two-electrode EIS setup.

In Figure 37, the combined magnitude Bode plots allow us to see similarities across data sets. The frequency-invariant impedance magnitude of the TSA-only measurements was higher than that of all data sets including bacteria at 24.2 ± 8.6 Ω. At lower frequencies, the impedance measurements of the biofilm samples overall were higher than that of the TSA-only samples. The 0-hour data was closest to the TSA-only data at these frequencies.

As growth duration increased to 8-hours, the impedance magnitude at lower frequencies increased greatly then began to decrease at 16-hours and 24-hours. At higher frequencies, a contrasting trend occurs. The TSA-only samples showed the highest impedance magnitude, then decreased with the 0-hour samples. The impedance magnitude for the 8-,16-, and 24-hour samples were all very similar, reaching between 8 and 10 Ω in the frequency-invariant range. Another detail to note is that all biofilm data sets have a corner frequency greater than that of the TSA-only samples. Since the corner frequency is the frequency at which the resistive and reactive components of the system are closest, this would suggest that the biofilm samples have a more reactive electrochemical response than the TSA-only samples.

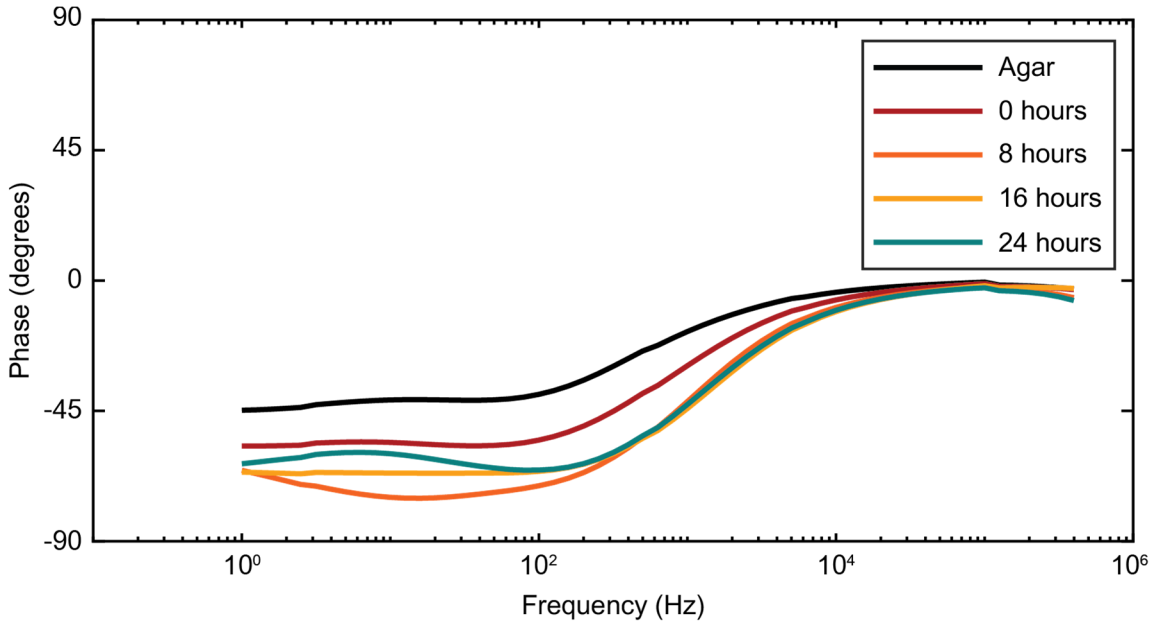

Figure 38. Bode plot depicting the impedance phases of TSA and *S. epidermidis* biofilms incubated for 0, 8, 16, and 24 hours across a range of frequencies using the two-electrode EIS setup.

The combined phase Bode plot in Figure 38 demonstrates the variation in phase for the CPE region of the plot. In contrast, the resistive region of the plot is very similar for all

samples, particularly near 100 kHz. The reason for the small dip in phase after 100 kHz is currently unknown but may be associated with an environmental factor as it is present on both TSA-only and biofilm plots. A pattern similar to the magnitude Bode plot is found at lower frequencies. Again, the phase of the TSA-only samples is distinct from all bacteria samples, and the 0-hour biofilm is closest in phase. With increasing growth duration, the 8-hour biofilm has the highest absolute value of phase, then 16-hour, and finally 24-hour.

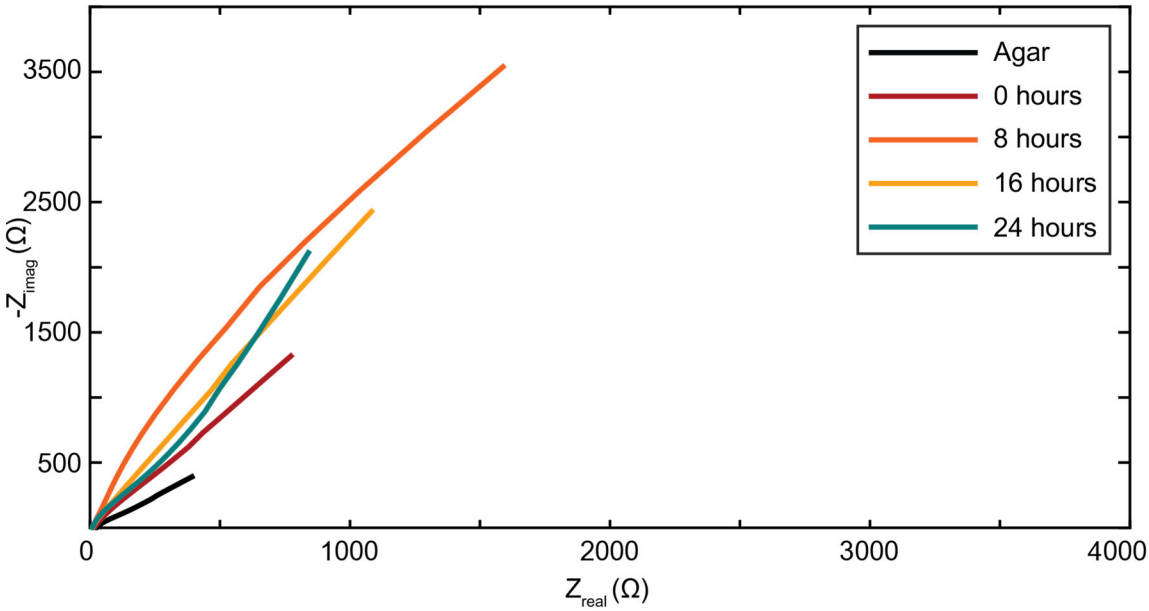

Figure 39. Nyquist plot depicting the real and imaginary impedances of TSA and *S. epidermidis* biofilms incubated for 0, 8, 16, and 24 hours across a range of frequencies using the two-electrode EIS setup.

The combined Nyquist plot in Figure 39 provides a clearer comparison of the relationships between biofilm growth duration and impedance. All biofilm samples had a phase angle of greater magnitude and a greater overall impedance than the TSA-only samples. The presence of bacteria in the 0-hour samples increased the impedance and absolute value of phase angle. With increased growth duration, the 8-hour biofilm showed

the greatest impedance and absolute value of phase angle which decreased with the 16-hour and 24-hours samples.

Of the previous publications that were reviewed in this thesis on biofilm EIS, only three provided Nyquist plots that followed the impedance of their respective biofilm over a certain growth period. Bharatula et. al[23] found that the impedance and absolute value of phase angle decreased over the duration of the biofilm's growth. The results reported by Bharatula et al visually agree with the trends found from the 8-hour, 16-hour, and 24-hours samples reported here. Additionally, the biofilm used in the work by Bharatula et. al was comprised *P. aeruginosa* which is both from a different bacteria family and is Gram-negative instead of Gram-positive.

The Nyquist plots published by Romero et. al[24] also show a decrease in the absolute value of phase angle and impedance over time, and their EIS measurements were taken at 1 hour, 6 hours, 13.5 hours, and 18.3 hours. However, since they did not report what specific combination of ureolytic bacteria species was used for their experiments, it is not simple to make a comparison. In addition, this publication also found that the biofilm's impedance response became more semi-circular, or kinetic, in shape over time rather only diffusional.

Ben-Yoav et. al[20] published Nyquist plots with a different trends. Rather than decreasing phase angle and impedance over time, the absolute value of phase angle increased over time while the impedance was similar across the entire growth duration. This publication also measured at the most time points – a total of six from 12 hours to 91 hours. The biofilm studied in this publication was *E. coli*.

Across these publications, we find that the results from Bharatula et. al agree closest to our results, because we also found a decrease in the absolute value of phase angle and impedance magnitude across 8-, 16-, and 24-hour measurements. The previous work by Bharatula et. al also exhibited diffusion regions shown in the Nyquist plots across all time points. While the other two publications did not align as closely, this can be expected as each species of bacteria behaves differently. The environment in which the biofilm is studied can also impact the results. In Table 6, the differences in biofilm growth procedures between these publications and our results are provided.

Table 6. Biofilm growth conditions across three publications and our experiments.

Authors	Bacteria Species	Growth Media	Gel or Liquid
Bharatula et. al[23]	*P. aeruginosa*	ABTG Media	Liquid Media
Romero et. al[24]	Combination of ureolytic bacteria	Luria-Bertani Media	Liquid Media
Ben-Yoav et. al[20]	*E. coli*	Luria-Bertani Media	Liquid Media
Our Experiments	*S. epidermidis*	Tryptic Soy Agar	Gel Media

After analyzing the results of this thesis, we were able to produce an equivalent circuit to represent the two-electrode systems, as shown in Figure 40. The interface of the silver electrodes and TSA is modeled as a CPE. This is similar to how the interface between electrode and media was represented in previous publications[19, 20, 25]. The resistor represents the combination of TSA and biofilm. The TSA on its own had a set resistance, and adding biofilm reduced the total resistance. A series configuration was chosen because the shape of the Bode plots closely matches that of a resistor and capacitor in series. The

only major difference is that the phase of the experimental data was not -90˚ at lower frequencies because it is a CPE and not a strictly capacitive element.

While there are still more complex equivalent circuits that would be slightly more accurate, the key aspects of the results are captured in a simple and straightforward way.

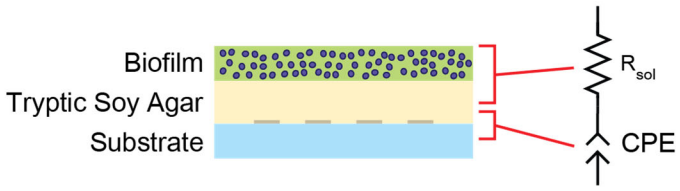

Figure 40. A diagram of the proposed equivalent circuit for the two-electrode EIS device. R_{sol} is the resistance of the solution, which is either TSA alone or TSA and biofilm. CPE is the constant phase element at the double-layer boundary of the silver electrodes and the TSA.

Chapter 4. Summary, Conclusions, and Future Work

4.1 Summary of Results and Conclusions

Past research in our group has primarily focused on the healing of chronic wounds[12, 13], but it is equally important to understand the method by which a biofilm infection occurs. A deeper understanding of the communication and growth process of biofilms provides valuable information for the prevention of infections entirely. In this thesis, we designed and fabricated a device for performing EIS on biofilms for the purpose of gaining a better understanding of their growth cycle and communication patterns. The device was unique in that the fabrication method provided a much larger electrode surface area than previous EIS configurations[19-25], allowing the device to take measurements across a larger media volume. Some major challenges occurred even before most of the data collection took place. Determining the most consistent photolithography process and finalizing the biofilm growth procedure were the most time-consuming challenges.

We found that the interdigitated two-electrode design was best for collecting and analyzing both tryptic soy agar (TSA) and biofilm data as it aligned with the results found in prior publications, while the four-electrode design produced much more complicated results. An equivalent circuit was proposed to provide a physical interpretation of the two-electrode devices. The circuit consisted of a constant phase element (CPE) in series with a resistor. Both devices were able to collect repeatable results from the TSA experiments. The two-electrode device was selected as the design which was simpler to interpret and was also capable of producing repeatable results at 0, 8, 16, and 24 hours of biofilm growth.

Experiments performed only on TSA found that at lower frequencies, TSA behaves as a Warburg element, or CPE with a constant phase of -45°[111]. Experiments including biofilms showed that they introduced a more capacitive electrochemical response. The impedance calculated in all biofilm experiments was greater than the impedance found in TSA-only experiments.

From the trends shown in Figures 37, 38, and 39, the presence of *S. epidermidis* causes an increase in the absolute value of phase, and an increase in impedance for low frequencies but a decrease in impedance at high frequencies. After 8 hours of growth the absolute value of phase and impedance magnitude was much higher than that of either the 0-hour or TSA-only samples. This means that the presence of bacteria contributes a charge storage ability, with the 8-hour biofilm showing the greatest charge storage capacity. Between the 0-hour and 8-hour samples, the biofilm would be progressing from the reversible attachment stage (at 0 hours) to further on in the biofilm growth cycle, such as irreversible attachment, maturation, or dispersion. Since a true biofilm with EPS has not yet formed during the 0-hour measurements, the 8-hour measurements can be described as our first true "biofilm" measurements. Following the 8-hour samples, we found that the magnitude of impedance and absolute value of phase decreased with the 16-hours and 24-hour measurements, meaning that after an initial peak in charge storage capacity, the biofilm continues to decrease in charge storage capacity.

4.2 Proposed Future Work

For this thesis, the two-electrode EIS device was only used to study *S. epidermidis* biofilm, while one of the most studied biofilms was *P. aeruginosa* [19, 21, 23]. Exploring other biofilms would allow for a more direct comparison with previous work. In addition, studying more biofilm species may provide insight into whether certain traits affect the electrochemical properties of the biofilm, such as the family of bacteria or whether the species is Gram-positive or Gram-negative.

Previous work also showed that two-electrode measurements were common for biofilm research, but not often used when the growth or adhesion of the biofilm were the key result. Two-electrode experiments were more often used in microbial fuel cell studies[98-101], while fewer publications used a two-electrode EIS configuration for microbially-influenced corrosion[62] or biofilm characterization[25]. Because of this, designing a three-electrode configuration would be an interesting next step in this project. A three-electrode device would allow for a better comparison to previous works.

One of the most challenging aspects of this thesis was initially attempting to grow biofilm directly in the devices. While moving a piece of agar into the device after the biofilm has grown still provides repeatable results, the initial intention of these devices was to allow biofilms to be grown directly inside the device with no need for additional maneuvering. The compact size of the device may have been an issue, so a potential solution would be to increase the scale of the device to allow the bacteria to be spread more easily and produce an even biofilm layer. A larger surface area may also help with

distribution of oxygen in the incubator, which was an issue due to the height of the walls on the PDMS wells.

Finally, collecting more data from the existing two-electrode device design, whether at the same time points in the biofilm growth duration or different ones, will allow for a clearer understanding of trends in the electrochemical properties of *S. epidermidis*. For example, collecting EIS data at 4-hour, 12-hour, and 20-hour time points would allow us more insight into the stages of biofilm growth and the time at which the peak charge storage capacity is reached. Collecting EIS data after 24 hours of growth would allow for a better comparison with previous works, many of which studied biofilms that were 24-hours old at a minimum and would also allow us to identify if the phase and impedance eventually reaches a steady state. Since the majority of the data for each time point was recorded on the same day, it would be interesting to see if differences arise when every biofilm is not grown from the same overnight culture.

This device has been proven to produce replicable results, but there is still a great deal of work to be done by future researchers in order to understand the patterns behind biofilm communication at the electrochemical level.

Bibliography

1. Malone, M.; Bjarnsholt, T.; McBain, A. J.; James, G. A.; Stoodley, P.; Leaper, D.; Tachi, M.; Schultz, G.; Swanson, T.; Wolcott, R. D., The prevalence of biofilms in chronic wounds: a systematic review and meta-analysis of published data. *Journal of Wound Care* **2017,** *26* (1), 20-25.
2. Jamal, M.; Ahmad, W.; Andleeb, S.; Jalil, F.; Imran, M.; Nawaz, M. A.; Hussain, T.; Ali, M.; Rafiq, M.; Kamil, M. A., Bacterial biofilm and associated infections. *Journal of the chinese medical association* **2018,** *81* (1), 7-11.
3. Veerachamy, S.; Yarlagadda, T.; Manivasagam, G.; Yarlagadda, P. K., Bacterial adherence and biofilm formation on medical implants: a review. *Proceedings of the Institution of Mechanical Engineers, Part H: Journal of Engineering in Medicine* **2014,** *228* (10), 1083-1099.
4. Rimondini, L.; Cochis, A.; Varoni, E.; Azzimonti, B.; Carrassi, A., Biofilm formation on implants and prosthetic dental materials. **2015**.
5. Sun, H. M.; Pulakat, L.; Anderson, D. W., Challenges and New Therapeutic Approaches in the Management of Chronic Wounds. *Current Drug Targets* **2020,** *21* (12), 1264-1275.
6. Sen, C. K.; Gordillo, G. M.; Roy, S.; Kirsner, R.; Lambert, L.; Hunt, T. K.; Gottrup, F.; Gurtner, G. C.; Longaker, M. T., Human skin wounds: a major and snowballing threat to public health and the economy. *Wound repair and regeneration* **2009,** *17* (6), 763-771.
7. Sridhar, S.; Wang, F.; Wilson, T. G.; Palmer, K.; Valderrama, P.; Rodrigues, D. C., The role of bacterial biofilm and mechanical forces in modulating dental implant failures. *Journal of the Mechanical Behavior of Biomedical Materials* **2019,** *92*, 118-127.
8. Bürgers, R.; Gerlach, T.; Hahnel, S.; Schwarz, F.; Handel, G.; Gosau, M., In vivo and in vitro biofilm formation on two different titanium implant surfaces. *Clinical Oral Implants Research* **2010,** *21* (2), 156-164.
9. Busscher, H.; Rinastiti, M.; Siswomihardjo, W.; Van der Mei, H., Biofilm formation on dental restorative and implant materials. *Journal of Dental Research* **2010,** *89* (7), 657-665.
10. Gbejuade, H. O.; Lovering, A. M.; Webb, J. C., The role of microbial biofilms in prosthetic joint infections. *Acta Orthop* **2015,** *86* (2), 147-158.
11. Zimmerli, W.; Trampuz, A.; Ochsner, P. E., Prosthetic-joint infections. *New England Journal of Medicine* **2004,** *351* (16), 1645-1654.
12. Heald, R.; Bennett, M.; Subramaniam, V. V.; Dusane, D.; Lochab, V.; Sundaram, P. M.; Salyer, S.; West, J.; Stoodley, P.; Prakash, S., Printed electroceutical dressings for the inhibition of biofilms and treatment of chronic wounds. *Journal of Microelectromechanical Systems* **2020,** *29* (5), 918-923.
13. Heald, R.; Salyer, S.; Ham, K.; Wilgus, T. A.; Subramaniam, V. V.; Prakash, S., Electroceutical treatment of infected chronic wounds in a dog and a cat. *Veterinary Surgery* **2022**.

14. Manna, S.; Ghanty, C.; Baindara, P.; Barik, T. K.; Mandal, S. M., Electrochemical communication in biofilm of bacterial community. *Journal of Basic Microbiology* **2020,** *60* (10), 819-827.
15. Wicken, A. J., Bacterial Cell Walls and Surfaces. In *Bacterial Adhesion: Mechanisms and Physiological Significance*, Savage, D. C.; Fletcher, M., Eds. Springer US: Boston, MA, 1985; pp 45-70.
16. Hall-Stoodley, L.; Stoodley, P., Evolving concepts in biofilm infections. *Cellular Microbiology* **2009,** *11* (7), 1034-1043.
17. Liu, J.; Martinez-Corral, R.; Prindle, A.; Lee, D.-y. D.; Larkin, J.; Gabalda-Sagarra, M.; Garcia-Ojalvo, J.; Süel, G. M., Coupling between distant biofilms and emergence of nutrient time-sharing. *Science* **2017,** *356* (6338), 638-642.
18. Poma, N.; Vivaldi, F.; Bonini, A.; Salvo, P.; Kirchhain, A.; Ates, Z.; Melai, B.; Bottai, D.; Tavanti, A.; Di Francesco, F., Microbial biofilm monitoring by electrochemical transduction methods. *TrAC Trends in Analytical Chemistry* **2021,** *134*, 116134.
19. Kim, T.; Kang, J.; Lee, J. H.; Yoon, J., Influence of attached bacteria and biofilm on double-layer capacitance during biofilm monitoring by electrochemical impedance spectroscopy. *Water Research* **2011,** *45* (15), 4615-4622.
20. Ben-Yoav, H.; Freeman, A.; Sternheim, M.; Shacham-Diamand, Y., An electrochemical impedance model for integrated bacterial biofilms. *Electrochimica Acta* **2011,** *56* (23), 7780-7786.
21. Fraiwan, A.; Choi, S.; Ieee In *A Biomicrosystem for Simultaneous Optical and Electrochemical Monitoring of Electroactive Microbial Biofilm*, 2015 Ieee Sensors, Busan, SOUTH KOREA, Nov 01-04; Busan, SOUTH KOREA, 2015; pp 197-200.
22. Dheilly, A.; Linossier, I.; Darchen, A.; Hadjiev, D.; Corbel, C.; Alonso, V., Monitoring of microbial adhesion and biofilm growth using electrochemical impedancemetry. *Applied Microbiology and Biotechnology* **2008,** *79* (1), 157-164.
23. Bharatula, L. D.; Marsili, E.; Kwan, J. J., Impedimetric detection of Pseudomonas aeruginosa attachment on flexible ITO-coated polyethylene terephthalate substrates. *Electrochimica Acta* **2020,** *332*.
24. Romero, M. C.; Ramos, G.; Gonzalez, I.; Ramirez, F., A Novel Method to Reveal a Ureolytic Biofilm Attachment and In Situ Growth Monitoring by Electrochemical Impedance Spectroscopy. *Applied Biochemistry and Biotechnology* **2021,** *193* (5), 1379-1396.
25. Ward, A. C.; Hannah, A. J.; Kendrick, S. L.; Tucker, N. P.; MacGregor, G.; Connolly, P., Identification and characterisation of Staphylococcus aureus on low cost screen printed carbon electrodes using impedance spectroscopy. *Biosensors & Bioelectronics* **2018,** *110*, 65-70.
26. Franklin, M. J.; Nivens, D. E.; Guckert, J. B.; White, D. C., EFFECT OF ELECTROCHEMICAL IMPEDANCE SPECTROSCOPY ON MICROBIAL BIOFILM CELL NUMBERS, VIABILITY, AND ACTIVITY. *Corrosion* **1991,** *47* (7), 519-522.
27. Miller, M. B.; Bassler, B. L., Quorum sensing in bacteria. *Annual Reviews in Microbiology* **2001,** *55* (1), 165-199.

28. Prindle, A.; Liu, J.; Asally, M.; Ly, S.; Garcia-Ojalvo, J.; Süel, G. M., Ion channels enable electrical communication in bacterial communities. *Nature* **2015,** *527* (7576), 59-63.
29. Dusane, D. H.; Lochab, V.; Jones, T.; Peters, C. W.; Sindeldecker, D.; Das, A.; Roy, S.; Sen, C. K.; Subramaniam, V. V.; Wozniak, D. J., Electroceutical treatment of Pseudomonas aeruginosa biofilms. *Scientific reports* **2019,** *9* (1), 1-13.
30. Lochab, V.; Jones, T. H.; Dusane, D. H.; Peters, C. W.; Stoodley, P.; Wozniak, D. J.; Subramaniam, V. V.; Prakash, S., Ultrastructure imaging of Pseudomonas aeruginosa lawn biofilms and eradication of the tobramycin-resistant variants under in vitro electroceutical treatment. *Scientific reports* **2020,** *10* (1), 1-12.
31. Garrett, T. R.; Bhakoo, M.; Zhang, Z., Bacterial adhesion and biofilms on surfaces. *Progress in Natural Science* **2008,** *18* (9), 1049-1056.
32. Toda, Y.; Moro, I.; Koga, T.; Asakawa, H.; Hamada, S., Ultrastructure of extracellular polysaccharides produced by serotype c Streptococcus mutans. *Journal of Dental Research* **1987,** *66* (8), 1364-1369.
33. Branda, S. S.; Vik, A.; Friedman, L.; Kolter, R., Biofilms: the matrix revisited. *Trends in Microbiology* **2005,** *13* (1), 20-26.
34. Hall-Stoodley, L.; Costerton, J. W.; Stoodley, P., Bacterial biofilms: From the natural environment to infectious diseases. *Nature Reviews Microbiology* **2004,** *2* (2), 95-108.
35. Boyd, J.; Korotkova, N.; Grady, M., Adhesion of Biofilms on Titanium Measured by Laser-Induced Spallation. *Experimental Mechanics* **2018**, 1-10.
36. Lopez, D.; Vlamakis, H.; Kolter, R., Biofilms. *Cold Spring Harbor Perspectives in Biology* **2010,** *2* (7).
37. Hoiby, N.; Ciofu, O.; Johansen, H. K.; Song, Z. J.; Moser, C.; Jensen, P. O.; Molin, S.; Givskov, M.; Tolker-Nielsen, T.; Bjarnsholt, T., The clinical impact of bacterial biofilms. *International Journal of Oral Science* **2011,** *3* (2), 55-65.
38. Hernandez-Jimenez, E.; del Campo, R.; Toledano, V.; Vallejo-Cremades, M. T.; Munoz, A.; Largo, C.; Arnalich, F.; Garcia-Rio, F.; Cubillos-Zapata, C.; Lopez-Collazo, E., Biofilm vs. planktonic bacterial mode of growth: Which do human macrophages prefer? *Biochemical and Biophysical Research Communications* **2013,** *441* (4), 947-952.
39. Cross, S. E.; Kreth, J.; Zhu, L.; Sullivan, R.; Shi, W.; Qi, F.; Gimzewski, J. K., Nanomechanical properties of glucans and associated cell-surface adhesion of Streptococcus mutans probed by atomic force microscopy under in situ conditions. *Microbiology* **2007,** *153* (9), 3124-3132.
40. Dunne, W. M., Bacterial Adhesion: Seen Any Good Biofilms Lately? *Clinical Microbiology Reviews* **2002,** *15* (2), 155-166.
41. Waters, M. S.; Kundu, S.; Lin, N. J.; Lin-Gibson, S., Microstructure and Mechanical Properties of In Situ Streptococcus mutans Biofilms. *ACS Applied Materials & Interfaces* **2014,** *6* (1), 327-332.
42. Mikkelsen, H.; Duck, Z.; Lilley, K.; Welch, M., Interrelationships between colonies, biofilms, and planktonic cells of Pseudomonas aeruginosa. *Journal of bacteriology* **2007,** *189* (6), 2411-2416.

43. Maunders, E.; Welch, M., Matrix exopolysaccharides; the sticky side of biofilm formation. *Fems Microbiology Letters* **2017,** *364* (13).
44. Muhammad, M. H.; Idris, A. L.; Fan, X.; Guo, Y. C.; Yu, Y. Y.; Jin, X.; Qiu, J. Z.; Guan, X.; Huang, T. P., Beyond Risk: Bacterial Biofilms and Their Regulating Approaches. *Frontiers in Microbiology* **2020,** *11*.
45. Bhatia, R.; Gulati, D.; Sethi, G., Biofilms and nanoparticles: applications in agriculture. *Folia Microbiologica* **2021**, 1-12.
46. Pandit, A.; Adholeya, A.; Cahill, D.; Brau, L.; Kochar, M., Microbial biofilms in nature: unlocking their potential for agricultural applications. *Journal of applied microbiology* **2020,** *129* (2), 199-211.
47. Qureshi, N., Beneficial biofilms: wastewater and other industrial applications. In *Biofilms in the Food and Beverage Industries*, Elsevier: 2009; pp 474-498.
48. Arnold, J. W., Development of bacterial biofilms during poultry processing. *Poultry and Avian Biology Reviews* **1998,** *9* (1), 1-9.
49. Lapointe, C.; Deschenes, L.; Ells, T. C.; Bisaillon, Y.; Savard, T., Interactions between spoilage bacteria in tri-species biofilms developed under simulated meat processing conditions. *Food Microbiology* **2019,** *82*, 515-522.
50. Herzberg, M.; Berglin, M.; Eliahu, S.; Bodin, L.; Agrenius, K.; Zlotkin, A.; Svenson, J., Efficient Prevention of Marine Biofilm Formation Employing a Surface-Grafted Repellent Marine Peptide. *Acs Applied Bio Materials* **2021,** *4* (4), 3360-3373.
51. Brant, K. M.; Gilg, M. R., Testing the relative effectiveness of traditional and non-traditional antifouling substrates on barnacle and macroalgae settlement. *Marine Biology Research* **2014,** *10* (10), 1027-1032.
52. Hnatiuc, B.; Sabau, A.; Ghita, S.; Hnatiuc, M.; Dumitrache, C. L.; Pellerin, S. In *Influence of GlidArc treatment on layers formation of biofouling*, 7th International Conference on Advanced Topics in Optoelectronics, Microelectronics, and Nanotechnologies (ATOM-N), Constanta, ROMANIA, Aug 21-24; Constanta, ROMANIA, 2014.
53. Fux, C. A.; Quigley, M.; Worel, A.; Post, C.; Zimmerli, S.; Ehrlich, G.; Veeh, R. H., Biofilm-related infections of cerebrospinal fluid shunts. *Clinical Microbiology and Infection* **2006,** *12* (4), 331-337.
54. Hall-Stoodley, L.; Costerton, J. W.; Stoodley, P., Bacterial biofilms: from the natural environment to infectious diseases. *Nature Reviews Microbiology* **2004,** *2* (2), 95.
55. Adair, C.; Gorman, S.; Feron, B.; Byers, L.; Jones, D.; Goldsmith, C.; Moore, J.; Kerr, J.; Curran, M.; Hogg, G., Implications of endotracheal tube biofilm for ventilator-associated pneumonia. *Intensive Care Medicine* **1999,** *25* (10), 1072-1076.
56. Wu, H.; Moser, C.; Wang, H.-Z.; Høiby, N.; Song, Z.-J., Strategies for combating bacterial biofilm infections. *International Journal of Oral Science* **2015,** *7* (1), 1.
57. Kallick, E.; Nistico, L.; Longwell, M.; Byers, B.; Cartieri, F.; Kreft, R.; Edington, H., Resistance of Synthetic and Biologic Surgical Meshes to Methicillin-Resistant Staphylococcus aureus Biofilm: An In Vitro Investigation. *International Journal of Biomaterials* **2019,** *2019*.

58. Muro-Fraguas, I.; Sainz-Garcia, A.; Lopez, M.; Rojo-Bezares, B.; Mugica-Vidal, R.; Sainz-Garcia, E.; Toledano, P.; Saenz, Y.; Gonzalez-Marcos, A.; Alba-Elias, F., Antibiofilm coatings through atmospheric pressure plasma for 3D printed surgical instruments. *Surface & Coatings Technology* **2020,** *399*.
59. Cope, J. R.; Collier, S. A.; Nethercut, H.; Jones, J. M.; Yates, K.; Yoder, J. S., Risk behaviors for contact lens–related eye infections among adults and adolescents—United States, 2016. *MMWR. Morbidity and Mortality Weekly Report* **2017,** *66* (32), 841.
60. McLaughlin-Borlace, L.; Stapleton, F.; Matheson, M.; Dart, J., Bacterial biofilm on contact lenses and lens storage cases in wearers with microbial keratitis. *Journal of Applied Microbiology* **1998,** *84* (5), 827-838.
61. Ball, A. S.; Chaparian, R. R.; van Kessel, J. C., Quorum sensing gene regulation by LuxR/HapR master regulators in vibrios. *Journal of bacteriology* **2017,** *199* (19), e00105-17.
62. Jia, R.; Yang, D. Q.; Xu, D. K.; Gu, T. Y., Electron transfer mediators accelerated the microbiologically influence corrosion against carbon steel by nitrate reducing Pseudomonas aeruginosa biofilm. *Bioelectrochemistry* **2017,** *118*, 38-46.
63. Haque, S.; Yadav, D. K.; Bisht, S. C.; Yadav, N.; Singh, V.; Dubey, K. K.; Jawed, A.; Wahid, M.; Dar, S. A., Quorum sensing pathways in Gram-positive and-negative bacteria: potential of their interruption in abating drug resistance. *Journal of Chemotherapy* **2019,** *31* (4), 161-187.
64. Abisado, R. G.; Benomar, S.; Klaus, J. R.; Dandekar, A. A.; Chandler, J. R., Bacterial quorum sensing and microbial community interactions. *MBio* **2018,** *9* (3), e02331-17.
65. Hardman, A. M.; Stewart, G. S.; Williams, P., Quorum sensing and the cell-cell communication dependent regulation of gene expression in pathogenic and non-pathogenic bacteria. *Antonie Van Leeuwenhoek* **1998,** *74* (4), 199-210.
66. Banerji, R.; Kanojiya, P.; Saroj, S. D., Role of interspecies bacterial communication in the virulence of pathogenic bacteria. *Critical Reviews in Microbiology* **2020,** *46* (2), 136-146.
67. Li, Y.-H.; Tian, X., Quorum sensing and bacterial social interactions in biofilms. *Sensors* **2012,** *12* (3), 2519-2538.
68. Kong, K.-F.; Vuong, C.; Otto, M., Staphylococcus quorum sensing in biofilm formation and infection. *International journal of medical microbiology* **2006,** *296* (2-3), 133-139.
69. Olson, M. E.; Todd, D. A.; Schaeffer, C. R.; Paharik, A. E.; Van Dyke, M. J.; Büttner, H.; Dunman, P. M.; Rohde, H.; Cech, N. B.; Fey, P. D., Staphylococcus epidermidis agr quorum-sensing system: signal identification, cross talk, and importance in colonization. *Journal of bacteriology* **2014,** *196* (19), 3482-3493.
70. Verbeke, F.; De Craemer, S.; Debunne, N.; Janssens, Y.; Wynendaele, E.; Van de Wiele, C.; De Spiegeleer, B., Peptides as quorum sensing molecules: measurement techniques and obtained levels in vitro and in vivo. *Frontiers in neuroscience* **2017,** *11*, 183.
71. Ghosh, R.; Das, A.; Mallik, S., Inhibition of quorum sensing in Pseudomonas aeruginosa: a review. *Indian Journal of Pharmaceutical Sciences* **2019,** *81* (5), 797-806.

72. Lee, J.; Zhang, L., The hierarchy quorum sensing network in Pseudomonas aeruginosa. *Protein & cell* **2015,** *6* (1), 26-41.
73. Liu, J.; Prindle, A.; Humphries, J.; Gabalda-Sagarra, M.; Asally, M.; Lee, D.-y. D.; Ly, S.; Garcia-Ojalvo, J.; Süel, G. M., Metabolic co-dependence gives rise to collective oscillations within biofilms. *Nature* **2015,** *523* (7562), 550-554.
74. Jing, X.; Yang, Y.; Ai, Z.; Chen, S.; Zhou, S., Potassium channel blocker inhibits the formation and electroactivity of Geobacter biofilm. *Science of The Total Environment* **2020,** *705*, 135796.
75. Chen, G.-Q.; Cui, C.; Mayer, M. L.; Gouaux, E., Functional characterization of a potassium-selective prokaryotic glutamate receptor. *Nature* **1999,** *402* (6763), 817-821.
76. Ren, D.; Navarro, B.; Xu, H.; Yue, L.; Shi, Q.; Clapham, D. E., A prokaryotic voltage-gated sodium channel. *Science* **2001,** *294* (5550), 2372-2375.
77. Iyer, R.; Iverson, T. M.; Accardi, A.; Miller, C., A biological role for prokaryotic ClC chloride channels. *Nature* **2002,** *419* (6908), 715-718.
78. Choi, W.; Shin, H.-C.; Kim, J. M.; Choi, J.-Y.; Yoon, W.-S., Modeling and applications of electrochemical impedance spectroscopy (EIS) for lithium-ion batteries. *Journal of Electrochemical Science and Technology* **2020,** *11* (1), 1-13.
79. Noelle, R.; Beltrop, K.; Holtstiege, F.; Kasnatscheew, J.; Placke, T.; Winter, M., A reality check and tutorial on electrochemical characterization of battery cell materials: How to choose the appropriate cell setup. *Materials Today* **2020,** *32*, 131-146.
80. Middlemiss, L. A.; Rennie, A. J. R.; Sayers, R.; West, A. R., Characterisation of batteries by electrochemical impedance spectroscopy. *Energy Reports* **2020,** *6*, 232-241.
81. Zhang, X. H.; Zhang, X.; Sun, X. Z.; An, Y. B.; Song, S.; Li, C.; Wang, K.; Su, F. Y.; Chen, C. M.; Liu, F. Y.; Wu, Z. S.; Ma, Y. W., Electrochemical impedance spectroscopy study of lithium-ion capacitors: Modeling and capacity fading mechanism. *Journal of Power Sources* **2021,** *488*.
82. Lufrano, F.; Staiti, P.; Minutoli, M., Evaluation of nafion based double layer capacitors by electrochemical impedance spectroscopy. *Journal of Power Sources* **2003,** *124* (1), 314-320.
83. Sun, X. Z.; Huang, B.; Zhang, X.; Zhang, D. C.; Zhang, H. T.; Ma, Y. W., Experimental Investigation of Electrochemical Impedance Spectroscopy of Electrical Double Layer Capacitor. *Acta Physico-Chimica Sinica* **2014,** *30* (11), 2071-2076.
84. Asghari, S.; Mokmeli, A.; Samavati, M., Study of PEM fuel cell performance by electrochemical impedance spectroscopy. *International Journal of Hydrogen Energy* **2010,** *35* (17), 9283-9290.
85. Easton, E. B.; Pickup, P. G., An electrochemical impedance spectroscopy study of fuel cell electrodes. *Electrochimica Acta* **2005,** *50* (12), 2469-2474.
86. Kashyap, D.; Dwivedi, P. K.; Pandey, J. K.; Kim, Y. H.; Kim, G. M.; Sharma, A.; Goel, S., Application of electrochemical impedance spectroscopy in bio-fuel cell characterization: A review. *International Journal of Hydrogen Energy* **2014,** *39* (35), 20159-20170.
87. Turick, C. E.; Colon-Mercado, H.; Bagwell, C. E.; Greenway, S. D.; Amoroso, J. W., Non-contact electrochemical evaluation of biofilms. *Sn Applied Sciences* **2020,** *2* (3).

88. Randviir, E. P.; Banks, C. E., Electrochemical impedance spectroscopy: an overview of bioanalytical applications. *Analytical Methods* **2013,** *5* (5), 1098-1115.
89. Permeh, S.; Lau, K.; Duncan, M., Characterization of Biofilm Formation and Coating Degradation by Electrochemical Impedance Spectroscopy. *Coatings* **2019,** *9* (8).
90. Horowitz, P.; Hill, W.; Robinson, I., *The art of electronics*. Cambridge university press Cambridge: 1989; Vol. 2.
91. Chang, B.-Y.; Park, S.-M., Electrochemical impedance spectroscopy. *Annual Review of Analytical Chemistry* **2010,** *3*, 207-229.
92. Franklin, M. J.; Nivens, D. E.; Vass, A. A.; Mittelman, M. W.; Jack, R. F.; Dowling, N. J. E.; White, D. C., EFFECT OF CHLORINE AND CHLORINE BROMINE BIOCIDE TREATMENTS ON THE NUMBER AND ACTIVITY OF BIOFILM BACTERIA AND ON CARBON-STEEL CORROSION. *Corrosion* **1991,** *47* (2), 128-134.
93. Heyer, A.; D'Souza, F.; Morales, C. F. L.; Ferrari, G.; Mol, J. M. C.; de Wit, J. H. W., Ship ballast tanks a review from microbial corrosion and electrochemical point of view. *Ocean Engineering* **2013,** *70*, 188-200.
94. Li, S. M.; Zhang, Y. Y.; Liu, J. H.; Yu, M., INFLUENCE OF THIOBACILLUS FERROXIDANS BIOFILM ON THE CORROSION BEHAVIOR OF STEEL A3. *International Journal of Modern Physics B* **2010,** *24* (15-16), 3083-3088.
95. Sheng, X. X.; Ting, Y. P.; Pehkonen, S. A., The influence of sulphate-reducing bacteria biofilm on the corrosion of stainless steel AISI 316. *Corrosion Science* **2007,** *49* (5), 2159-2176.
96. White, D. C.; Arrage, A. A.; Nivens, D. E.; Palmer, R. J.; Rice, J. F.; Sayler, G. S., Biofilm ecology: On-line methods bring new insights into MIC and microbial biofouling. *Biofouling* **1996,** *10* (1-3), 3-&.
97. Dharmarajan, S.; Chandrasekaran, K.; Sundaram, M.; Narayanan, P., Electrochemical studies on the interfaces of freshwater biofilm/oxide film of alloy steels. *Vacuum* **2022,** *196*.
98. Borole, A. P.; Aaron, D.; Hamilton, C. Y.; Tsouris, C., Understanding Long-Term Changes in Microbial Fuel Cell Performance Using Electrochemical Impedance Spectroscopy. *Environmental Science & Technology* **2010,** *44* (7), 2740-2744.
99. He, Z.; Mansfeld, F., Exploring the use of electrochemical impedance spectroscopy (EIS) in microbial fuel cell studies. *Energy & Environmental Science* **2009,** *2* (2), 215-219.
100. Lepage, G.; Albernaz, F. O.; Perrier, G.; Merlin, G., Characterization of a microbial fuel cell with reticulated carbon foam electrodes. *Bioresource Technology* **2012,** *124*, 199-207.
101. Ramasamy, R. P.; Ren, Z. Y.; Mench, M. M.; Regan, J. M., Impact of initial biofilm growth on the anode impedance of microbial fuel cells. *Biotechnology and Bioengineering* **2008,** *101* (1), 101-108.
102. Kandpal, R.; Nara, S.; Shahadat, M.; Ansari, M. O.; Alshahrie, A.; Ali, S. W.; Ahammad, S. Z.; Malhotra, B. D., Impedance spectroscopic study of biofilm formation on pencil lead graphite anode in microbial fuel cell. *Journal of the Taiwan Institute of Chemical Engineers* **2021,** *128*, 114-123.

103. Sindhuja, M.; Kumar, N. S.; Sudha, V.; Harinipriya, S., Equivalent circuit modeling of microbial fuel cells using impedance spectroscopy. *Journal of Energy Storage* **2016,** *7*, 136-146.
104. Martin, E.; Savadogo, O.; Guiot, S. R.; Tartakovsky, B., Electrochemical characterization of anodic biofilm development in a microbial fuel cell. *Journal of Applied Electrochemistry* **2013,** *43* (5), 533-540.
105. Lochab, V.; Jones, T. H.; Alkandry, E.; West, J. D.; Abdel-Rahman, M. H.; Subramaniam, V. V.; Prakash, S., Evaluation of electrical properties of ex vivo human hepatic tissue with metastatic colorectal cancer. *Physiological measurement* **2020,** *41* (8), 085005.
106. Huiszoon, R. C.; Subramanian, S.; Rajasekaran, P. R.; Beardslee, L. A.; Bentley, W. E.; Ghodssi, R., Flexible platform for in situ impedimetric detection and bioelectric effect treatment of Escherichia coli biofilms. *IEEE Transactions on Biomedical Engineering* **2018,** *66* (5), 1337-1345.
107. Velasco, J. L. D.; Bernard, M. J. B.; Perez, G. T.; Olvera, L. G.; Lopez, H. S., Clinical efficacy of sodium alginate meshes for the control of infectious dissemination by Escherichia coli and Staphylococcus epidermidis in cavitated wounds with primary healing. *Veterinaria Mexico* **2012,** *43* (4), 285-293.
108. Ronco, T.; Aragao, M. F.; Svenningsen, S.; Christensen, J. B.; Permin, A.; Saaby, L.; Bionda, N.; Lantz, E. E.; Olsen, R. H., Efficacy of a novel antimicrobial hydrogel for eradication of Staphylococcus epidermidis, Staphylococcus aureus and Cutibacterium acnes from preformed biofilm and treatment performance in an in vivo MRSA wound model. *Jac-Antimicrobial Resistance* **2021,** *3* (3).
109. Roy, S.; Prakash, S.; Mathew-Steiner, S. S.; Das Ghatak, P.; Lochab, V.; Jones, T. H.; Mohana Sundaram, P.; Gordillo, G. M.; Subramaniam, V. V.; Sen, C. K., Disposable patterned electroceutical dressing (PED-10) is safe for treatment of open clinical chronic wounds. *Advances in wound care* **2019,** *8* (4), 149-159.
110. Stević, Z.; Vujasinović, M. R.; Radunović, M., Estimation of parameters obtained by electrochemical impedance spectroscopy on systems containing high capacities. *Sensors* **2009,** *9* (9), 7365-7373.
111. Muralidharan, V., Warburg impedance-basics revisited. *Anti-Corrosion Methods and Materials* **1997**.
112. Wilemski, G.; Fixman, M., General theory of diffusion-controlled reactions. *The Journal of chemical physics* **1973,** *58* (9), 4009-4019.
113. Calef, D. F.; Deutch, J., Diffusion-controlled reactions. *Annual Review of Physical Chemistry* **1983,** *34* (1), 493-524.
114. Bach, S.; Pereira-Ramos, J.; Baffier, N., Electrochemical properties of sol–gel Li4/3Ti5/3O4. *Journal of power sources* **1999,** *81*, 273-276.
115. Rho, Y. H.; Kanamura, K., Li+ ion diffusion in Li4Ti5O12 thin film electrode prepared by PVP sol–gel method. *Journal of Solid State Chemistry* **2004,** *177* (6), 2094-2100.
116. Barat, B. R.; Cano, E., The use of agar gelled electrolyte for in situ electrochemical measurements on metallic cultural heritage. *Electrochimica Acta* **2015,** *182*, 751-762.

117. Mech-Dorosz, A.; Khan, M. S.; Mateiu, R. V.; Hélix-Nielsen, C.; Emnéus, J.; Heiskanen, A., Impedance characterization of biocompatible hydrogel suitable for biomimetic lipid membrane applications. *Electrochimica Acta* **2021,** *373*, 137917.

Appendix A. Process Flow Documents

A.1 Fabricating glass slides with silver pattern

<table>
<tr><th>Step</th><th>Operation</th><th>Notes</th></tr>
<tr><td>1A</td><td>Pre-cleaning Part A</td><td>In chemical hood, add acetone to a soft polyester wipe and gently remove larger impurities from surface of glass on both sides.</td></tr>
<tr><td>1B</td><td>Precleaning Part B</td><td>Rinse both sides with IPA and blow dry with nitrogen gun.</td></tr>
<tr><td>2</td><td>Dehydration Bake/HMDS Vacuum Vapor Prime</td><td>OVN03 Standard Sequence at 150˚C
Device: Yield Engineering Systems YES-3 Vacuum Oven</td></tr>
<tr><td>3</td><td>AZ nLof 2020 Spin Coat (1.8 micron)</td><td>Pipette dispense. Cover most of sample with AZ nLOF 2020 negative photoresist. Will take 1 full pipette and one half-full. Spin Recipe below gives 1.8 micron thick photoresist on COT04
<table>
<tr><th>Speed (RPM)</th><th>Acceleration (RPM/s)</th><th>Time (sec)</th></tr>
<tr><td>300</td><td>100</td><td>5</td></tr>
<tr><td>3000</td><td>300</td><td>60</td></tr>
</table>
Device: Apogee Spin Coater</td></tr>
<tr><td>4</td><td>Soft Bake</td><td>Bake on COT03 Hotplate (constant temperature 115˚C) for 2.0 min.
Device: Cost Effective Equipment 100CB Spin Coater/Hot Plate</td></tr>
<tr><td>5</td><td>Expose</td><td>ALN02 Hard Contact exposure for 7.0 seconds
Device: EV 620 Aligner</td></tr>
<tr><td>6</td><td>Post-exposure Bake</td><td>Bake on COT03 Hotplate (constant temperature 115˚C) for 1.5 min.
Device: Cost Effective Equipment 100CB Spin Coater/Hot Plate</td></tr>
<tr><td>7A</td><td>Develop Part A</td><td>Submerge sample in MF-CD-26 Developer in a glass dish for 60 seconds. The dish should be less than halfway full of developer such that the dish can be moved around in circles</td></tr>
</table>

		slowly. This allows fresh developer to continually flow over the surface of the glass slide in waves.
7B	Develop Part B	Rinse both sides with DI water for 30 seconds and blow dry with nitrogen gun.
8	First Microscope Inspection	Examine pattern under microscope and ensure spacing and radii measurements match the nominal dimensions. This will ensure pattern is correct. If sample is damaged, save and reclean the glass to be used later. *Device: NanoScience Zeta-20 3D Optical Profilometer*
9	Coat with Silver	Evaporate 100 nm of silver onto the slides (ensure the side with photoresist is the one that is coated). *Device: CHA Solution System E-Gun Evaporator*
10	Lift-off/Strip	Immerse in hot 80˚C NMP solution for at least 15 minutes. Multiple samples can be immersed in the same dish provided they do not overlap.
11	Rinse and Dry	Rinse sample thoroughly with Methanol, IPA rinse, then blow dry with nitrogen gun.
12	Second Microscope Inspection	Measure the width of the electrode, the space between turns, the inner radius of a turn, and the outer radius of a turn at 5 locations for each sample. This will ensure pattern is correct. If sample is damaged, save and reclean the glass to be used later. *Device: NanoScience Zeta-20 3D Optical Profilometer*

A.2 Fabricating and attaching PDMS barriers

Step	Operation	Notes
1A	PDMS Mixing Part A	In a new plastic cup, weigh Sylgard 184 silicone elastomer in a 10:1 ratio by weight with a final weight of 33 g.
1B	PDMS Mixing Part B	Use a new wooden tongue depressor to thoroughly mix the PDMS for 60 seconds until it is nearly opaque.
2	Degas	Place the cup and PDMS mixture into vacuum chamber and degas for 1 hour until all air bubbles have risen and popped. *Device: Bel-Art SP Scienceware Vacuum Desiccator*
3	Prepare Acrylic Molds	Use scotch tape to attach the top of the mold to the base of the mold. Two molds can be filled with 33 g of PDMS.
4	Fill Molds	Slowly pour PDMS out of the plastic cup into the corner of one mold and fill until the mold is 50% full. Pour the other half of the PDMS into a second mold.
5	Cure PDMS	Place the molds on a hotplate set to 70˚C and cure for 4 hours.
6	Remove PDMS Barriers	Remove all tape from the molds. Using a pen knife, cut around the inside and outside edges of the PDMS to the base of the mold. Slide off the top piece of the mold, then slide the PDMS barrier off the center of the mold. Trim any excess PDMS and store the barriers in a clean petri dish.
7	Cleaning PDMS Barriers	Using clear packing tape, gently remove excess PDMS and other debris from the bottom surface of the PDMS barriers.
8	Plasma Bonding	Follow the plasma bonding procedure and ignite plasma for 30 seconds. Remove and attach PDMS to substrates as quickly as possible.

A.3 Preparation of devices with TSA and biofilm

Step	Operation	Notes
1	Inoculate Overnight Culture	Add 25 mL of TSB to a new centrifuge tube. Use an inoculation loop to remove 1 colony of *S. epidermidis* from a streaked plate and add to the TSB. Place in a shaker incubator at 37˚C for 18 hours.
2	Dilute Inoculation	Add 9.9 mL of TSB to a new centrifuge tube. Vortex mix the overnight culture for 10 seconds, then add 100 µL of overnight culture. Refrigerate up to 48 hours until ready to use.
3	Prepare Dishes	Autoclave TSA powder and DI water in a 40g to 1 L ratio. Allow the TSA to cool for 10-15 minutes. Meanwhile, draw two 2" x 1" rectangles on the outside of the petri dishes so that the lines will be visible below the TSA once solid.
4	Add TSA to Dishes	Add 8.9 mL of the TSA to each 9 cm petri dish to result in a 1.4 mm high agar layer. Gently rotate the dish to ensure an even coating and allow the TSA to solidify and cool completely. Refrigerate the dishes upside-down until ready to use.
5	Add Bacteria to Dishes	Add 165 µL of the diluted *S. epidermidis* solution to the surface of the TSA, then use a cell spreader to evenly spread the solution around. Be very careful to not disturb the surface of the thin TSA layer. Allow the surface to dry for 30 minutes under a biosafety cabinet, then place into a 37˚C incubator for the desired growth duration. If only measuring TSA, skip this step and proceed to step 6.
6	Place Media in Devices	Remove dishes from the incubator. Using a clean inoculation loop, trace around the two rectangles drawn on the dishes to cut out the TSA and biofilm. Gently slide the inoculation loop under the surface of the TSA, which should easily detach from the bottom of the dish. Place the media into the device well with biofilm-side up and make sure the media is flat on the surface of the electrodes.
7	EIS Measurements	Complete EIS measurements within 1 hour of removing the measured media from the incubator.

A.4 Process for producing a 5-inch chrome photomask on quartz plate

<table>
<tr><th>Step</th><th>Operation</th><th>Notes</th></tr>
<tr><td>A</td><td>Strip old resist</td><td>Strip old photoresist on mask blank with acetone followed by 2-propanol rinse. Blow dry.</td></tr>
<tr><td>1</td><td>Dehydration Bake</td><td>Bay Temp: Humidity:
Hotplate 180ºC for 5.0 min</td></tr>
<tr><td>2</td><td>AZ nLOF 2020
spin coat
(1.8 micron)</td><td>Pipette dispense. Cover most of the mask with AZ nLOF 2020.
Spin recipe below gives 1.8 micron thick photoresist.
COT04
<table>
<tr><th>Speed (RPM)</th><th>Acceleration (RPM/s)</th><th>Time (sec)</th></tr>
<tr><td>300</td><td>100</td><td>5</td></tr>
<tr><td>3000</td><td>300</td><td>60</td></tr>
</table></td></tr>
<tr><td>3</td><td>Soft bake</td><td>COT03 Hotplate 115ºC for 1.0 min
(actual hotplate temperature, not set point)</td></tr>
<tr><td>4</td><td>Expose</td><td>MLA01
Laser: 375 nm (Do NOT use 405 laser)
Optical Autofocus
Dose: 140 mJ
Defocus: 0</td></tr>
<tr><td>5</td><td>Post exposure bake: REQUIRED</td><td>COT03 Hotplate 115ºC for 1.5 minutes (REQUIRED)
(actual hotplate temperature, not set point)</td></tr>
<tr><td>6</td><td>Develop</td><td>HOD08
MF-CD-26 Developer in glass dish: 60 to 75 seconds
Swirl and agitate developer solution slightly
DI rinse 30 sec, blow dry</td></tr>
<tr><td>7</td><td>Microscope Inspection: Bay 2</td><td>Use yellow filter in Nikon microscope to avoid exposing resist if you possibly may need additional developing
Inspect to ensure pattern quality. Ensure that unexposed areas of substrate are absent of photoresist and clear. Perform additional development if not cleared.</td></tr>
<tr><td>8</td><td>Etch chrome</td><td>Wet etch away the resist-free clear chromium in Transene Nichrome Etch bath. After clear, rinse thoroughly in DI water</td></tr>
<tr><td>9</td><td>Strip photoresist</td><td>Immerse in hot 80C AZ Kwik Strip or NMP solution.
Room temperature NMP is not recommended: resist may not fully dissolve in cold NMP.
Do NOT use acetone as resist will not dissolve.</td></tr>
</table>

9 (cont.)	Strip photoresist (cont.)	Glass beaker on hotplate in solvent hood: at least 20.0 min in 80ºC AZ Kwik Strip or NMP solution (actual liquid temperature, not the hotplate setpoint)
10	Rinse and Dry	For NMP: rinse sample thoroughly with Methanol, IPA rinse then N_2 Dry For AZ Kwik Strip: rinse sample thoroughly with clean AZ Kwik Strip, IPA rinse then N_2 Dry

Appendix B. MATLAB Code

B.1 Code used for Figures 3 and 4

```
% Input Values
R = 10;                                 %Resistance (ohm)
C = 1e-9;                               %Capacitance (F)
f = linspace(1,1e12, 10000000);         %Frequency range (Hz)
w = 2*pi.*f;                            %Omega
Z_C = 1./(1i.*w*C);                     %Impedance of capacitor (ohm)
L = 1e-10;                              %Inductance (H)
Z_L = 1i.*w*L;                          %Impedance of inductor (ohm)

% Resistor and capacitor in series
Z_rcs = R+Z_C;                          %Impedance in Ohms
phi_rcs = rad2deg(angle(Z_rcs));        %Phase in degrees

figure(1);
subplot(2,1,1)
loglog(f,abs(Z_rcs))
xlim([1,1e12]);
ylim([min(abs(Z_rcs)),max(abs(Z_rcs))]);

subplot(2,1,2)
semilogx(f,phi_rcs)
xlim([1,1e12]);
ylim([-180,180]);
yticks([-180 -90 0 90 180])

figure(2);
plot(real(Z_rcs),imag(Z_rcs))
xlim([0,12]);

% Resistor and capacitor in parallel
Z_rcp = 1./((1./R)+(1./Z_C));           %Impedance in Ohms
phi_rcp = rad2deg(angle(Z_rcp));        %Phase in degrees

figure(3);
subplot(2,1,1)
loglog(f,abs(Z_rcp))
xlim([1,1e12]);
ylim([min(abs(Z_rcp)),max(abs(Z_rcp))]);

subplot(2,1,2)
semilogx(f,phi_rcp)
xlim([1,1e12]);
ylim([-180,180]);
yticks([-180 -90 0 90 180])
```

```
figure(4);
plot(real(Z_rcp),imag(Z_rcp))
xlim([0,12]);

% Resistor, Capacitor, Inductor in series
Z_rcls = R+Z_C+Z_L;                     %Impedance in Ohms
phi_rcls = rad2deg(angle(Z_rcls));      %Phase in degrees

figure(5);
subplot(2,1,1)
loglog(f,abs(Z_rcls))
xlim([1,1e12]);
ylim([min(abs(Z_rcls)),max(abs(Z_rcls))]);

subplot(2,1,2)
semilogx(f,phi_rcls)
xlim([1,1e12]);
ylim([-180,180]);
yticks([-180 -90 0 90 180])

figure(6);
plot(real(Z_rcls),imag(Z_rcls))
xlim([0,12]);

% Resistor, Capacitor, Inductor in parallel

Z_rclp = 1./((1./R)+(1./Z_C)+(1./Z_L)); %Impedance in Ohms
phi_rclp = rad2deg(angle(Z_rclp));      %Phase in degrees

figure(7);
subplot(2,1,1)
loglog(f,abs(Z_rclp))
xlim([1,1e12]);
ylim([min(abs(Z_rclp)),max(abs(Z_rclp))]);

subplot(2,1,2)
semilogx(f,phi_rclp)
xlim([1,1e12]);
ylim([-180,180]);
yticks([-180 -90 0 90 180])

figure(8);
plot(real(Z_rclp),imag(Z_rclp))
xlim([0,12]);
```

Published with MATLAB® R2019b

B.2 Code used for Figures 11-14 and 20-38

Two-electrode measurements: Agar

```
Freq = table2array(ElectrodeMeasurements(:,3));                % Frequency range(Hz)

% Agar Sample 1
S1RAgar = table2array(ElectrodeMeasurements(:,16));            % Real impedance (ohm)
S1IAgar = table2array(ElectrodeMeasurements(:,17));            % Imaginary impedance
(ohm)
S1MAgar = table2array(ElectrodeMeasurements(:,18));            % Magnitude of impedance
(ohm)
S1PAgar = table2array(ElectrodeMeasurements(:,19));            % Phase (deg)

% Agar Sample 2
S2RAgar = table2array(ElectrodeMeasurementsS1(:,16));
S2IAgar = table2array(ElectrodeMeasurementsS1(:,17));
S2MAgar = table2array(ElectrodeMeasurementsS1(:,18));
S2PAgar = table2array(ElectrodeMeasurementsS1(:,19));

% Agar Sample 4 (Sample 3 discarded)
S4RAgar = table2array(ElectrodeMeasurementsS3(:,16));
S4IAgar = table2array(ElectrodeMeasurementsS3(:,17));
S4MAgar = table2array(ElectrodeMeasurementsS3(:,18));
S4PAgar = table2array(ElectrodeMeasurementsS3(:,19));

AvgRealAgar = (S1RAgar+S2RAgar+S4RAgar)./3;                    % Averages of all samples
AvgImagAgar = (S1IAgar+S2IAgar+S4IAgar)./3;
AvgModAgar = (S1MAgar+S2MAgar+S4MAgar)./3;
AvgPhaseAgar = (S1PAgar+S2PAgar+S4PAgar)./3;

% Calculating error bar values
% Real Impedance
RValsAgar = [S1RAgar,S2RAgar,S4RAgar]';
RsdAgar = transpose(std(RValsAgar));

% Imaginary Impedance
IValsAgar = [S1IAgar,S2IAgar,S4IAgar]';
IsdAgar = transpose(std(IValsAgar));

% Magnitude
MValsAgar = [S1MAgar,S2MAgar,S4MAgar]';
MsdAgar = transpose(std(MValsAgar));

% Phase
PValsAgar = [S1PAgar,S2PAgar,S4PAgar]';
PsdAgar = transpose(std(PValsAgar));

% Find corner frequency
x1=log10(Freq(1:21));
```

```
y1=log10(AvgModAgar(1:21));
Line1 = polyfit(x1,y1,1);
fit1 = 10.^(Line1(1).*log10(Freq) + Line1(2));
x2=log10(Freq(41:57));
y2=log10(AvgModAgar(41:57));
Line2 = polyfit(x2,y2,1);
fit2 = 10.^(Line2(1).*log10(Freq) + Line2(2));
cornerfreqAgar = 10^((Line2(2) - Line1(2)) / (Line1(1) - Line2(1)));

CPEAgar = mean(AvgPhaseAgar(1:21));
```

0 hr biofilm

```
% 0 hr Sample 1
S1R0hr = table2array(Wire0hour(:,16));
S1I0hr = table2array(Wire0hour(:,17));
S1M0hr = table2array(Wire0hour(:,18));
S1P0hr = table2array(Wire0hour(:,19));

% 0 hr Sample 3
S2R0hr = table2array(Wire0hourS2(:,16));
S2I0hr = table2array(Wire0hourS2(:,17));
S2M0hr = table2array(Wire0hourS2(:,18));
S2P0hr = table2array(Wire0hourS2(:,19));

% 0 hr Sample 4
S3R0hr = table2array(Wire0hourS3(:,16));
S3I0hr = table2array(Wire0hourS3(:,17));
S3M0hr = table2array(Wire0hourS3(:,18));
S3P0hr = table2array(Wire0hourS3(:,19));

AvgReal0hr = (S1R0hr+S2R0hr+S3R0hr)./3;
AvgImag0hr = (S1I0hr+S2I0hr+S3I0hr)./3;
AvgMod0hr = (S1M0hr+S2M0hr+S3M0hr)./3;
AvgPhase0hr = (S1P0hr+S2P0hr+S3P0hr)./3;

% Calculating error bar values
% Real Impedance
RVals0hr = [S1R0hr,S2R0hr,S3R0hr]';
Rsd0hr = transpose(std(RVals0hr));

% Imaginary Impedance
IVals0hr = [S1I0hr,S2I0hr,S3I0hr]';
Isd0hr = transpose(std(IVals0hr));

% Magnitude
MVals0hr = [S1M0hr,S2M0hr,S3M0hr]';
Msd0hr = transpose(std(MVals0hr));

% Phase
```

```
PValsOhr = [S1POhr,S2POhr,S3POhr]';
PsdOhr = transpose(std(PValsOhr));

% Find corner frequency
x1=log10(Freq(1:21));
y1=log10(AvgModOhr(1:21));
Line1 = polyfit(x1,y1,1);
fit1 = 10.^(Line1(1).*log10(Freq) + Line1(2));
x2=log10(Freq(41:57));
y2=log10(AvgModOhr(41:57));
Line2 = polyfit(x2,y2,1);
fit2 = 10.^(Line2(1).*log10(Freq) + Line2(2));
cornerfreqOhr = 10^((Line2(2) - Line1(2)) / (Line1(1) - Line2(1)));

CPEOhr = mean(AvgPhaseOhr(1:21));
```

8 hr biofilms

```
% % 8 hr Sample 1
% S1R8hr = table2array(Wire8hour(:,16));
% S1I8hr = table2array(Wire8hour(:,17));
% S1M8hr = table2array(Wire8hour(:,18));
% S1P8hr = table2array(Wire8hour(:,19));

% 8 hr Sample 2
S2R8hr = table2array(Wire8hourS1(:,16));
S2I8hr = table2array(Wire8hourS1(:,17));
S2M8hr = table2array(Wire8hourS1(:,18));
S2P8hr = table2array(Wire8hourS1(:,19));

% 8 hr Sample 3
S3R8hr = table2array(Wire8hourS2(:,16));
S3I8hr = table2array(Wire8hourS2(:,17));
S3M8hr = table2array(Wire8hourS2(:,18));
S3P8hr = table2array(Wire8hourS2(:,19));

% 8 hr Sample 4
S4R8hr = table2array(Wire8hourS3(:,16));
S4I8hr = table2array(Wire8hourS3(:,17));
S4M8hr = table2array(Wire8hourS3(:,18));
S4P8hr = table2array(Wire8hourS3(:,19));

% 8 hr Sample 6
S5R8hr = table2array(Wire8hourS5(:,16));
S5I8hr = table2array(Wire8hourS5(:,17));
S5M8hr = table2array(Wire8hourS5(:,18));
S5P8hr = table2array(Wire8hourS5(:,19));


AvgReal8hr = (S5R8hr+S2R8hr+S3R8hr+S4R8hr)./4;
```

```
AvgImag8hr = (S5I8hr+S2I8hr+S3I8hr+S4I8hr)./4;
AvgMod8hr = (S5M8hr+S2M8hr+S3M8hr+S4M8hr)./4;
AvgPhase8hr = (S5P8hr+S2P8hr+S3P8hr+S4P8hr)./4;

% Calculating error bar values
% Real Impedance
RVals8hr = [S5R8hr,S2R8hr,S3R8hr,S4R8hr]';
Rsd8hr = transpose(std(RVals8hr));

% Imaginary Impedance
IVals8hr = [S5I8hr,S2I8hr,S3I8hr,S4I8hr]';
Isd8hr = transpose(std(IVals8hr));

% Magnitude
MVals8hr = [S5M8hr,S2M8hr,S3M8hr,S4M8hr]';
Msd8hr = transpose(std(MVals8hr));

% Phase
PVals8hr = [S5P8hr,S2P8hr,S3P8hr,S4P8hr]';
Psd8hr = transpose(std(PVals8hr));

% Find corner frequency
x1=log10(Freq(1:21));
y1=log10(AvgMod8hr(1:21));
Line1 = polyfit(x1,y1,1);
fit1 = 10.^(Line1(1).*log10(Freq) + Line1(2));
x2=log10(Freq(41:57));
y2=log10(AvgMod8hr(41:57));
Line2 = polyfit(x2,y2,1);
fit2 = 10.^(Line2(1).*log10(Freq) + Line2(2));
cornerfreq8hr = 10^((Line2(2) - Line1(2)) / (Line1(1) - Line2(1)));

CPE8hr = mean(AvgPhase8hr(1:21));
```

16 hour

```
% Agar Sample 1
S1R16hr = table2array(Wire16hour(:,16));
S1I16hr = table2array(Wire16hour(:,17));
S1M16hr = table2array(Wire16hour(:,18));
S1P16hr = table2array(Wire16hour(:,19));

% Agar Sample 2
S2R16hr = table2array(Wire16hourS1(:,16));
S2I16hr = table2array(Wire16hourS1(:,17));
S2M16hr = table2array(Wire16hourS1(:,18));
S2P16hr = table2array(Wire16hourS1(:,19));

% Agar Sample 3
S3R16hr = table2array(Wire16hourS2(:,16));
```

```
S3I16hr = table2array(Wire16hourS2(:,17));
S3M16hr = table2array(Wire16hourS2(:,18));
S3P16hr = table2array(Wire16hourS2(:,19));

AvgReal16hr = (S1R16hr+S2R16hr+S3R16hr)./3;
AvgImag16hr = (S1I16hr+S2I16hr+S3I16hr)./3;
AvgMod16hr = (S1M16hr+S2M16hr+S3M16hr)./3;
AvgPhase16hr = (S1P16hr+S2P16hr+S3P16hr)./3;

% Calculating error bar values
% Real Impedance
RVals16hr = [S1R16hr,S2R16hr,S3R16hr]';
Rsd16hr = transpose(std(RVals16hr));

% Imaginary Impedance
IVals16hr = [S1I16hr,S2I16hr,S3I16hr]';
Isd16hr = transpose(std(IVals16hr));

% Magnitude
MVals16hr = [S1M16hr,S2M16hr,S3M16hr]';
Msd16hr = transpose(std(MVals16hr));

% Phase
PVals16hr = [S1P16hr,S2P16hr,S3P16hr]';
Psd16hr = transpose(std(PVals16hr));

% Find corner frequency
x1=log10(Freq(1:21));
y1=log10(AvgMod16hr(1:21));
Line1 = polyfit(x1,y1,1);
fit1 = 10.^(Line1(1).*log10(Freq) + Line1(2));
x2=log10(Freq(41:57));
y2=log10(AvgMod16hr(41:57));
Line2 = polyfit(x2,y2,1);
fit2 = 10.^(Line2(1).*log10(Freq) + Line2(2));
cornerfreq16hr = 10^((Line2(2) - Line1(2)) / (Line1(1) - Line2(1)));

CPE16hr = mean(AvgPhase16hr(1:21));
```

24 hr biofilm

```
% Agar Sample 5
S1R24hr = table2array(Wire24hourS4(:,16));
S1I24hr = table2array(Wire24hourS4(:,17));
S1M24hr = table2array(Wire24hourS4(:,18));
S1P24hr = table2array(Wire24hourS4(:,19));

% Agar Sample 6
S2R24hr = table2array(Wire24hourS5(:,16));
S2I24hr = table2array(Wire24hourS5(:,17));
```

```
S2M24hr = table2array(Wire24hourS5(:,18));
S2P24hr = table2array(Wire24hourS5(:,19));

% Agar Sample 7
S3R24hr = table2array(Wire24hourS6(:,16));
S3I24hr = table2array(Wire24hourS6(:,17));
S3M24hr = table2array(Wire24hourS6(:,18));
S3P24hr = table2array(Wire24hourS6(:,19));


AvgReal24hr = (S1R24hr+S2R24hr+S3R24hr)./3;
AvgImag24hr = (S1I24hr+S1I24hr+S3I24hr)./3;
AvgMod24hr = (S1M24hr+S2M24hr+S3M24hr)./3;
AvgPhase24hr = (S1P24hr+S2P24hr+S3P24hr)./3;

% Calculating error bar values
% Real Impedance
RVals24hr = [S1R24hr,S2R24hr,S3R24hr]';
Rsd24hr = transpose(std(RVals24hr));

% Imaginary Impedance
IVals24hr = [S1I24hr,S2I24hr,S3I24hr]';
Isd24hr = transpose(std(IVals24hr));

% Magnitude
MVals24hr = [S1M24hr,S2M24hr,S3M24hr]';
Msd24hr = transpose(std(MVals24hr));

% Phase
PVals24hr = [S1P24hr,S2P24hr,S3P24hr]';
Psd24hr = transpose(std(PVals24hr));

% Find corner frequency
x1=log10(Freq(1:21));
y1=log10(AvgMod24hr(1:21));
Line1 = polyfit(x1,y1,1);
fit1 = 10.^(Line1(1).*log10(Freq) + Line1(2));
x2=log10(Freq(41:57));
y2=log10(AvgMod24hr(41:57));
Line2 = polyfit(x2,y2,1);
fit2 = 10.^(Line2(1).*log10(Freq) + Line2(2));
cornerfreq24hr = 10^((Line2(2) - Line1(2)) / (Line1(1) - Line2(1)));

CPE24hr = mean(AvgPhase24hr(1:21));
```

Magnitude Bode Plots

```
% Bode plot for average of all agar samples
figure(1)
errorbar(Freq,AvgModAgar,MsdAgar,'Color',[0.5 0.5 0.5])
```

```
xlim([1e-1 1e6])
ylim([1e0 1e4])
set(gca, 'XScale','log', 'YScale','log')
hold on
plot(Freq,AvgModAgar,'-','Color','black','LineWidth',2)
xlabel('Frequency (Hz)')
ylabel('Magnitude (ohms)')
hold off

% Bode plot for average of all 0hr samples
figure(2)
errorbar(Freq,AvgMod0hr,Msd0hr,'Color',[0.5 0.5 0.5])
xlim([1e-1 1e6])
ylim([1e0 1e4])
set(gca, 'XScale','log', 'YScale','log')
hold on
plot(Freq,AvgMod0hr,'-','Color','#AD0000','LineWidth',2)
xlabel('Frequency (Hz)')
ylabel('Magnitude (ohms)')
hold off

% Bode plot for average of all 8hr samples
figure(3)
errorbar(Freq,AvgMod8hr,Msd8hr,'Color',[0.5 0.5 0.5])
xlim([1e-1 1e6])
ylim([1e0 1e4])
set(gca, 'XScale','log', 'YScale','log')
hold on
plot(Freq,AvgMod8hr,'-','Color','#F4631E','LineWidth',2)
xlabel('Frequency (Hz)')
ylabel('Magnitude (ohms)')
hold off

% Bode plot for average of all 16hr samples
figure(4)
errorbar(Freq,AvgMod16hr,Msd16hr,'Color',[0.5 0.5 0.5])
xlim([1e-1 1e6])
ylim([1e0 1e4])
set(gca, 'XScale','log', 'YScale','log')
hold on
plot(Freq,AvgMod16hr,'-','Color','#FF9F00','LineWidth',2)
xlabel('Frequency (Hz)')
ylabel('Magnitude (ohms)')
hold off

% Bode plot for average of all 24 hour samples
figure(5)
errorbar(Freq,AvgMod24hr,Msd24hr,'Color',[0.5 0.5 0.5])
xlim([1e-1 1e6])
ylim([1e0 1e4])
set(gca, 'XScale','log', 'YScale','log')
```

```
hold on
plot(Freq,AvgMod24hr,'-','Color','#007E7E','LineWidth',2)
xlabel('Frequency (Hz)')
ylabel('Magnitude (ohms)')
hold off
% legend('Agar','Agar','0 hours','0 hours', '8 hours',  '8 hours','16 hours', '16
hours','24 hours','24 hours')

hold off


% Bode plot for average of all agar samples
figure(6)
plot(Freq,AvgModAgar,'-','Color','black','LineWidth',2)
xlim([1e-1 1e6])
ylim([1e0 1e4])
set(gca, 'XScale','log', 'YScale','log')
xlabel('Frequency (Hz)')
ylabel('Magnitude (ohms)')
hold on

% Bode plot for average of all 0hr samples
plot(Freq,AvgMod0hr,'-','Color','#AD0000','LineWidth',2)
xlim([1e-1 1e6])
ylim([1e0 1e4])
set(gca, 'XScale','log', 'YScale','log')

% Bode plot for average of all 8hr samples
plot(Freq,AvgMod8hr,'-','Color','#F4631E','LineWidth',2)
xlim([1e-1 1e6])
ylim([1e0 1e4])
set(gca, 'XScale','log', 'YScale','log')

% Bode plot for average of all 16hr samples
plot(Freq,AvgMod16hr,'-','Color','#FF9F00','LineWidth',2)
xlim([1e-1 1e6])
ylim([1e0 1e4])
set(gca, 'XScale','log', 'YScale','log')

% Bode plot for average of all 24 hour samples
plot(Freq,AvgMod24hr,'-','Color','#007E7E','LineWidth',2)
xlim([1e-1 1e6])
ylim([1e0 1e4])
set(gca, 'XScale','log', 'YScale','log')
legend('Agar','0 hours','8 hours','16 hours','24 hours')
hold off
```

Phase Bode plots
Bode plot for average of all agar samples

```
figure(7)
errorbar(Freq,AvgPhaseAgar,PsdAgar,'Color',[0.5 0.5 0.5])
xlim([1e-1 1e6])
ylim([-90 90])
yticks([-90 -45 0 45 90])
set(gca, 'XScale','log')
xlabel('Frequency (Hz)')
ylabel('Phase (degrees)')
hold on
plot(Freq,AvgPhaseAgar,'-','Color','black','LineWidth',2)
hold off

% Bode plot for average of all 0hr samples
figure(8)
errorbar(Freq,AvgPhase0hr,Psd0hr,'Color',[0.5 0.5 0.5])
xlim([1e-1 1e6])
ylim([-90 90])
yticks([-90 -45 0 45 90])
set(gca, 'XScale','log')
xlabel('Frequency (Hz)')
ylabel('Phase (degrees)')
hold on
plot(Freq,AvgPhase0hr,'-','Color','#AD0000','LineWidth',2)
hold off

% Bode plot for average of all 8hr samples
figure(9)
errorbar(Freq,AvgPhase8hr,Psd8hr,'Color',[0.5 0.5 0.5])
xlim([1e-1 1e6])
ylim([-90 90])
yticks([-90 -45 0 45 90])
set(gca, 'XScale','log')
xlabel('Frequency (Hz)')
ylabel('Phase (degrees)')
hold on
plot(Freq,AvgPhase8hr,'-','Color','#F4631E','LineWidth',2)
hold off

% Bode plot for average of all 16hr samples
figure(10)
errorbar(Freq,AvgPhase16hr,Psd16hr,'Color',[0.5 0.5 0.5])
xlim([1e-1 1e6])
ylim([-90 90])
yticks([-90 -45 0 45 90])
set(gca, 'XScale','log')
xlabel('Frequency (Hz)')
ylabel('Phase (degrees)')
hold on
plot(Freq,AvgPhase16hr,'-','Color','#FF9F00','LineWidth',2)
hold off
```

```
% Bode plot for average of all 24 hour samples
figure(11)
errorbar(Freq,AvgPhase24hr,Psd24hr,'Color',[0.5 0.5 0.5])
xlim([1e-1 1e6])
ylim([-90 90])
yticks([-90 -45 0 45 90])
set(gca, 'XScale','log')
xlabel('Frequency (Hz)')
ylabel('Phase (degrees)')
hold on
plot(Freq,AvgPhase24hr,'-','Color','#007E7E','LineWidth',2)
hold off

% Bode plot for average of all agar samples
figure(12)
plot(Freq,AvgPhaseAgar,'-','Color','black','LineWidth',2)
xlim([1e-1 1e6])
ylim([-90 90])
yticks([-90 -45 0 45 90])
set(gca, 'XScale','log')
xlabel('Frequency (Hz)')
ylabel('Phase (degrees)')
hold on

% Bode plot for average of all 0hr samples
plot(Freq,AvgPhase0hr,'-','Color','#AD0000','LineWidth',2)
xlim([1e-1 1e6])
ylim([-90 90])
yticks([-90 -45 0 45 90])
set(gca, 'XScale','log')

% Bode plot for average of all 8hr samples
plot(Freq,AvgPhase8hr,'-','Color','#F4631E','LineWidth',2)
xlim([1e-1 1e6])
ylim([-90 90])
yticks([-90 -45 0 45 90])
set(gca, 'XScale','log')

% Bode plot for average of all 16hr samples
plot(Freq,AvgPhase16hr,'-','Color','#FF9F00','LineWidth',2)
xlim([1e-1 1e6])
ylim([-90 90])
yticks([-90 -45 0 45 90])
set(gca, 'XScale','log')

% Bode plot for average of all 24 hour samples
plot(Freq,AvgPhase24hr,'-','Color','#007E7E','LineWidth',2)
xlim([1e-1 1e6])
ylim([-90 90])
yticks([-90 -45 0 45 90])
```

```
set(gca, 'XScale','log')
legend('Agar','0 hours', '8 hours', '16 hours', '24 hours')
hold off
```

VERTICAL ERROR: Nyquist plot for average of all agar samples

```
figure(13)
errorbar(AvgRealAgar,abs(AvgImagAgar),RsdAgar,RsdAgar,'Color',[0.5 0.5 0.5])
xlim([0 500])
ylim([0 450])
xlabel('Real Impedance (ohms)')
ylabel('-Imaginary Imepdance(ohms)')
hold on
plot(AvgRealAgar,abs(AvgImagAgar),'-','Color','black','LineWidth',2)
hold off

% Nyquist plot for average of all 0hr samples
figure(14)
errorbar(AvgReal0hr,abs(AvgImag0hr),Rsd0hr,Rsd0hr,'Color',[0.5 0.5 0.5])
xlim([0 1800])
ylim([0 1800])
xlabel('Real Impedance (ohms)')
ylabel('-Imaginary Imepdance(ohms)')
hold on
plot(AvgReal0hr,abs(AvgImag0hr),'-','Color','#AD0000','LineWidth',2)
hold off

% Nyquist plot for average of all 8hr samples
figure(15)
errorbar(AvgReal8hr,abs(AvgImag8hr),Rsd8hr,Rsd8hr,'Color',[0.5 0.5 0.5])
xlim([0 2500])
ylim([0 4000])
xlabel('Real Impedance (ohms)')
ylabel('-Imaginary Imepdance(ohms)')
hold on
plot(AvgReal8hr,abs(AvgImag8hr),'-','Color','#F4631E','LineWidth',2)
hold off

% Nyquist plot for average of all 16hr samples
figure(16)
errorbar(AvgReal16hr,abs(AvgImag16hr),Rsd16hr,Rsd16hr,'Color',[0.5 0.5 0.5])
xlim([0 2000])
ylim([0 3000])
xlabel('Real Impedance (ohms)')
ylabel('-Imaginary Imepdance(ohms)')
hold on
plot(AvgReal16hr,abs(AvgImag16hr),'-','Color','#FF9F00','LineWidth',2)
hold off
```

```
% Nyquist plot for average of all 24hr samples
figure(17)
errorbar(AvgReal24hr,abs(AvgImag24hr),Rsd24hr,Rsd24hr,'Color',[0.5 0.5 0.5])
xlim([0 1500])
ylim([0 2500])
xlabel('Real Impedance (ohms)')
ylabel('-Imaginary Imepdance(ohms)')
hold on
plot(AvgReal24hr,abs(AvgImag24hr),'-','Color','#007E7E','LineWidth',2)
hold off


% All nyquist vertical error
figure(18)
plot(AvgRealAgar,abs(AvgImagAgar),'-','Color','black','LineWidth',2)
xlim([0 4000])
ylim([0 4000])
xlabel('Real Impedance (ohms)')
ylabel('-Imaginary Imepdance(ohms)')
hold on

% Nyquist plot for average of all 0hr samples
plot(AvgReal0hr,abs(AvgImag0hr),'-','Color','#AD0000','LineWidth',2)
xlim([0 4000])
ylim([0 4000])
xlabel('Real Impedance (ohms)')
ylabel('-Imaginary Imepdance(ohms)')

% Nyquist plot for average of all 8hr samples
plot(AvgReal8hr,abs(AvgImag8hr),'-','Color','#F4631E','LineWidth',2)
xlim([0 4000])
ylim([0 4000])
xlabel('Real Impedance (ohms)')
ylabel('-Imaginary Imepdance(ohms)')

% Nyquist plot for average of all 16hr samples
plot(AvgReal16hr,abs(AvgImag16hr),'-','Color','#FF9F00','LineWidth',2)
xlim([0 4000])
ylim([0 4000])
xlabel('Real Impedance (ohms)')
ylabel('-Imaginary Imepdance(ohms)')

% Nyquist plot for average of all 24hr samples
plot(AvgReal24hr,abs(AvgImag24hr),'-','Color','#007E7E','LineWidth',2)
xlim([0 4000])
ylim([0 4000])
xlabel('Real Impedance (ohms)')
ylabel('-Imaginary Imepdance(ohms)')
legend('Agar','0 hours', '8 hours', '16 hours', '24 hours')
hold off
```

HORIZONTAL ERROR: Nyquist plot for average of all agar samples

```
figure(19)
errorbar(AvgRealAgar,abs(AvgImagAgar),IsdAgar,IsdAgar,'horizontal','Color',[0.5 0.5 0.5])
xlim([0 500])
ylim([0 450])
xlabel('Real Impedance (ohms)')
ylabel('-Imaginary Imepdance(ohms)')
hold on
plot(AvgRealAgar,abs(AvgImagAgar),'-','Color','black','LineWidth',2)
hold off

% Nyquist plot for average of all 0hr samples
negIsd0hr = zeros(1, length(Isd0hr));
for i = 1:length(Isd0hr)
    if Isd0hr(i) > Avgreal0hr(i)
        negIsd0hr(i) = Avgreal0hr(i);
    else
        negIsd0hr(i) = Isd0hr(i);
    end
end

figure(20)
errorbar(Avgreal0hr,abs(Avgimag0hr),negIsd0hr,Isd0hr,'horizontal','Color',[0.5 0.5 0.5])
xlim([0 1800])
ylim([0 1800])
xlabel('Real Impedance (ohms)')
ylabel('-Imaginary Imepdance(ohms)')
hold on
plot(Avgreal0hr,abs(Avgimag0hr),'-','Color','#AD0000','LineWidth',2)
hold off

% Nyquist plot for average of all 8hr samples
figure(21)
errorbar(Avgreal8hr,abs(Avgimag8hr),Isd8hr,Isd8hr,'horizontal','Color',[0.5 0.5 0.5])
xlim([0 2500])
ylim([0 4000])
xlabel('Real Impedance (ohms)')
ylabel('-Imaginary Imepdance(ohms)')
hold on
plot(Avgreal8hr,abs(Avgimag8hr),'-','Color','#F4631E','LineWidth',2)
hold off

% Nyquist plot for average of all 16hr samples
figure(22)
errorbar(Avgreal16hr,abs(Avgimag16hr),Isd16hr,Isd16hr,'horizontal','Color',[0.5 0.5 0.5])
xlim([0 2000])
ylim([0 3000])
xlabel('Real Impedance (ohms)')
```

```
ylabel('-Imaginary Imepdance(ohms)')
hold on
plot(AvgReal16hr,abs(AvgImag16hr),'-','Color','#FF9F00','LineWidth',2)
hold off

% Nyquist plot for average of all 24hr samples
figure(23)
errorbar(AvgReal24hr,abs(AvgImag24hr),Isd24hr,Isd24hr,'horizontal','Color',[0.5 0.5 0.5])
xlim([0 1500])
ylim([0 2500])
xlabel('Real Impedance (ohms)')
ylabel('-Imaginary Imepdance(ohms)')
hold on
plot(AvgReal24hr,abs(AvgImag24hr),'-','Color','#007E7E','LineWidth',2)
hold off
```

Plot of steady state impedance

```
SS_Imp = [AvgModAgar(57),AvgMod0hr(57),AvgMod8hr(57),AvgMod16hr(57),AvgMod24hr(57)]
SS_StDev = [MsdAgar(57),Msd0hr(57),Msd8hr(57),Msd16hr(57),Msd24hr(57)]
xvals = [1 2 3 4 5]

errorbar(xvals,SS_Imp,SS_StDev,'.')
xlim([0 6])
ylim([0 35])

SS_Agar = MValsAgar(:,57);
SS_0hr = MVals0hr(:,57);
SS_8hr = MVals8hr(1:3,57);
SS_16hr = MVals16hr(:,57);
SS_24hr = MVals24hr(:,57);


%Agar vs 0hr
[h1,p1]=ttest(SS_Agar,SS_0hr)

%Agar vs 8hr
[h2,p2]=ttest(SS_Agar,SS_8hr)

%Agar vs 16hr
[h3,p3]=ttest(SS_Agar,SS_16hr)

%Agar vs 24hr
[h4,p4]=ttest(SS_Agar,SS_24hr)

%0hr vs 8hr
[h5,p5]=ttest(SS_0hr,SS_8hr)

%0hr vs 16hr
```

```
[h6,p6]=ttest(SS_0hr,SS_16hr)

%0hr vs 24hr
[h7,p7]=ttest(SS_0hr,SS_24hr)

%8hr vs 16hr
[h8,p8]=ttest(SS_8hr,SS_16hr)

%8hr vs 24hr
[h9,p9]=ttest(SS_8hr,SS_24hr)

%16hr vs 24hr
[h24,p24]=ttest(SS_16hr,SS_24hr)
```

B.3 Code used for Figures 15-18

```
Freq = table2array(ElectrodeAgarData(:,3));                % Frequency
range(Hz)

% Sample 1
S1R = table2array(ElectrodeAgarData(:,16));                % Real impedance
(ohm)
S1I = table2array(ElectrodeAgarData(:,17));                % Imaginary
impedance (ohm)
S1M = table2array(ElectrodeAgarData(:,18));                % Magnitude of
impedance (ohm)
S1P = table2array(ElectrodeAgarData(:,19));                % Phase (deg)

% Sample 3
S3R = table2array(ElectrodeAgarDataS2(:,16));
S3I = table2array(ElectrodeAgarDataS2(:,17));
S3M = table2array(ElectrodeAgarDataS2(:,18));
S3P = table2array(ElectrodeAgarDataS2(:,19));

% Sample 4
S4R = table2array(ElectrodeAgarDataS3(:,16));
S4I = table2array(ElectrodeAgarDataS3(:,17));
S4M = table2array(ElectrodeAgarDataS3(:,18));
S4P = table2array(ElectrodeAgarDataS3(:,19));
```

```
% Sample 5
S5R = table2array(ElectrodeAgarDataS4(:,16));
S5I = table2array(ElectrodeAgarDataS4(:,17));
S5M = table2array(ElectrodeAgarDataS4(:,18));
S5P = table2array(ElectrodeAgarDataS4(:,19));

AverageReal = (S1R+S3R+S4R+S5R)./4;                          % Averages of all
samples
AverageImag = (S1I+S3I+S4I+S5I)./4;
AverageMod = (S1M+S3M+S4M+S5M)./4;
AveragePhase = (S1P+S3P+S4P+S5P)./4;

% Find corner frequency
diff = Inf;
index = 0;
for i = 1:length(AverageReal)
    temp = abs(max(AverageReal) - abs(AverageImag(i)));

    if temp < diff
       index = i;
       diff = temp;
    end
end

firstcornerFreq = Freq(index);

diff = Inf;
index = 0;
for i = 1:length(AverageReal)
    temp = abs(min(AverageReal) - abs(AverageImag(i)));

    if temp < diff
       index = i;
       diff = temp;
    end
end

secondcornerFreq = Freq(index);

% Calculating error bar values
% Real Impedance
RVals = [S1R,S3R,S4R,S5R]';
Rsd = transpose(std(RVals));
% RPosError = max(RVals, [], 2) - AverageReal;
% RNegError = AverageReal - min(RVals, [], 2);

% Imaginary Impedance
IVals = [S1I,S3I,S4I,S5I]';
```

```
Isd = transpose(std(IVals));
% IPosError = max(IVals, [], 2) - AverageImag;
% INegError = AverageImag - min(IVals, [], 2);

% Magnitude
MVals = [S1M,S3M,S4M,S5M]';
Msd = transpose(std(MVals));
% MPosError = max(MVals, [], 2) - AverageMod;
% MNegError = AverageMod - min(MVals, [], 2);

% Phase
PVals = [S1P,S3P,S4P,S5P]';
Psd = transpose(std(PVals));
% PPosError = max(PVals, [], 2) - AveragePhase;
% PNegError = AveragePhase - min(PVals, [], 2);

% Bode plot for average of all samples
figure(1)
errorbar(Freq,AverageMod,Msd,'Color',[0.5 0.5 0.5])
xlim([1e-1 1e6])
ylim([1e0 1e4])
hold on
plot(Freq,AverageMod,'-','Color','black','LineWidth',2)
set(gca, 'XScale','log', 'YScale','log')
hold off

figure(2)
errorbar(Freq,AveragePhase,Psd,'Color',[0.5 0.5 0.5])
hold on
plot(Freq,AveragePhase,'-','Color','black','LineWidth',2)
xlim([1e-1 1e6])
ylim([-90 90])
yticks([-90 -45 0 45 90])
set(gca, 'XScale','log')
hold off

% Nyquist plot for average of all samples
figure(3)
errorbar(AverageReal,AverageImag,Rsd,Rsd,'Color',[0.5 0.5 0.5])
xlim([45 80])
ylim([-12 6])
hold on
plot(AverageReal, AverageImag,'-','Color','black','LineWidth',2)
hold off

figure(4)
errorbar(AverageReal,AverageImag,Isd,Isd,'horizontal','Color',[0.5 0.5 0.5])
xlim([45 80])
```

```
ylim([-12 6])
hold on
plot(AverageReal, AverageImag,'-','Color','black','LineWidth',2)
hold off
```

Published with MATLAB® R2019b

Appendix C. Supplementary Plots

C.1 Two-electrode measurements on tryptic soy agar

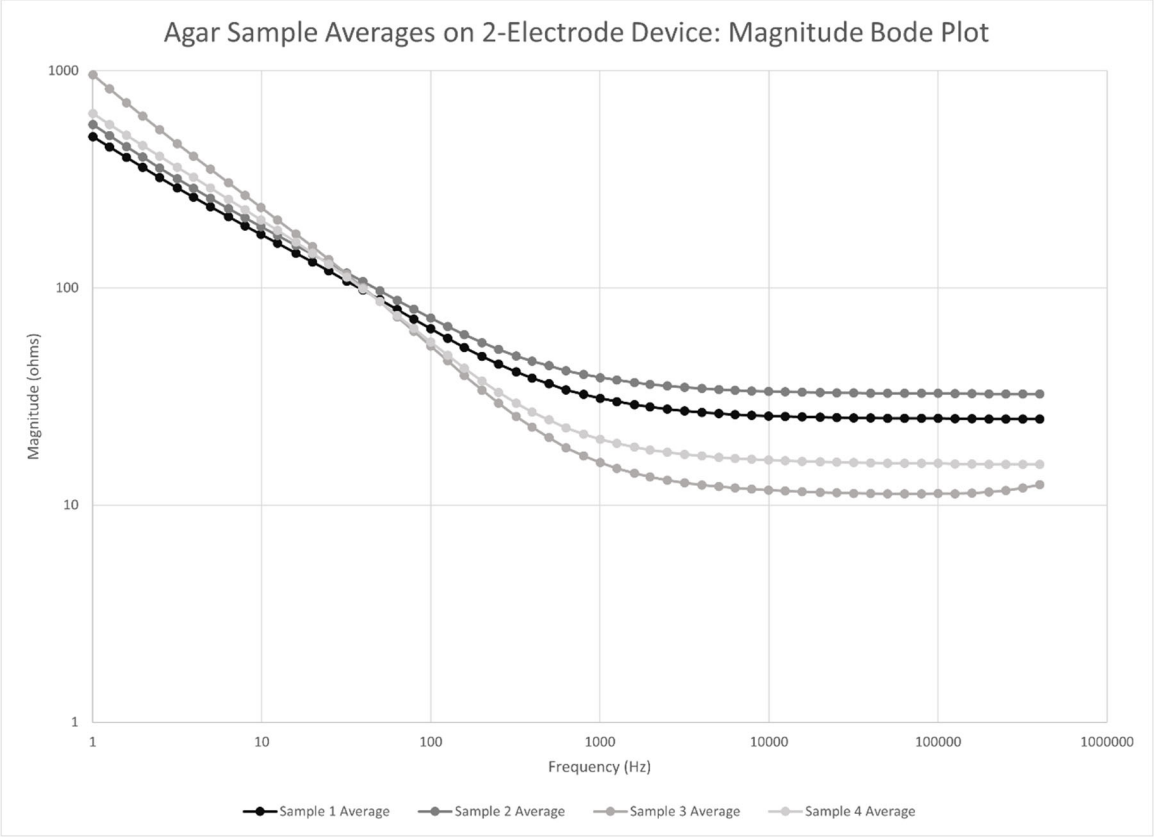

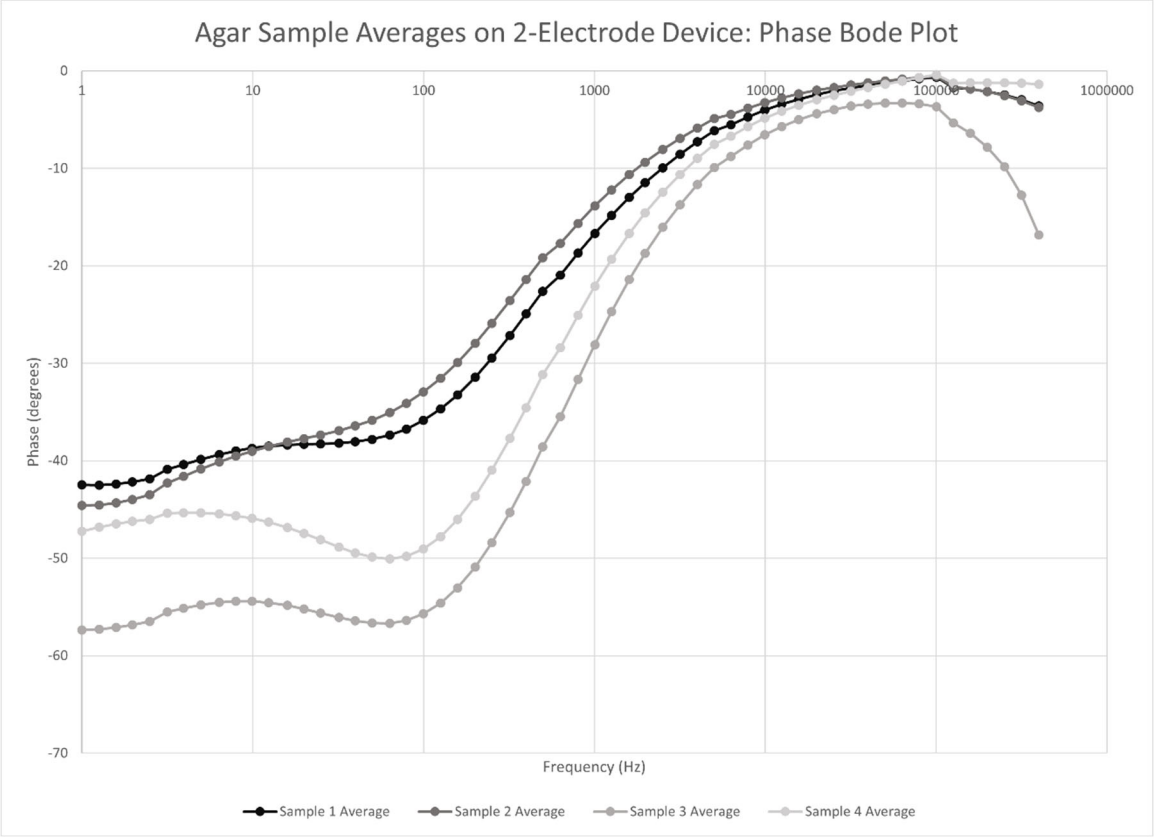
Agar Sample Averages on 2-Electrode Device: Phase Bode Plot
0
-10
-20
-30
-40
-50
-60
-70
Phase (degrees)
1
10
100
1000
10000
100000
1000000
Frequency (Hz)
Sample 1 Average
Sample 2 Average
Sample 3 Average
Sample 4 Average

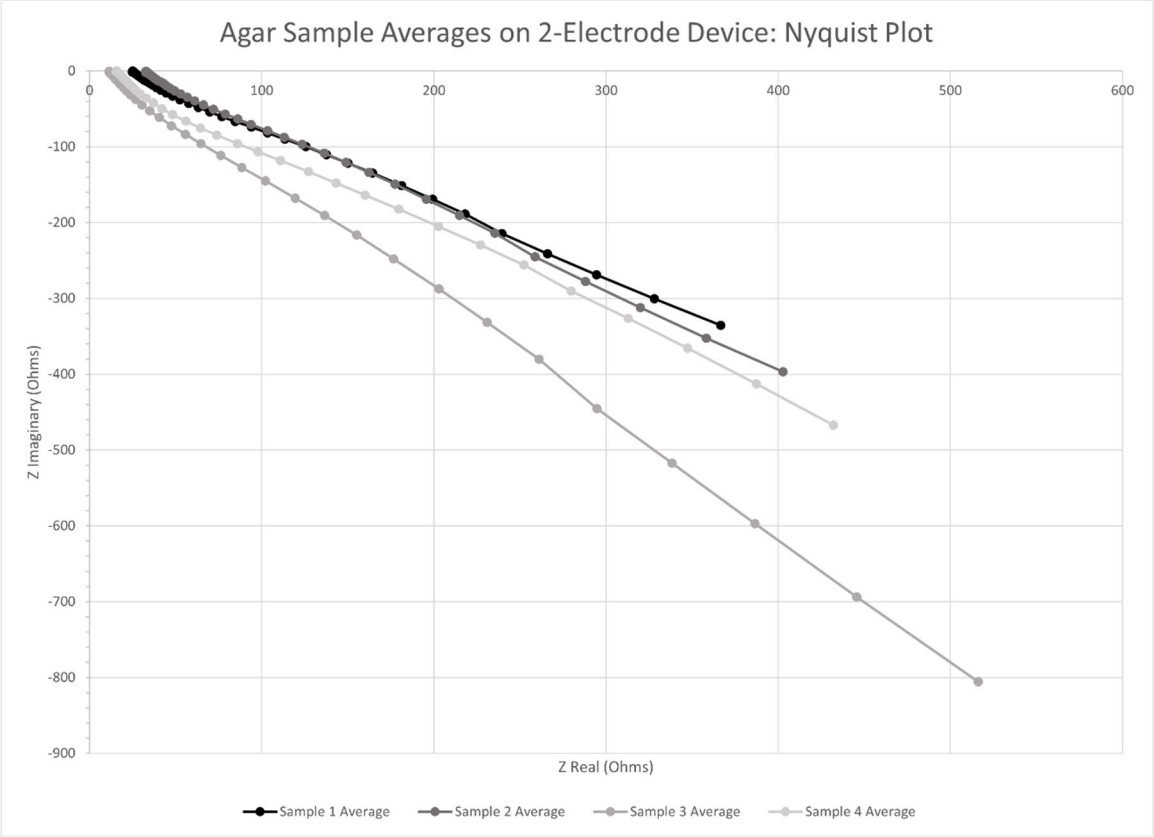
Agar Sample Averages on 2-Electrode Device: Nyquist Plot
0
-100
-200
-300
-400
-500
-600
-700
-800
-900
0
100
200
300
400
500
600
Z Imaginary (Ohms)
Z Real (Ohms)
Sample 1 Average
Sample 2 Average
Sample 3 Average
Sample 4 Average

C.2 Four-electrode measurements on tryptic soy agar

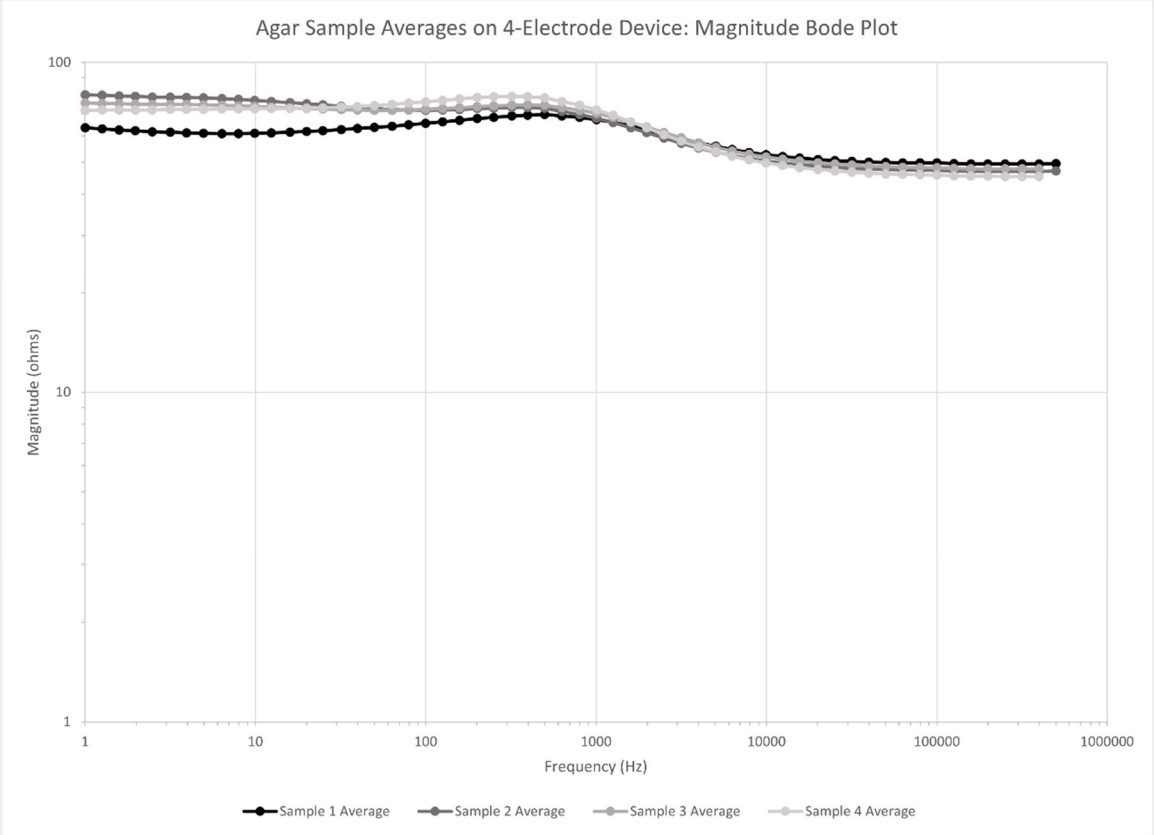

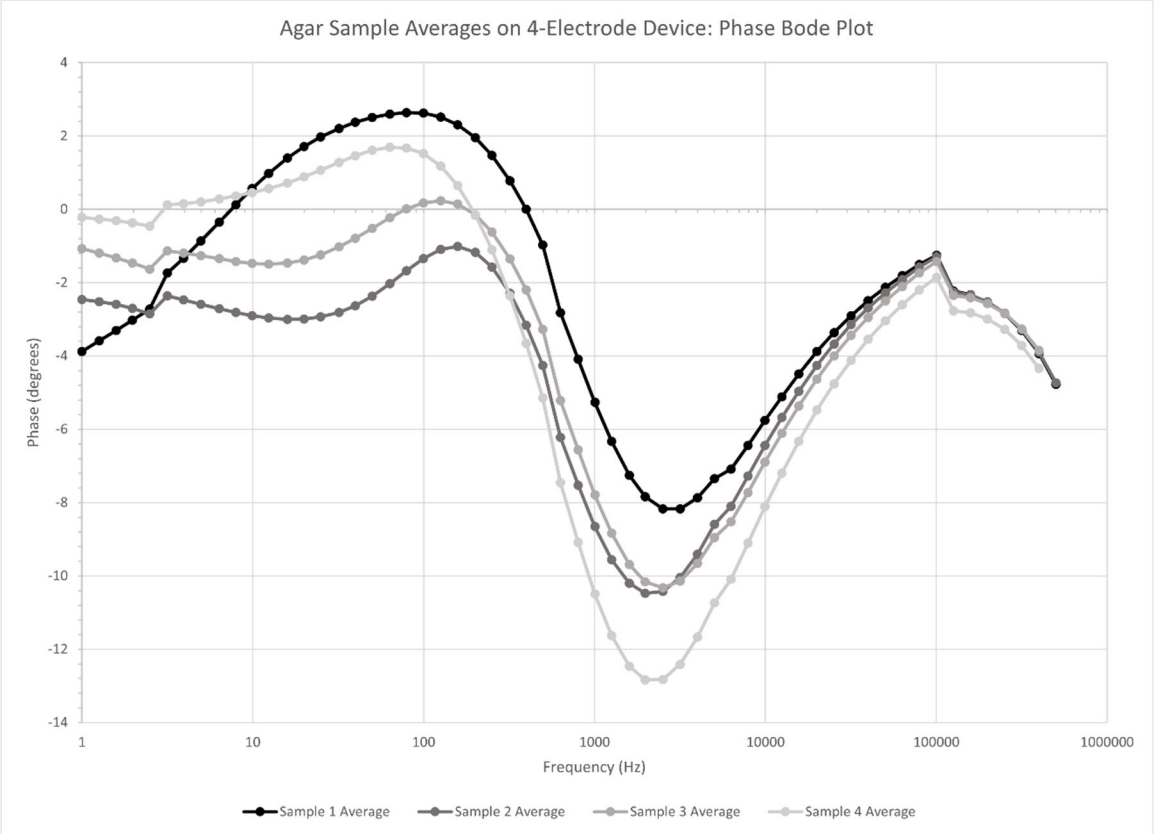
Agar Sample Averages on 4-Electrode Device: Phase Bode Plot
Phase (degrees)
4
2
0
-2
-4
-6
-8
-10
-12
-14
1
10
100
1000
10000
100000
1000000
Frequency (Hz)
Sample 1 Average
Sample 2 Average
Sample 3 Average
Sample 4 Average

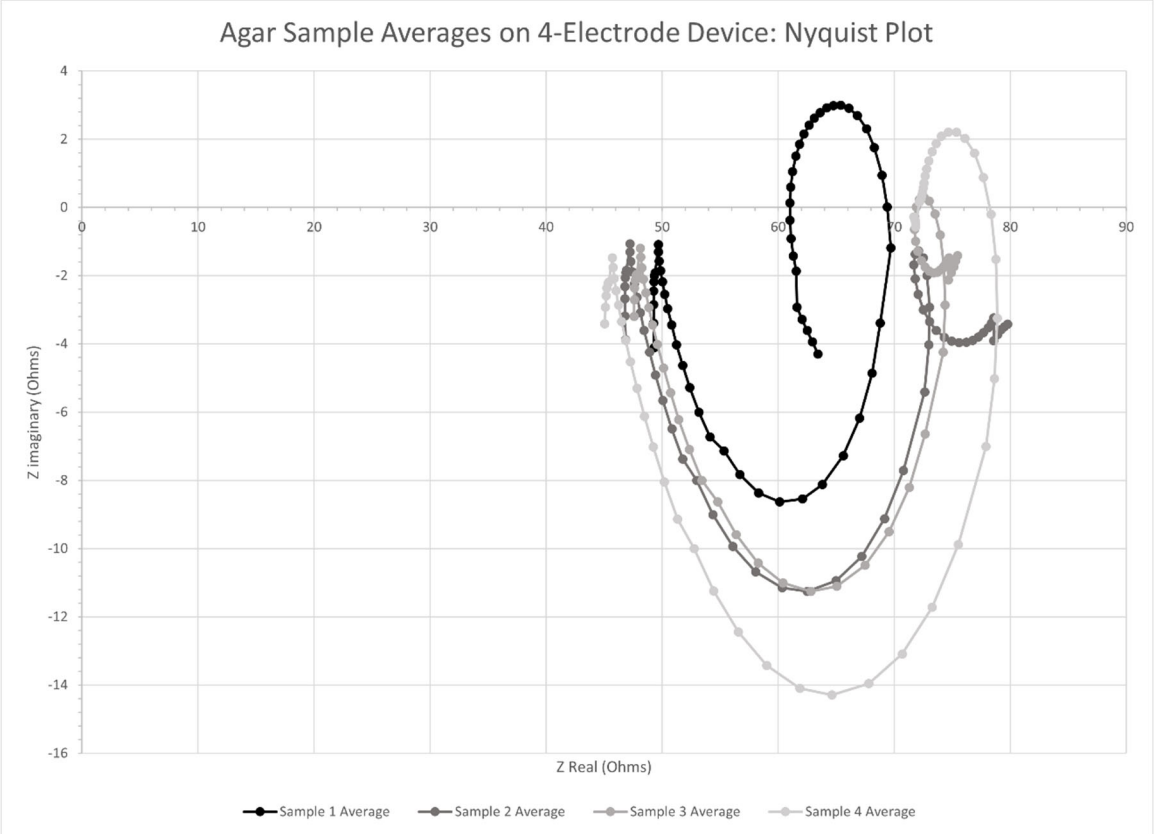
Agar Sample Averages on 4-Electrode Device: Nyquist Plot
Z imaginary (Ohms)
Z Real (Ohms)
4
2
0
-2
-4
-6
-8
-10
-12
-14
-16
0
10
20
30
40
50
60
70
80
90
Sample 1 Average
Sample 2 Average
Sample 3 Average
Sample 4 Average

C.3 Two-electrode measurements on 0-hour biofilm

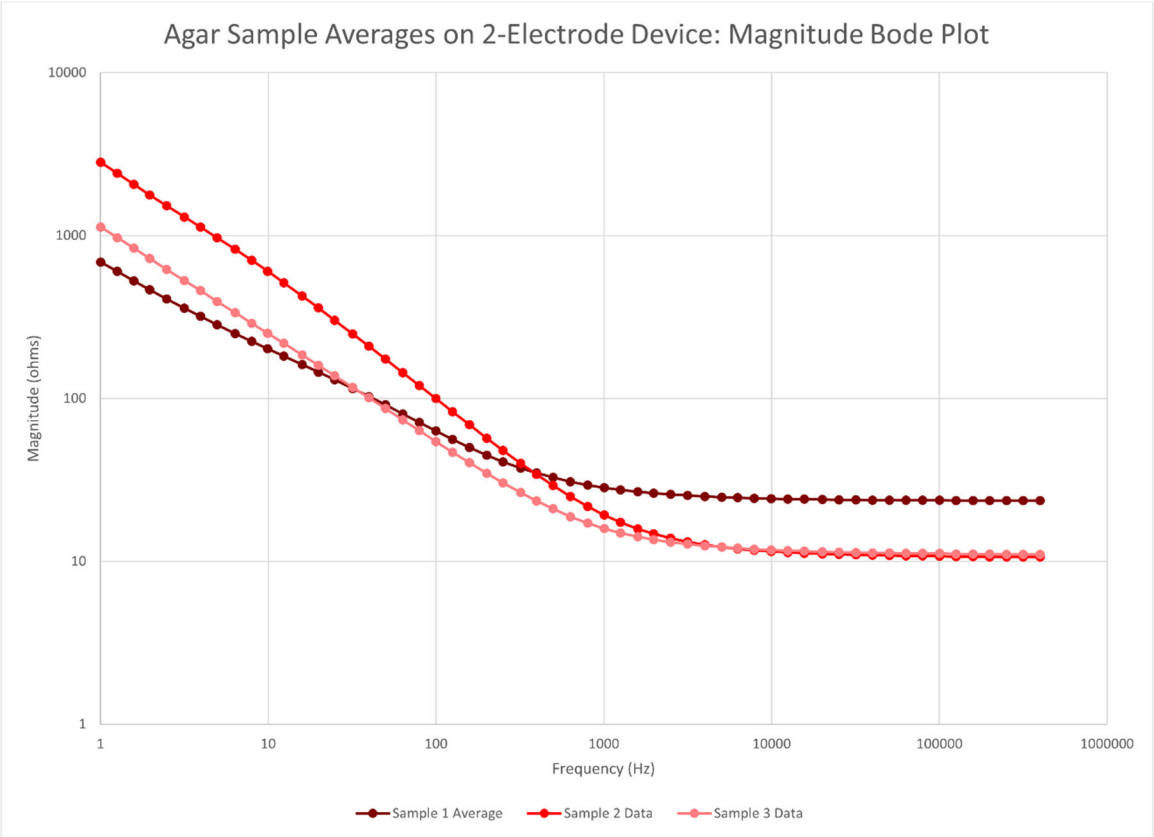

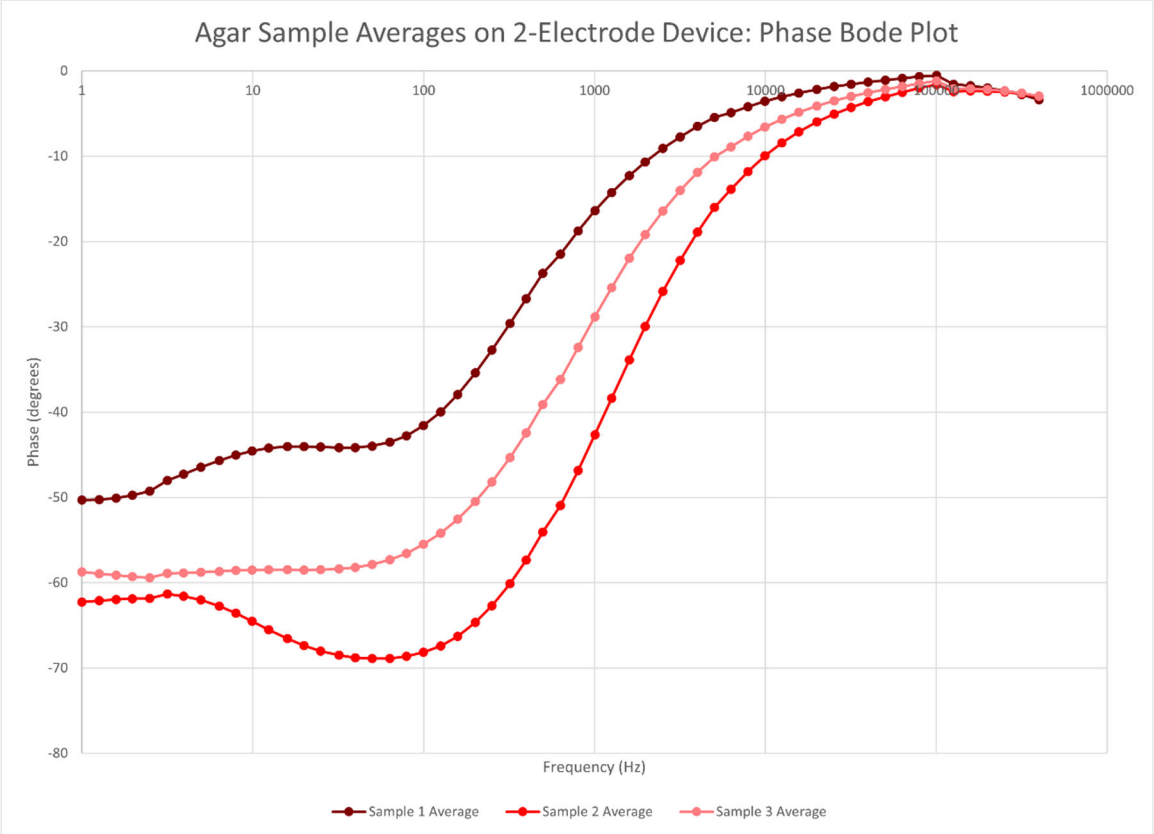
Agar Sample Averages on 2-Electrode Device: Phase Bode Plot
0
-10
-20
-30
-40
-50
-60
-70
-80
Phase (degrees)
1
10
100
1000
10000
100000
1000000
Frequency (Hz)
Sample 1 Average
Sample 2 Average
Sample 3 Average

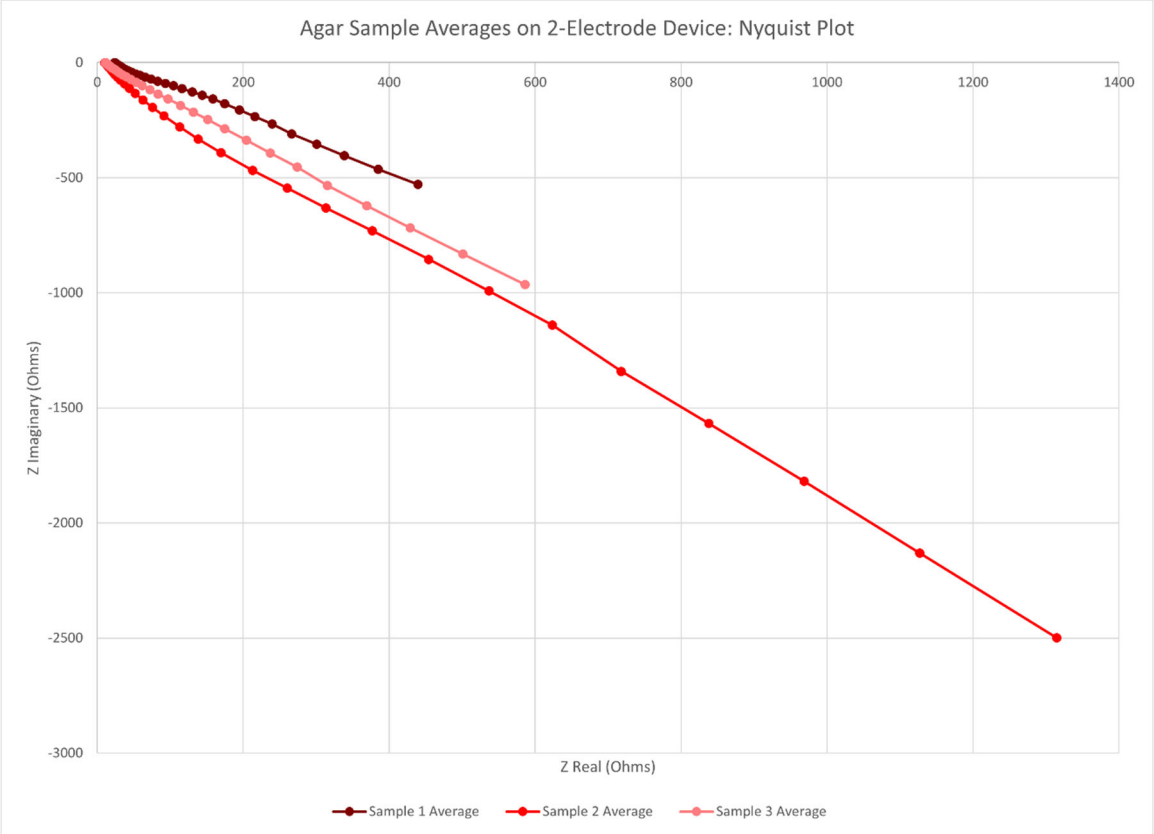
Agar Sample Averages on 2-Electrode Device: Nyquist Plot
0
-500
-1000
-1500
-2000
-2500
-3000
Z Imaginary (Ohms)
0
200
400
600
800
1000
1200
1400
Z Real (Ohms)
Sample 1 Average
Sample 2 Average
Sample 3 Average

C.4 Two-electrode measurements on 8-hour biofilm

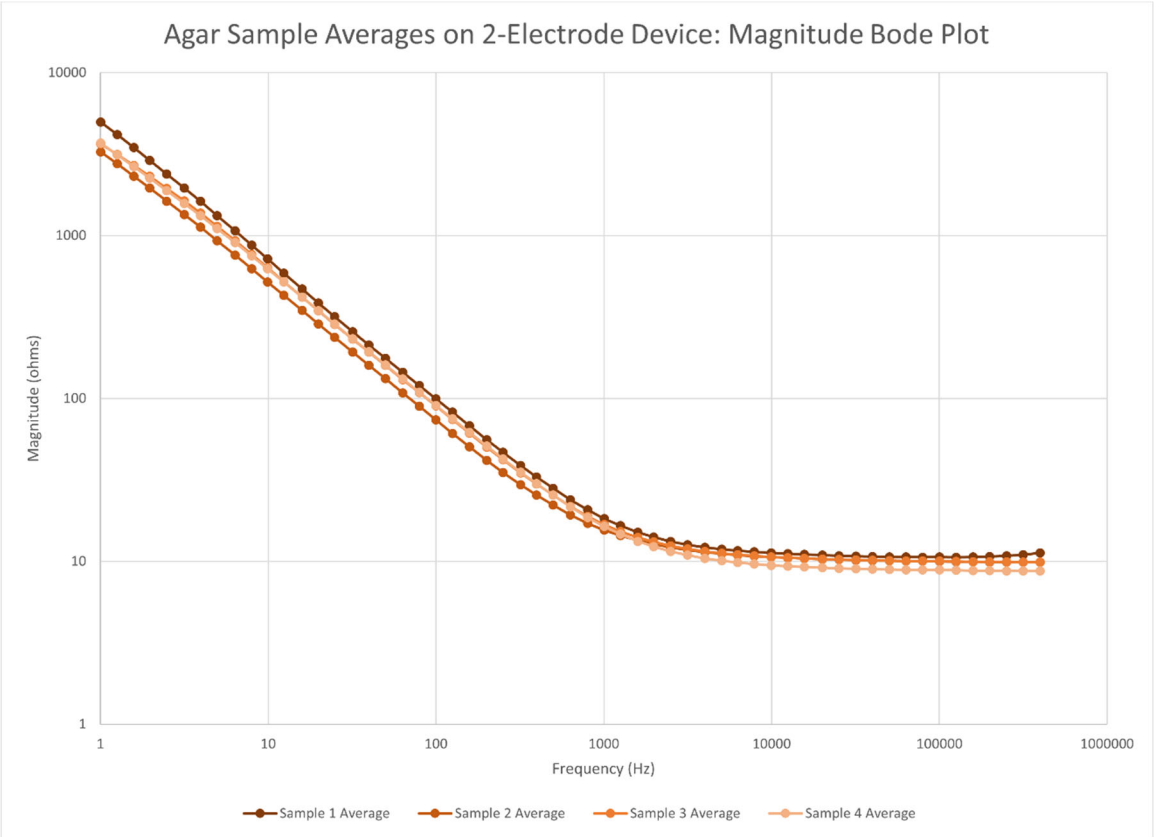

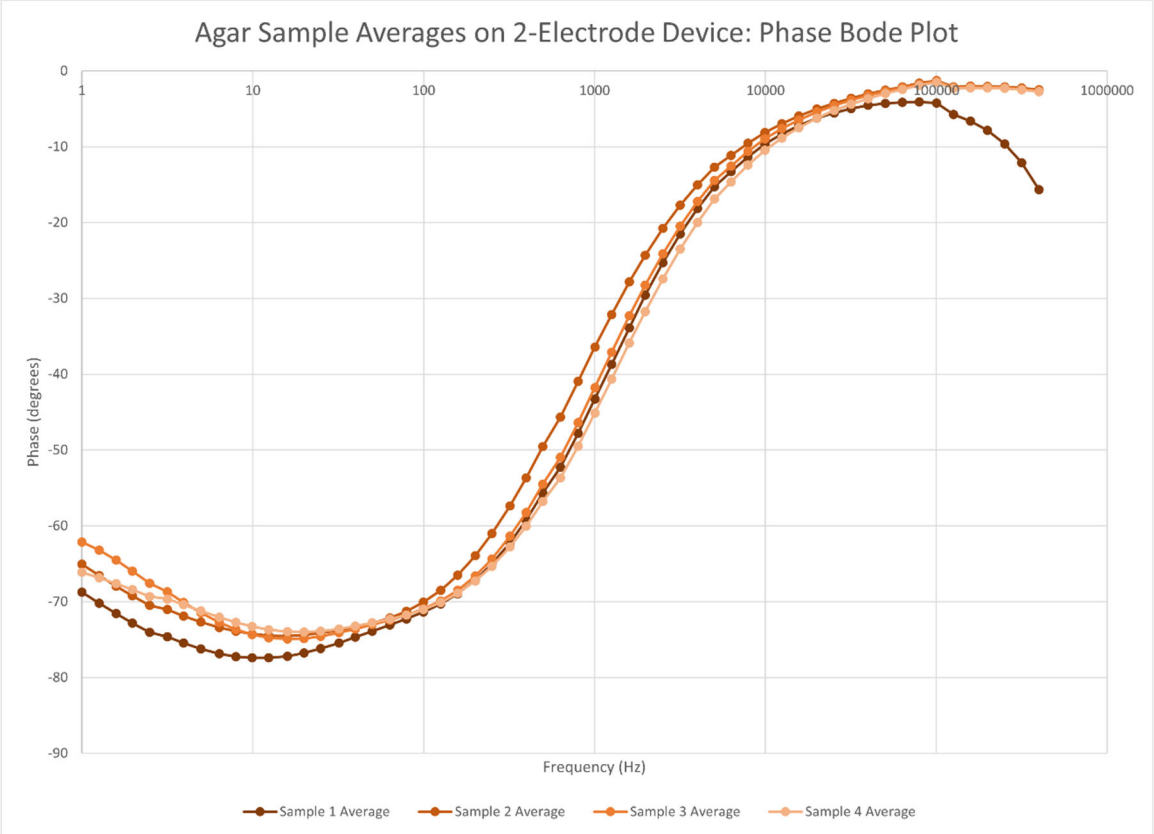
Agar Sample Averages on 2-Electrode Device: Phase Bode Plot
0
-10
-20
-30
-40
-50
-60
-70
-80
-90
Phase (degrees)
1
10
100
1000
10000
100000
1000000
Frequency (Hz)
Sample 1 Average
Sample 2 Average
Sample 3 Average
Sample 4 Average

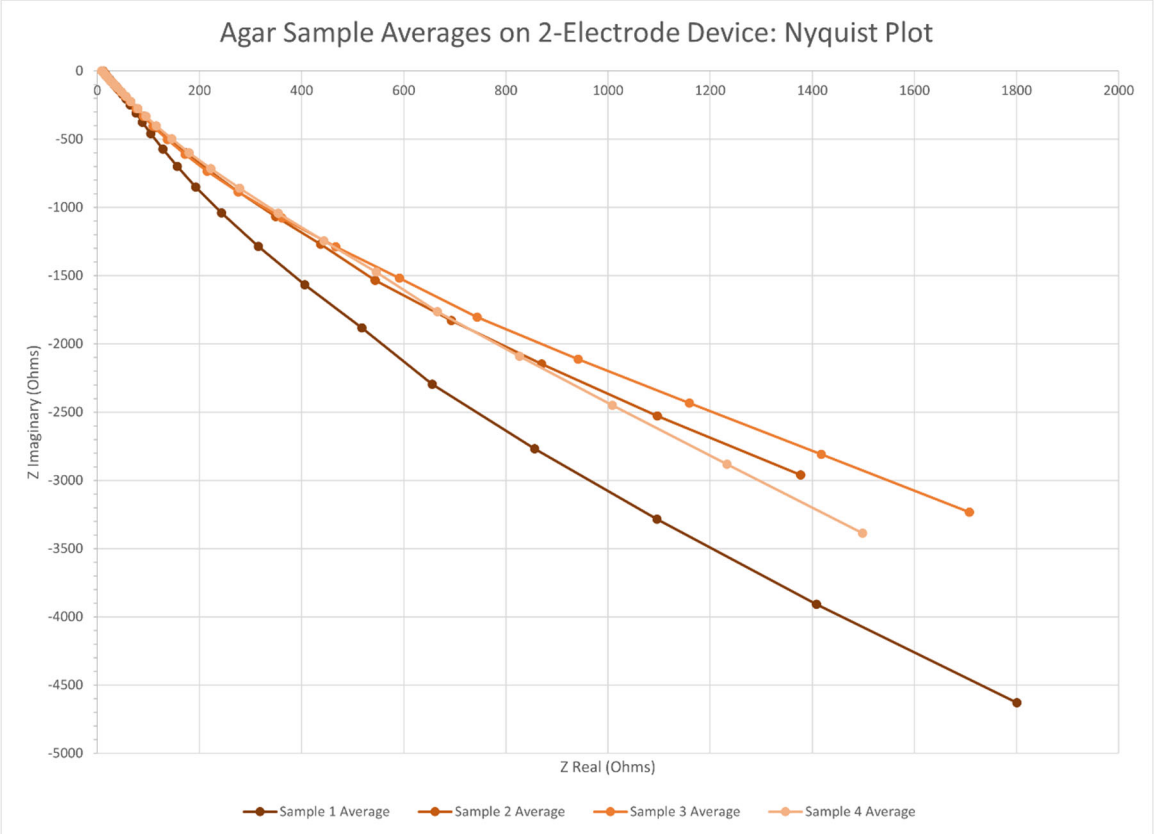
Agar Sample Averages on 2-Electrode Device: Nyquist Plot
0
-500
-1000
-1500
-2000
-2500
-3000
-3500
-4000
-4500
-5000
Z Imaginary (Ohms)
0
200
400
600
800
1000
1200
1400
1600
1800
2000
Z Real (Ohms)
Sample 1 Average
Sample 2 Average
Sample 3 Average
Sample 4 Average

C.5 Two-electrode measurements on 16-hour biofilm

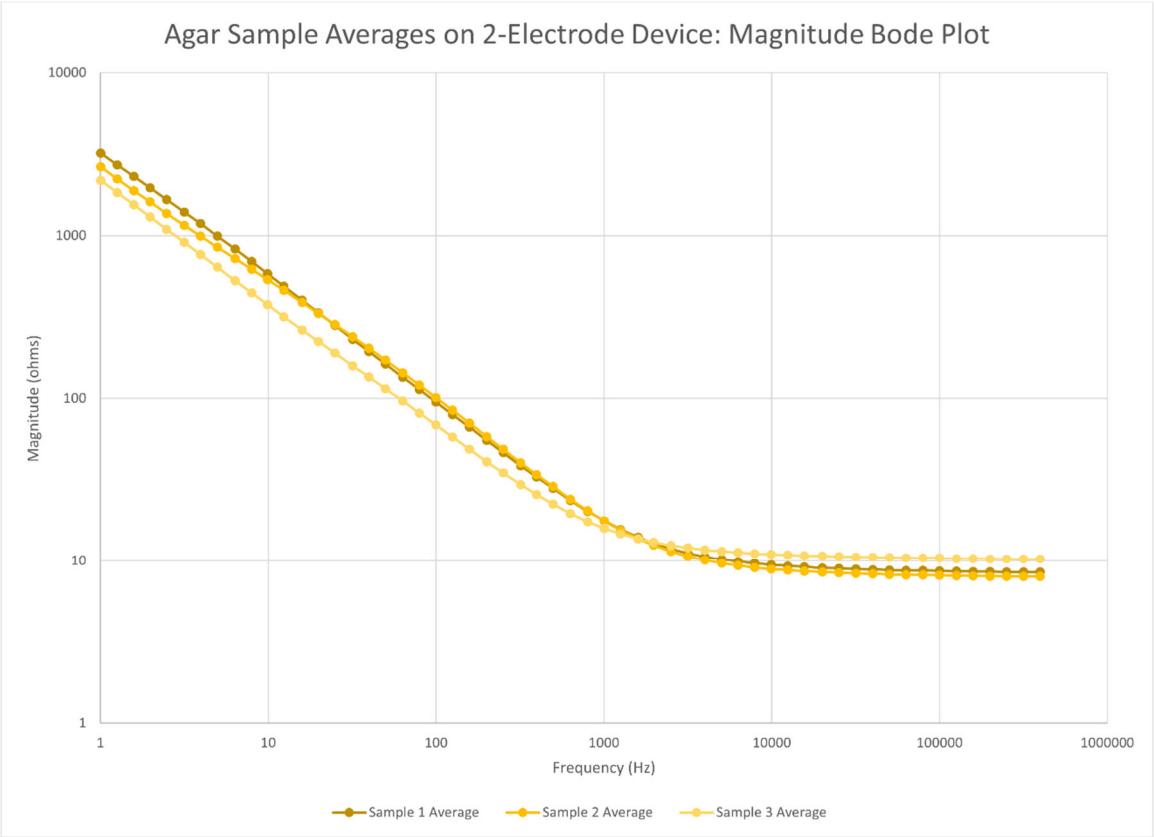

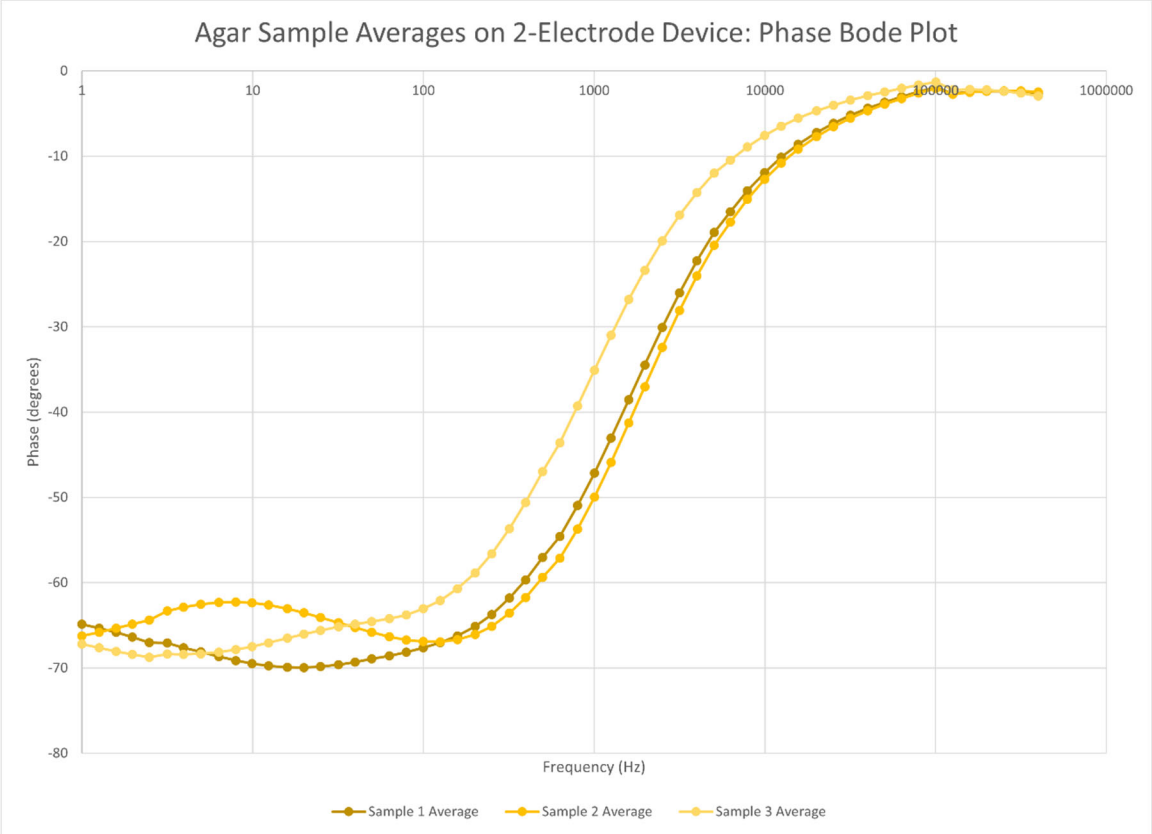
Agar Sample Averages on 2-Electrode Device: Phase Bode Plot
0
-10
-20
-30
-40
-50
-60
-70
-80
Phase (degrees)
1
10
100
1000
10000
100000
1000000
Frequency (Hz)
Sample 1 Average
Sample 2 Average
Sample 3 Average

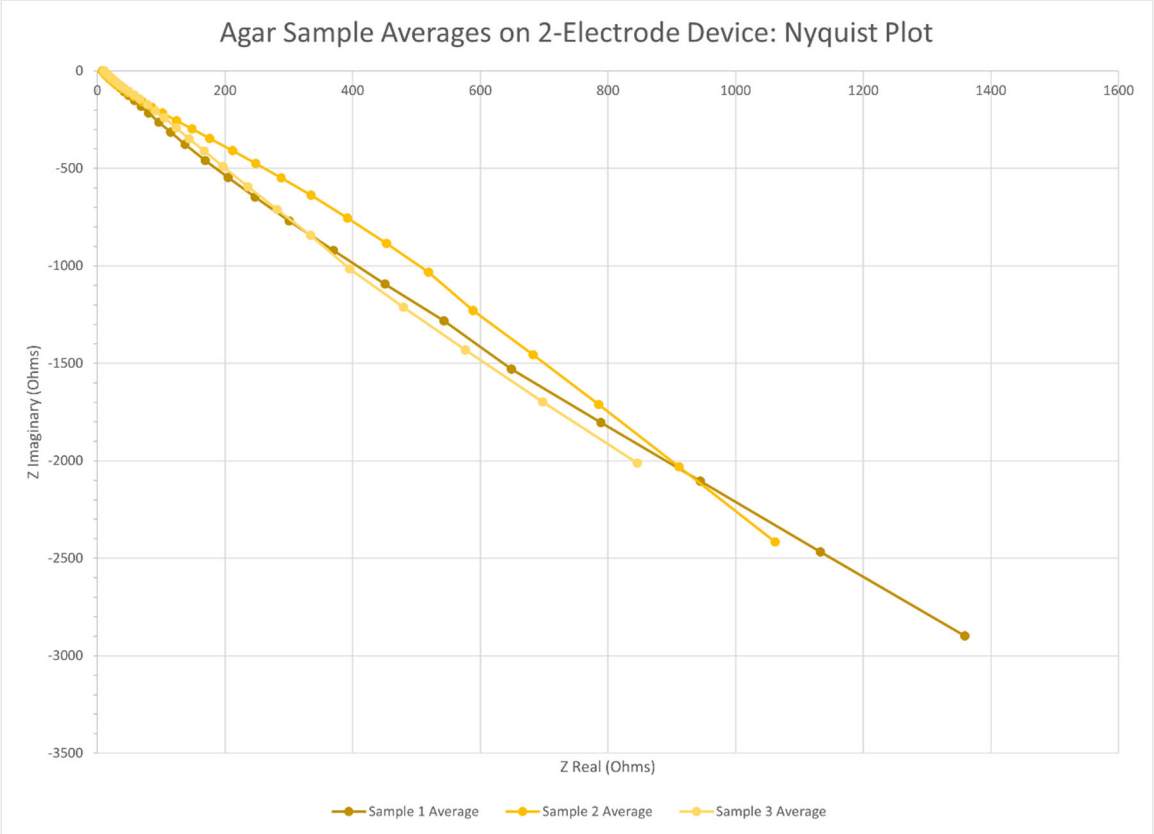
Agar Sample Averages on 2-Electrode Device: Nyquist Plot
0
-500
-1000
-1500
-2000
-2500
-3000
-3500
Z Imaginary (Ohms)
0
200
400
600
800
1000
1200
1400
1600
Z Real (Ohms)
Sample 1 Average
Sample 2 Average
Sample 3 Average

C.6 Two-electrode measurements on 24-hour biofilm

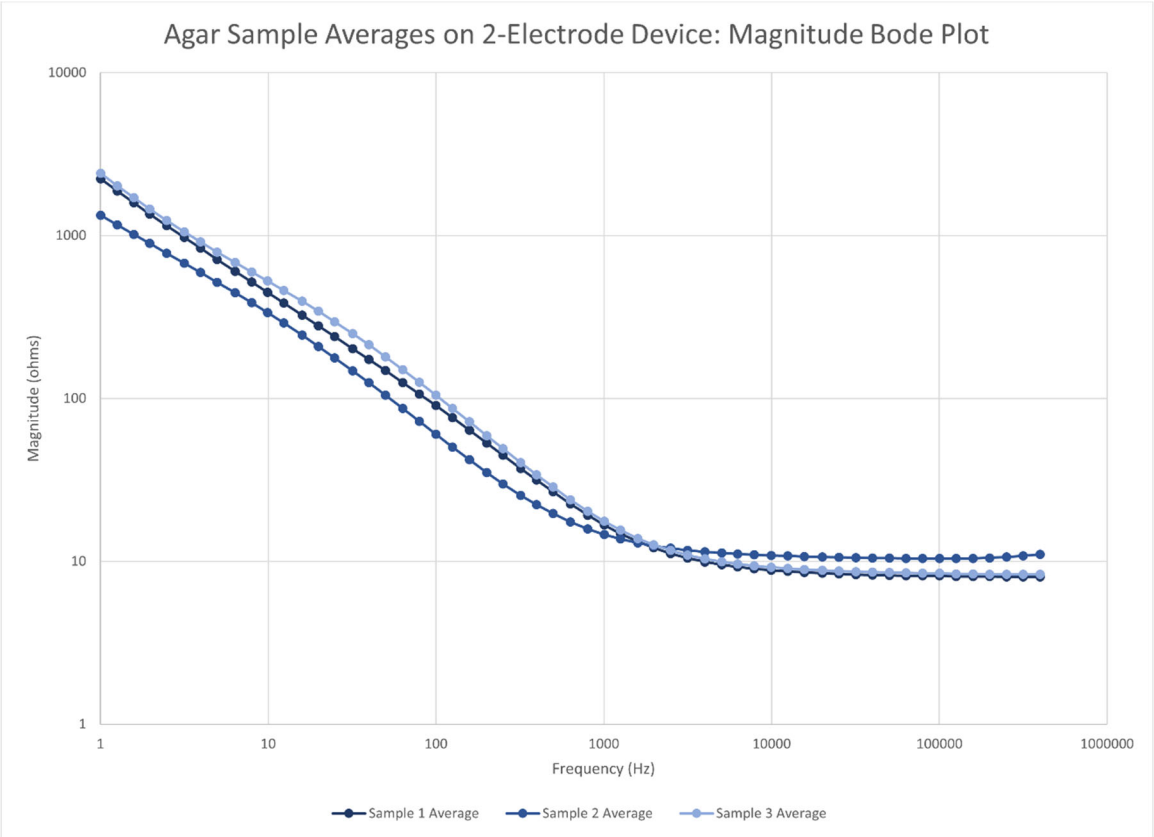

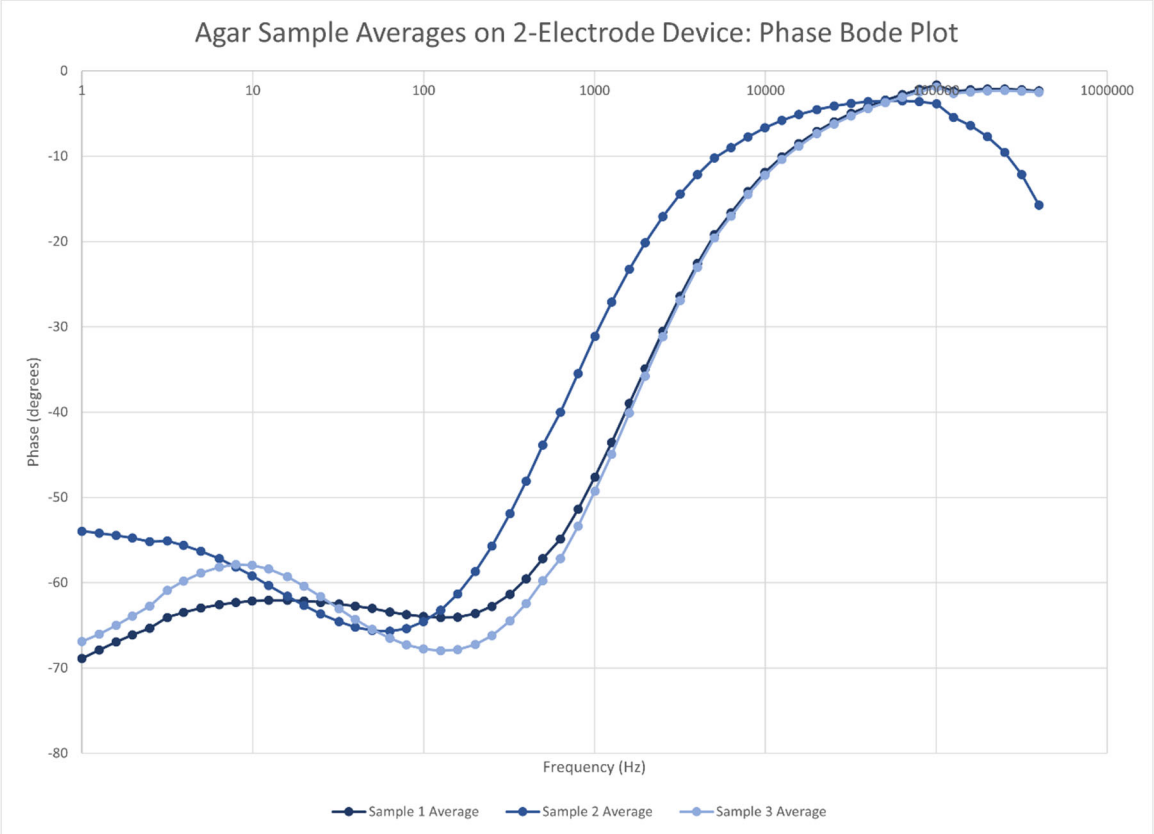
Agar Sample Averages on 2-Electrode Device: Phase Bode Plot
0
-10
-20
-30
-40
-50
-60
-70
-80
Phase (degrees)
1
10
100
1000
10000
100000
1000000
Frequency (Hz)
Sample 1 Average
Sample 2 Average
Sample 3 Average

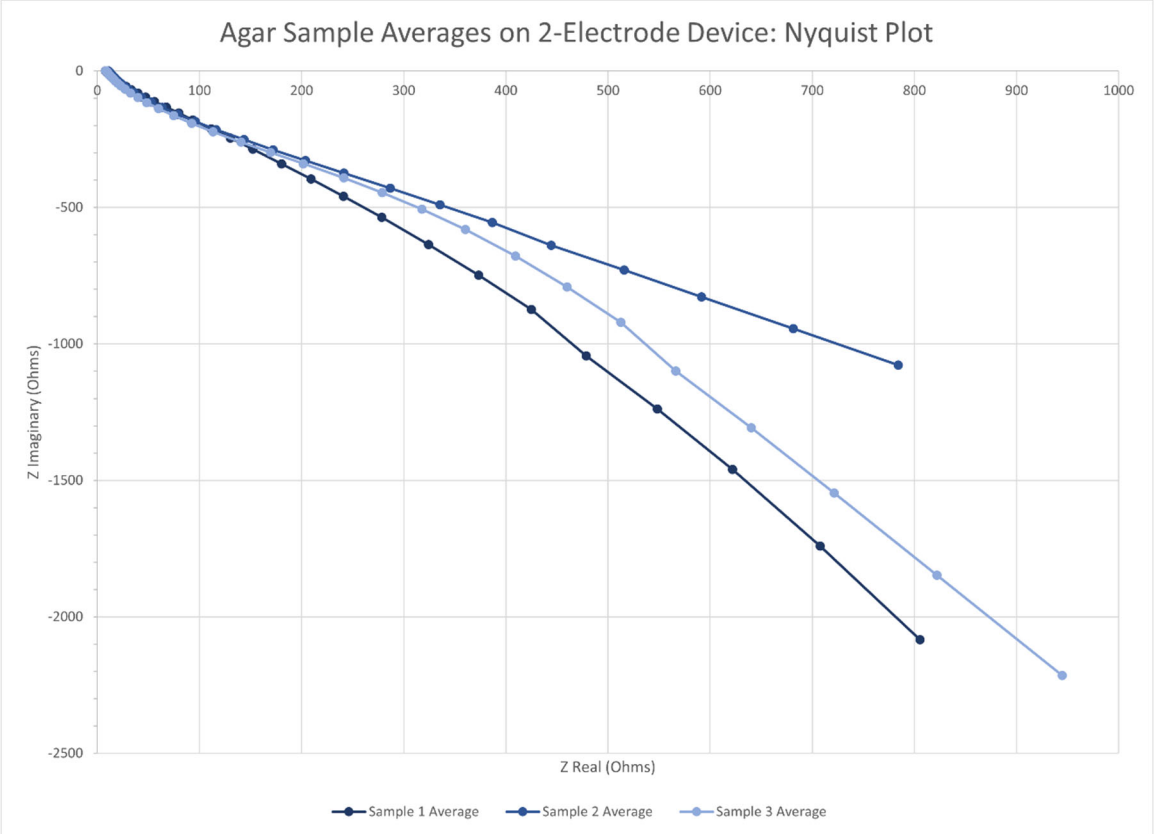
Agar Sample Averages on 2-Electrode Device: Nyquist Plot
0
-500
-1000
-1500
-2000
-2500
Z Imaginary (Ohms)
0
100
200
300
400
500
600
700
800
900
1000
Z Real (Ohms)
Sample 1 Average
Sample 2 Average
Sample 3 Average